

A New Methodology for Frequency Domain Analysis of Wave Energy Converters
with Periodically Varying Physical Parameters

by

Mark Mosher

B.ScE, University of New Brunswick, 2009

A Thesis Submitted in Partial Fulfillment of the
Requirements for the Degree of

MASTER OF APPLIED SCIENCE

in the Department of Mechanical Engineering

© Mark Mosher, 2012
University of Victoria

All rights reserved. This thesis may not be reproduced in whole or in part, by
photocopying or other means, without the permission of the author.

A New Methodology for Frequency Domain Analysis of Wave Energy Converters
with Periodically Varying Physical Parameters

by

Mark Mosher

B.ScE, University of New Brunswick, 2009

Supervisory Committee

Dr. Bradley Buckham, Supervisor
(Department of Mechanical Engineering)

Dr. Peter Wild, Departmental Member
(Department of Mechanical Engineering)

Dr. Ben Nadler, Departmental Member
(Department of Mechanical Engineering)

Supervisory Committee

Dr. Bradley Buckham, Supervisor
(Department of Mechanical Engineering)

Dr. Peter Wild, Departmental Member
(Department of Mechanical Engineering)

Dr. Ben Nadler, Departmental Member
(Department of Mechanical Engineering)

ABSTRACT

Within a wave energy converter's operational bandwidth, device operation tends to be optimal in converting mechanical energy into a more useful form at an incident wave period that is proximal to that of a power-producing mode of motion. Point absorbers, a particular classification of wave energy converters, tend to have a relative narrow optimal bandwidth. When not operating within the narrow optimal bandwidth, a point absorber's response and efficiency is attenuated. Given the wide range of sea-states that can be expected during a point absorber's operational life, these devices require a means to adjust, or control, their natural response to maximize the amount of energy absorbed in the large population of non-optimal conditions. In the field of wave energy research, there is considerable interest in the use of non-linear control techniques to this end.

Non-linear control techniques introduce time-varying and state dependent control parameters into the point absorber motion equations, which usually motivates a computationally expensive numerical integration to determine the response of the device - important metrics such as gross converted power and relative travels of the device's pieces are extracted through post processing of the time series data. As an alternative, the work presented in this thesis was based on a closed form perturbation based

approach for analysis of the response of a device with periodically-varying control parameters, subject to regular wave forcing, in the frequency domain.

The proposed perturbation based method provides significant savings in computational time and enables the device's response to be represented in a closed form manner with a relatively small number of solution components - each component is comprised of a complex amplitude and oscillation frequency. This representation of the solution was found to be very concise and descriptive, and to lend itself to the calculation of gross absorbed power and travel constraint violations, making it extremely useful in the automated design optimization process; the methodology allows large number of design iterations, including both physical design and control variables, to be evaluated and conclusively compared.

In the development of the perturbation method, it was discovered that the device's motion response can be calculated from an infinite series of second order ordinary differential equations that can be truncated without destroying the solution accuracy. It was found that the response amplitude operator for the generic form of a solution component provides a means to gauge the device's response to a given wave input and control parameter variation, including a gauge of the solution process stability. It is unclear as of yet if this is physical, a result of the solution process, or both. However, for a given control parameter set resulting in an unstable solution, the instability was shown to be, at least in part, a result of the device's dynamics.

If the stability concerns can be addressed through additional constraints and updates to the wave energy converter hydrodynamic parameters, the methodology will expand on the commonly accepted boundaries for wave energy converter frequency-domain analysis methods and be of much practical importance in the evaluation of control techniques in the field of wave energy converter technology.

Contents

Supervisory Committee	ii
Abstract	iii
Table of Contents	v
List of Tables	vii
List of Figures	viii
Nomenclature	xiii
Acknowledgements	xvi
1 Introduction	1
1.1 Motivation	4
1.2 Thesis Objectives	5
1.3 Literature Review	6
1.3.1 Wave Energy Converter (WEC) Technology	6
1.3.2 Mathematical Modeling of Immersed Body Oscillation	11
1.3.3 WEC Control	15
1.3.4 SyncWave Case Study	20
1.4 Thesis Overview	27
2 Mathematical Modelling of WECs	28
2.1 Governing Dynamic Equations	28
2.2 Added Mass, Hydrodynamics and Radiation	33
2.3 Intrinsic Periodically Varying Control Actions	34
2.4 Steady State Solution	36
2.4.1 Governing Equations	36

2.4.2	Recursive Procedure	38
2.5	Convergence Analysis	51
3	Computational Efficiency	57
3.1	WEC Motion Response Calculation	58
3.1.1	Perturbation Method with Shared Frequency Improvements	60
3.1.2	Solution Representation Simplification	62
3.2	WEC Response Bandwidth Limitation	65
3.3	Significant Relative Travel	72
4	Net Power Absorption	79
4.1	Gross Power Absorption Expression	80
4.2	Gross Power Absorption Convergence Analysis	82
4.3	Variable Effective-Mass Unit Kinematics & Energy Consumption	86
4.3.1	Control System Design Concept	86
4.3.2	Variable Effective-Mass Unit Kinematics	91
4.3.3	Variable Effective-Mass Unit Kinetics	92
4.3.4	Variable Effective-Mass Unit Average Power Consumption	94
5	Conclusions & Future Work	98
5.1	Main Findings	98
5.2	Future Work	102
5.2.1	Stability Analysis	102
5.2.2	Perturbation Methodology Extension	108
A	Methodology Extension to a Three Term Control Input	109
	Bibliography	113

List of Tables

Table 1.1	Scaled SyncWave WEC Demonstration Device Parameters . . .	22
Table 2.1	Wave and physical control parameters used in demonstration case.	52
Table 3.1	Computational time and memory storage requirements of WEC device response evaluation for both a Runge-Kutta-Fehlberg numerical integration time-domain method and perturbation method with shared frequency improvements.	62
Table 3.2	Computational time and memory storage requirements of WEC device response evaluation for the improved perturbation method and the improved perturbation method with limited bandwidth, $0\frac{\text{rad}}{\text{s}} \leq \omega \leq 5\frac{\text{rad}}{\text{s}}$	70
Table 4.1	Froude scaled variable effective-mass unit physical parameters. .	89
Table 5.1	Wave and physical control parameters used to demonstrate an unstable response evaluation case.	103

List of Figures

Figure 1.1 A select few of the differing wave energy converter devices currently undergoing research internationally. The power take-off for these devices is represented as a viscous dashpot or spinning turbine.	2
Figure 1.2 Classification of Floating Wave Energy Converters[6]	7
Figure 1.3 The P2 Pelamis is an attenuator made up of five connected bodies totaling 180m in length and 4m in diameter. Each of the WEC's joints contain a power take-off to convert the bodies relative motion into electricity(www.pelamiswave.com).	7
Figure 1.4 The OceanLinx MK1 was a 500 tonne oscillating water column WEC installed in Port Kembla, Australia, in 2005(www.oceanlinx.com).	8
Figure 1.5 Carnegie's CETO III is a one-bodied point absorber located off the shores of Garden Island in Western Australia (www.carnegiewave.com).	9
Figure 1.6 Ocean Power Technologies' P150 PowerBuoy is self-reacting point-absorber rated at a capacity of 150kW. The device is shown horizontally prior to installation off Scotland's northeast coast in 2011 (www.oceanpowertechnologies.com).	10
Figure 1.7 Orbital fluid particle motion of Airy waves. The expressions for vertical particle velocities and accelerations are both time and depth dependent, given by $v(z, t) = \vec{v}(z) \cos \omega t$ and $a(z, t) = \vec{a}(z) \cos \omega t$ respectively.[16]	12
Figure 1.8 Latching control matches the phase of the forcing wave by holding the device fixed at the end of an oscillation for a latching period, T_L .[25]	18
Figure 1.9 Schematic of the SyncWave WEC device.	21
Figure 1.10 Bathymetric data for Hesquiaht Sound, British Columbia. Labeled are five potential test sites A-E.[29]	23

Figure 1.11 Variance density spectrum and resulting monthly significant wave height and energy periods of a characteristic year for five potential test sites, ‘A’ through ‘E’, in Hesquiaht Sound, British Columbia [29].	26
Figure 2.1 Diagram showing the three-degree of freedom SyncWave device. For the Lagrangian analysis, a control volume is taken surrounding the spar body and the enclosed variable effective mass system [10].	29
Figure 2.2 Clarification of the terminology used throughout this work. . .	39
Figure 2.3 The frequency and phase coefficients for an arbitrary level, n , are mapped from a component in the previous level’s solution, $\underline{z}_{n-1}^{(j)}(t)$. The preceding level’s component is responsible for generating two components on the n^{th} level. Note: the generated components share similar coefficient mapping, but differ by a sign.	46
Figure 2.4 The construction of the solution for an example case. The magnitude of each level’s components are shown in relation to their position in the solution array. Physical parameters for this simulation are given in Table 2.1	49
Figure 2.5 Construction of the spar response using the perturbation method.	50
Figure 2.6 The convergence of perturbation method motion response to the time-domain simulation is measured using the norm of the difference between the two responses. $\underline{z}(t), 500s \leq t \leq 1000s$, was calculated using the time-domain integration approach and the perturbation approach outlined in this chapter.	53
Figure 2.7 Time-series motion for each of the device’s bodies are shown at different perturbation method solution levels in grey, and compared to the motion of the time-domain simulation shown in black. Physical parameters for this simulation are given in Table 2.1	54
Figure 2.8 Computational efficiency comparison between the perturbation method and tradition time-domain numerical integration. The evaluation speed and memory required for the proposed methodology, in its current state, is much too demanding past the level of $N=13$	56

Figure 3.1 Absolute motion components for each body – the phase information for each component has been removed. All solution components with equivalent frequencies are summed in complex form. Physical parameters for this simulation are given in Table 2.1 59

Figure 3.2 The formulation of each subsequent level’s oscillation frequencies without the summation of amplitudes of components with equivalent oscillation frequencies 60

Figure 3.3 The formulation of each subsequent level’s oscillation frequencies with the summation of amplitudes of components with shared oscillation frequencies 60

Figure 3.4 Absolute motion components for each body. All solution components with equivalent frequencies, both within and across levels of the solution, are summed in complex form and then reported as amplitudes. Physical parameters for this example problem that generated the solution are given in Table 2.1 63

Figure 3.5 The solution components that are most important in creating an accurate time-motion response are visually evaluated by comparing the solution component magnitudes to their RAO (a),(c) and (e). The 2-norm errors associated with bandwidth limitation are shown in (b),(d) and (f). 68

Figure 3.6 Absolute motion components for each body for the bandwidth limited improved perturbation method. Solution components have been limited to oscillation frequencies within $0 \frac{rad}{s} \leq \omega \leq 5 \frac{rad}{s}$. Physical parameters for this simulation are given in Table 2.1 71

Figure 3.7 Relative motion response. Physical parameters for this simulation are given in Table 2.1. 74

Figure 3.8 Relative motion component magnitudes and phases. Physical parameters for this simulation are given in Table 2.1. Note: the component magnitudes have been multiplied by two to adhere with the complex conjugate simplification introduced in Section 2.4. 75

Figure 3.9	The Rayleigh probability density function for relative motion between a WEC's bodies. An area calculated under this function can be used to find the probability that the relative motion, H_r , exceeds a certain height, H_{lim} , shown here in grey.	76
Figure 3.10	Physical relative travel constraints are shown over the probability density function. The relative height travel constraints, H_{lim} , were taken as twice the amplitude constraints given in Table 1.1. Physical parameters for this simulation are given in Table 2.1	78
Figure 4.1	Convergence on a true average power. A numerically integrated average power for the time-domain's motion response is shown in black, where the lower limit of the integration interval was extended from the end of the simulation to time zero. A series of definite integrals were carried out for the perturbation method simulation, where the upper-limit of integration was varied from time zero to the end of the time-motion response.	83
Figure 4.2	The number of levels required in the motion response to convergence on a true average power for the perturbation analysis. A series of definite integrals were carried out upon each level, where the upper-limit was set to a value of 1000 seconds.	85
Figure 4.3	Variable effective-mass unit parameter design	87
Figure 4.4	Top view of variable effective-mass unit with contracted inertial arms	88
Figure 4.5	Inertial arm rotation angle as a function of the prescribed variation of the effective mass.	90
Figure 4.6	Coordinate systems for derivation of energy required to actuate the rotational position of the inertial arms. Note: in the orientation shown, both the \mathbf{x} and \mathbf{X} coordinates are pointing out of the page.	91
Figure 4.7	Instantaneous torque and power requirements of the variable effective-mass unit for the case study parameters given in Table 2.1. Three different power requirement scenarios are given according to possible physical designs.	96
Figure 4.8	Convergence on average power required to accurate inertial arms for three different implementation cases.	97

Figure 5.1 A flowchart depicting a potential automated optimization routine using the functions provided in this thesis.	99
Figure 5.2 A stable perturbation approach solution evaluation. Physical parameters for this simulation are given in Table 2.1	104
Figure 5.3 An unstable perturbation approach solution evaluation. Physical parameters for this simulation are given in Table 5.1. Note that the vertical axis' scale for both plots is quite different from the corresponding plots in Figure 5.2.	105
Figure 5.4 RAO shape changes with varied generator damping. Other physical parameters can be found in Table 5.1.	106
Figure 5.5 RAO shape changes with varied reaction mass damping. Other physical parameters can be found in Table 5.1.	107
Figure A.1 Pascal's pyramid for complete polynomials. The solution components have been ordered in such a way that they can be solved sequentially.	112

Nomenclature

A	Wave amplitude
\mathbf{C}	Device damping matrix
\mathbf{C}_L	Device damping matrix found in the linear mathematical model
E	Energy absorbed by the device
$E(f)$	Variance density spectrum
H	Regular wave height
H_{lim}	A relative travel limit constraint
H_r	Relative travel height
H_s	Significant wave height
I_{xx}, I_{yy}, I_{zz}	Moments of inertia
$\underline{\mathbf{I}}, \underline{\mathbf{J}}, \underline{\mathbf{K}}$	Unit vectors in the direction of X, Y, and Z, respectively
J	Rotational inertia of the variable effective mass unit
J_{max}	Maximum rotational inertia attainable by the variable effective mass unit
\mathbf{K}	Device stiffness matrix
\mathbf{K}_L	Device stiffness matrix found in the linear mathematical model
L	Length of inertial arm
\mathbf{M}	Device mass matrix
\mathbf{M}_L	Device mass matrix found in the linear mathematical model
N	Level of the perturbation method
N_{max}	Total number of levels in the perturbation method solution
N_{arm}	Number of inertial arms in variable effective mass unit
P_{avg}	Average absorbed power
$Pr(H_r \geq H_{lim})$	Probability that H_r exceeds H_{lim}
R	Spar hull radius
Q	Perturbation method's constant coefficient matrix
T	Oscillation period
T_e	Energy period
X,Y,Z	Cartesian coordinate system, where Z is zero at mean water height and positive upward

\vec{a}	Complex water particle acceleration amplitude
c_g	Generator damping coefficient
c_j	Damping coefficient for body j
$c_a(\omega)$	Damping coefficient representing the viscous drag effects and radiation damping
$\mathbf{f}_e(t)$	Wave excitation force in time
$\vec{\mathbf{f}}_e(\omega)$	An array of complex excitation force amplitudes on each of the device's bodies
$\vec{\mathbf{f}}_{e,f}(\omega)$	Complex excitation force amplitude on the float body
$\vec{\mathbf{f}}_{e,r}(\omega)$	Complex excitation force amplitude on the reaction mass body
$\vec{\mathbf{f}}_{e,s}(\omega)$	Complex excitation force amplitude on the spar body
g	Gravity
h	Depth of water
i	Imaginary number
$\underline{\mathbf{i}}, \underline{\mathbf{j}}, \underline{\mathbf{k}}$	Unit vectors in the direction of x, y, and z, respectively
k	Wave number
l	Ball screw lead
k_j	Hydrostatic stiffness of body j
m_j	Mass of body j
$m_4(t)$	Effective mass variation
$m_a(\omega)$	The frequency dependent added mass
m_∞	The asymptotically approached added mass as ω goes to infinity
m_{max}	Maximum attainable effective mass by the variable effective mass unit
m_n	The n^{th} spectral moment of a variance density spectrum
m_{rod}	Mass of variable effective mass unit's inertial arm
$p(H_r)$	Relative travel height probability density function
r_{bs}	Radius of ball screw
r_{rod}	Radius of inertial arm
t	Time
\vec{v}	Complex water particle velocity amplitude
x,y,z	Cartesian coordinate system
$\underline{z}(t)$	The heave motion of a device's bodies
$\underline{z}(t)_N$	The perturbation method's N^{th} level solution to the device motion

$z_f(t)$	The float's heave motion response
$z_r(t)$	The reaction mass's heave motion response
$z_s(t)$	The spars's heave motion response
z_P	Depth at which the water particle velocity and acceleration are considered to interact with the body
\Im	Imaginary portion of a complex value
\Re	Real portion of a complex value
$\alpha_A(t)$	Rotational acceleration about a point of interest on the device's variable effective mass unit
ϵ_0	Effective mass linear offset
ϵ_1	Effective mass variation amplitude
$\vec{\zeta}_N^{(j)}(\omega)$	An array of complex oscillation amplitudes for solution component j on the N^{th} level
$\vec{\zeta}_f(\omega)$	Oscillation amplitude for the float body
$\vec{\zeta}_r(\omega)$	Oscillation amplitude for the reaction mass body
$\vec{\zeta}_s(\omega)$	Oscillation amplitude for the spar body
$\theta(t)$	Rotation angle of variable effective mass' inertial arms
$\underline{\theta}_N^{(j)}$	Array of body phases in respect to time zero for component j of the N^{th} level of the solution
θ_f	Float phase in respect to time zero
θ_r	Reaction mass phase in respect to time zero
θ_s	Spar phase in respect to time zero
ρ	Density
τ	Torque
τ_A	Torque about a point of interest on the variable effective mass unit
ϕ_1	Effective mass phase lag
$\Omega(t)$	Rotational velocity of ball screw
ω	Oscillation frequency
ω_c	Effective mass variation control frequency
ω_i	Incident wave oscillation frequency
ω_j	Oscillation frequency of solution component j
ω_s	Frequency at which dry oscillator added mass and damping coefficients are assessed
$\omega_A(t)$	Rotational velocity about a point of interest on the device's variable effective mass unit

ACKNOWLEDGEMENTS

This work would not have been possible without the insight and support of many people. I would like to express my sincere gratitude to Dr. Brad Buckham, who offered a great deal of patience, guidance and encouragement from beginning to end, and who opened new doors when I hit dead ends. I would like to extend many thanks to my office mate, and great friend, Scott Beatty for providing me with invaluable support, reassurance and knowledge throughout my research. I would also like to thank my many friends and colleagues within the Mechanical Engineering Department, who invested in my thesis with their time, experiences and constructive criticism, and who were able to provided a good laugh when I needed it most. Finally, I want to acknowledge my family, whose constant encouragement made this experience possible.

Chapter 1

Introduction

Harnessing and converting the motion of ocean waves into useful energy has long been a desire of human-kind, with wave energy conversion patents dating back more than two centuries[1][2]. Interest in wave conversion technology increased during the oil crisis of 1973, and recent climate change concerns have re-energized the wave energy sector. This has resulted in the development of a wide variety of conceptual devices, and methodologies for the analysis of these devices, including the development of physical or numerical modelling strategies. Despite these efforts, wave energy converter (WEC) design has yet to converge on a commonly accepted optimal design or optimal control strategy that ensures economically competitive extraction from ocean waves. A very simplistic view of the operation principles for a select few of the widely varying design concepts currently being pursued internationally are given in Figure 1.1. These devices differ greatly in the manner by which water particle motions are used to excite the device, how each device absorbs energy, and their physical size and orientation.

Unfortunately for the field of wave energy research, the trial and error development of these concepts is not an economically viable option. Alternatively, to achieve an accurate assessment of the complete device dynamics, for a specified sea-state, developers are forced to use numerical dynamic simulations or device scaled tank tests. Both of these approaches can allow for the device's non-linearities, such as mooring and frictional forces, to be accurately represented on a repeated basis. Both approaches are thus important to the development of a device prior to installation into an ocean environment. Unfortunately, because of the computational time required to fully characterize these devices in a detailed numerical simulation, the build

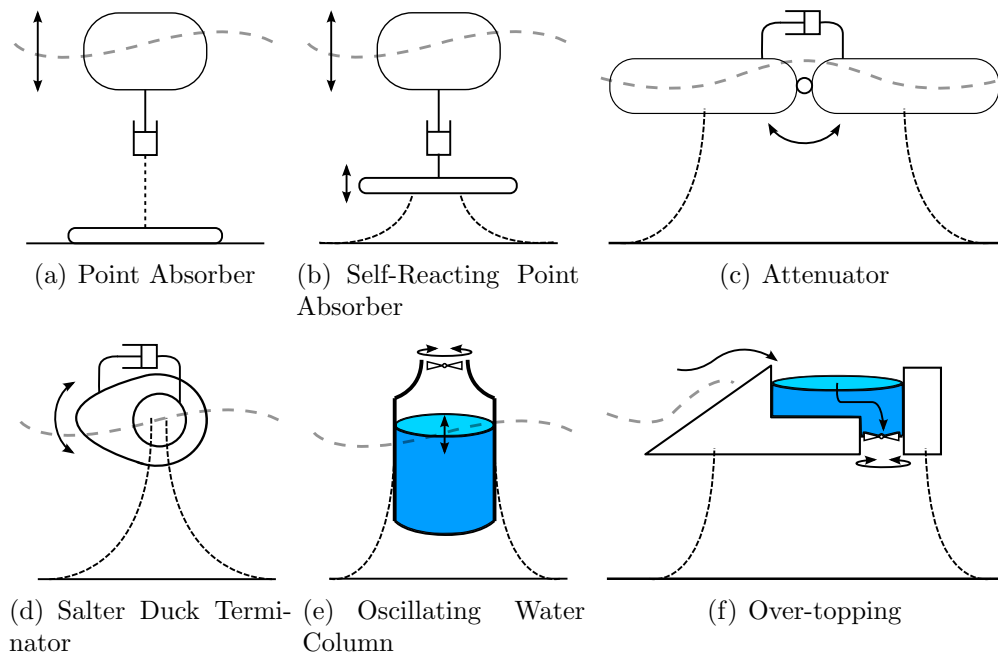


Figure 1.1: A select few of the differing wave energy converter devices currently undergoing research internationally. The power take-off for these devices is represented as a viscous dashpot or spinning turbine.

time required to create a representative scaled physical devices and inherent difficulty properly scaling the physical model these tools are often not exploited early in the design process.

Rather, high fidelity device numerical models are further idealized to create a mathematical model that uses linearized approximations of non-linear forces and only considers the motions associated with power conversion. These simplifications allow for computational time associated with a single numerical experiment to be significantly reduced and allows a large number of device geometries or control techniques to be evaluated in a short period of time.

Idealized mathematical models can be executed in the time-domain or the frequency-domain. Time-domain analysis techniques are commonly accepted for providing an accurate approximation of the transient device response and is the method of choice for relatively direct analysis of a device's response to time-varying control parameters. Although these techniques are significantly faster than a full numerical dynamic simulation, they are computationally heavy in comparison to frequency-domain techniques

and the detail provided in the solution envelopes a few key performance metrics that tell the WEC designer much of the design or control concept being considered. As a result, post-processing of the response is often necessary to extract the meaningful metrics upon which design decisions can be based. Alternatively, frequency-domain based techniques are often used to determine the steady-state response of a device under both regular and irregular waves. These techniques provide a computationally ‘light’ response calculation that requires little to no post processing to interpret. This allows for a large number of physical designs and control strategies to be evaluated in a finite time in a robust and automated manner. Frequency-domain models are often used in conjunction with an optimization algorithm that executes the comparison of a multitude of options. Unfortunately, current frequency-domain methods are incapable of analyzing the transient motion response of a device, such as the device’s response to changes in control actions. To converge on an optimal control strategy and optimal physical WEC shape and size prior to executing full numerical dynamics simulations, or construction of a physical scale model or prototype, frequency-domain WEC mathematical modelling needs to be improved so that control activity can be included in mathematical “trial and error” development of early stage concepts.

Widely varying and irregular ocean wave conditions make the selection of a device’s optimal physical parameters an indeterminate problem. An area of increasing importance is the means to control a WEC such that the amount of power absorbed by the device for a particular prominent wave being experienced at any given moment is maximized. Device control has the potential to both increase year-round device productivity, as well as reduce the size of a device at a specific nameplate capacity[3]. The control parameters used on a WEC vary widely depending on the type of device being analyzed; however, devices typically utilize adjustments within a hydraulic power take-off unit.

Numerous techniques have been proposed to optimally adjust a device’s control parameters. Linear control techniques consist of adjustments to a device’s control parameter to follow changes in the prevailing wave spectra on a time-scale of a half hour or greater. The control parameter changes are considered to occur outside the domain of the analysis and, because the transient response resulting from these parameter changes is much shorter than the time-scale in which the adjustments are made, they are considered to be “time-invariant” system parameters. These techniques can

be accurately analyzed using both time and frequency domain models, and can be implemented within an optimization routine with ease. Unfortunately, practical implementation of these techniques are unable to approach the theoretical maximum limits of power absorption in a real sea-state. Non-linear control techniques consist of WEC control parameter adjustments on a wave-to-wave time-scale, resulting in time-varying state-dependent system parameters in the dynamic equations. While such control is often suggested as a means to drastically improve power production, the device's response becomes highly non-linear[4]. Only time-domain methods are currently used to assess the transient response of the device. As suggested by Price, "Any model that can suitably represent transients can be adjusted to describe time varying response. Thus only the time domain wet oscillator is capable of representing an immersed body with time varying behaviour such as [non-linear] control." [5].

1.1 Motivation

The main motivation of this work is to refute the idea that the mathematical modelling of a WEC subject to a non-linear control strategy is strictly limited to the time-domain. If the control parameter is periodically varied in a regular sea-state, the system should reach a steady-state. Given persisting regular conditions, it is proposed that a frequency-domain analysis should be viable. This work aspires to build the capacity to analyze a device's response to periodically varied control parameters within the frequency-domain beginning with a regular wave condition. Literature in this field is very limited and it is not known if the computational benefits, and acceptance, of frequency-domain techniques for time-invariant control systems will translate to the time-variant paradigm. This thesis will provide clarity to that debate.

The proposed frequency-domain methodology could alter how industry evaluates WEC concepts at an early stage. First, the technique unifies the treatment of device shape and control, allowing control parameters to enter into an automated optimization process. Since the control of a device is inherently linked to the physical design of the WEC, the introduced methodology would allow for a large number of WEC physical parameters and control parameters to be quickly evaluated in unison, on the basis of maximum power absorption using a global optimization routine. A global optimization would guide the development of a particular device to converge on a physical design and an associated control technique that could then later be assessed

by a full numerical dynamic simulation or tank test.

Second, the technique is not device specific and could be applied to a variety of control techniques: methods applied for periodic variations of one WEC parameter could be directly applied to another choice of control parameter. Using a frequency-domain approach, the steady-state device response will be represented as several motion components each of a unique frequency, phase, and amplitude. This representation of the response, as opposed to a time series that must be post-processed, is thought to provide a more direct and robust basis for the evaluation of the device's performance.

1.2 Thesis Objectives

The high-level objective of this thesis is to expand the accepted domain of WEC frequency domain analysis so that it encompasses the analysis of control strategies that employ time-variation of a WEC's physical control parameter.

Towards that objective, the first task is to develop a set of dynamics equations that capture the dynamics of a representative WEC device with a single time-varying physical control parameter. The second task is to develop a new methodology for obtaining the steady-state motion response of the device in the frequency-domain and ensure its validity via comparison to numerically integrated time-domain results. Third, the computational efficiency of the proposed methodology must be evaluated, and, if needed, steps taken to ensure the methodology maintains the superior computational efficiency relative to traditional time-domain methods; the main benefits of frequency-domain analysis, its speed and succinctness, cannot be compromised.

Fourth, a means to translate the steady-state motion response information, embedded in a series of individual motion components, into an estimate of the gross absorbed power of the device must be provided. To be consistent with existing frequency-domain approaches, the gross power absorption calculation should avoid subjective post-processing of time series data, and account for losses associated with the energy required to complete the physical parameter variation under consideration.

Finally, a closed form means to determine if a device's physical constraints are being violated, relative travel constraints for example, should be provided. Again, to be consistent with existing frequency-domain approaches, it is desired that the constraint analysis can be evaluated in a closed form manner to avoid post processing of time-series data.

1.3 Literature Review

1.3.1 Wave Energy Converter (WEC) Technology

Despite the decades of research and progress made in wave energy research, ocean wave energy conversion technology is still fairly immature. In comparison to other renewable technologies, such as wind turbines, wave energy has yet to converge on a commonly accepted method of extracting energy. A WEC's ultimate goal is to maintain a high capture width and survivability in the ocean environment while offering a competitive capital cost [6]. There are a large number of physical mechanisms through which ocean wave energy can be harvested: a device proximal to shore experiences the wave break, while a device offshore uses the water particle motion to excite the power take-off. Research in the field must narrow in on which devices perform best in each scenario, and then determine which scenario provides the most opportunity.

As a result of the various different principles of extraction, there are many different classifications of devices. Early work in the wave energy field led to a classification system based around floating WECs [6]. Devices were classified under one of the three types: attenuator, terminator or point absorber. The classification system was intended to give an idea as to the geometry of the device and its principle of operation.

Attenuator devices are oriented parallel to the propagation direction of the incident waves, whereas terminator devices are aligned perpendicular to the direction of propagation. Attenuator devices generally span one or more incident wave lengths. As an ocean wave passes, sections of a floating body move relative to one another, as in Pelamis¹ shown in Figure 1.3, or floats of an articulated body rise and fall, as in Wave Star². If an attenuator is subject to waves perpendicular to the principal

¹www.pelamiswave.com

²www.wavestarenergy.com

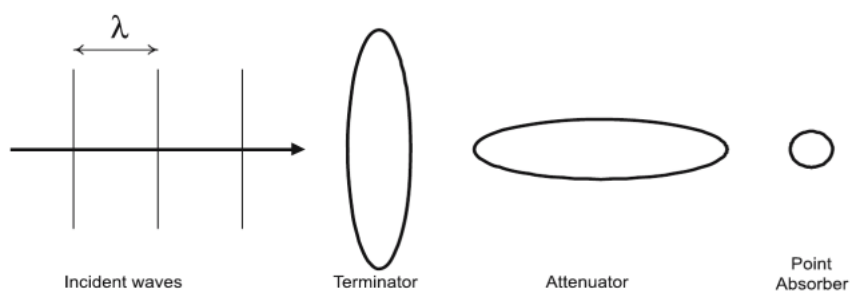


Figure 1.2: Classification of Floating Wave Energy Converters[6]

axis of the structure, it does not function as efficiently and the moving structure is often designed to allow some compliance such that the attenuator can re-orient with changes in the wave field's principal direction. Terminators can either be a fixed, as in overtopping devices, or compliant – the device does not resist the motions induced by incident waves, as in the Salter Duck array [7].



Figure 1.3: The P2 Pelamis is an attenuator made up of five connected bodies totaling 180m in length and 4m in diameter. Each of the WEC's joints contain a power take-off to convert the bodies relative motion into electricity(www.pelamiswave.com).

Overtopping devices, such as the WaveDragon³, are essentially a low-head hydro system. Large 'arms' are used to focus incoming waves towards a central collection location. The basin collects the water that crashes over top of the basin wall where it is maintained at a higher elevation than the surrounding ocean surface. This potential energy is captured as the water falls back to the surrounding ocean surface and passes through a turbine.

³www.wavedragon.net

Oscillating water column (OWC) WECs utilize an inverted chamber that holds an water-air interface with the air captured at the top of the sealed chamber. The motion of the ocean waves cause the level of water column in the chamber to rise and fall, this in turn causes the air in the chamber to compress or expand, respectively. A turbine in series with a small air valve that is actively controlled and captures the kinetic energy of the air as it enters or escapes the chamber. One such device is OceanLinx's MK1⁴ shown in Figure 1.4. OWC devices can be placed on-shore or off-shore. Though similar in operation principles, OWC on-shore devices are classified as terminators, where as the off-shore OWC devices are often referred to as members of the point absorber classification, discussed below.



Figure 1.4: The OceanLinx MK1 was a 500 tonne oscillating water column WEC installed in Port Kembla, Australia, in 2005(www.oceanlinx.com).

⁴www.oceanlinx.com

Point absorbing WECs are a floating body, typically axis-symmetric along the vertical axis, and have a small horizontal cross-section relative to incident wave lengths. A valuable attribute of point absorbers is their direction independence. Unlike attenuators and terminators, the axis-symmetric hull structure of a point absorber ensures excitation created by waves from different directions is consistent. The simplest form of a point absorbing device, given in Figure 1.1(a), is a floating single-body device that drives an ocean floor fixed electromechanical or hydraulic power take-off, as in Carnegie Wave Energy's CETO⁵ shown in Figure 1.5.



Figure 1.5: Carnegie's CETO III is a one-bodied point absorber located off the shores of Garden Island in Western Australia (www.carnegiewave.com).

Alternatively, a self-reacting point absorber captures energy by means of relative motion between two floating bodies, as in Figure 1.1(b). Self-reacting point absorbers are restrained by a compliant mooring that, in ideal circumstances, doesn't

⁵www.carnegiewave.com

impact the hydrodynamics of the point absorber's floating components. In the field of wave energy research, there is some debate on optimal self-reacting point absorber design[8][9]. One approach, used by the OPT PowerBuoy⁶ shown in Figure 1.6, is to use a second body, a spar buoy, with a large damper plate at its bottom end to approximate a fixed platform for the first body, a float, to react against. Alternatively, the second body can be used act in counter-phase to the float to generate increased relative motion, as in WaveBob⁷. Self-reacting devices are favoured over their fixed sea-floor counterparts because of their improved ability to survive extreme waves and naturally compensate for tidal free surface elevation changes via compliance of the mooring structure. In extreme waves, a self-reacting WEC's mooring allows potentially damaging waves to pass by without causing large relative travel, and subsequent end-stop collisions, to occur[10]. As a result, proponents of self-reacting devices claim less structural strength need be built into device components, providing significant cost reduction[11].



Figure 1.6: Ocean Power Technologies' P150 PowerBuoy is self-reacting point-absorber rated at a capacity of 150kW. The device is shown horizontally prior to installation off Scotland's northeast coast in 2011 (www.oceanpowertechnologies.com).

Unlike most other devices, point absorbers tend to have a relatively narrow bandwidth where the device effectively absorbs the energy present in the ocean surface. As a result, a large portion of wave energy literature pertaining to device control focuses varying the mechanics of point absorbers such that they remain effective over a large range of sea-states[12][4][13][14]; For point absorbing WECs, the need for wave-to-

⁶www.oceanpowertechnologies.com

⁷www.wavebob.com

wave control is critical, and for this reason the device considered in this thesis is a representative point absorber concept. The methodology provided within this work could be extended to other point absorbers provided they can be cast within the mathematical framework presented in Section 1.3.2.

1.3.2 Mathematical Modeling of Immersed Body Oscillation

In this section the established assumptions that simplify a complete high fidelity representation of a point absorber to a reduced order mathematical model are presented. Two different governing equations for an immersed - surface piercing or floating - body subject to the free surface oscillations are presented, and their differences and limitations are discussed. The material presented here will provide background on modeling the wave excitation forcing, the body hydrodynamics, and the response of an immersed body subject to a regular wave. This material will be extended in Section 2.1 to develop a new methodology for analyzing time-varying control techniques in the frequency domain.

If the extension of the immersed body in the horizontal plane in the direction of the incident wave propagation is much smaller than the incident wave length and the displacements of the immersed body along the vertical axis of motion are small, the small body approximation can be applied [15]. This approximation neglects any variation of surface elevation and fluid acceleration over the width of the body in the horizontal plane, as well as, any pitching motion produced from the form drag of elliptical water particle motion across the immersed body and, as a result, allows for any rotation or displacement of the body in the horizontal plane to be neglected. This results in a heave-constrained model, where only the motion along the vertical axis is taken into consideration.

The excitation force on an immersed body due to an assumed sinusoidal incident wave of frequency ω is split into two terms; the Froude-Krylov force and the diffraction force. The Froude-Krylov and diffraction forces on an immersed body are a result of the hydrodynamic pressure of an undisturbed incident wave and the forces affiliated with the wave diffracted by the body, respectively [6]. Computing these forces normally requires both volume and surface integration of pressure distributions; how-

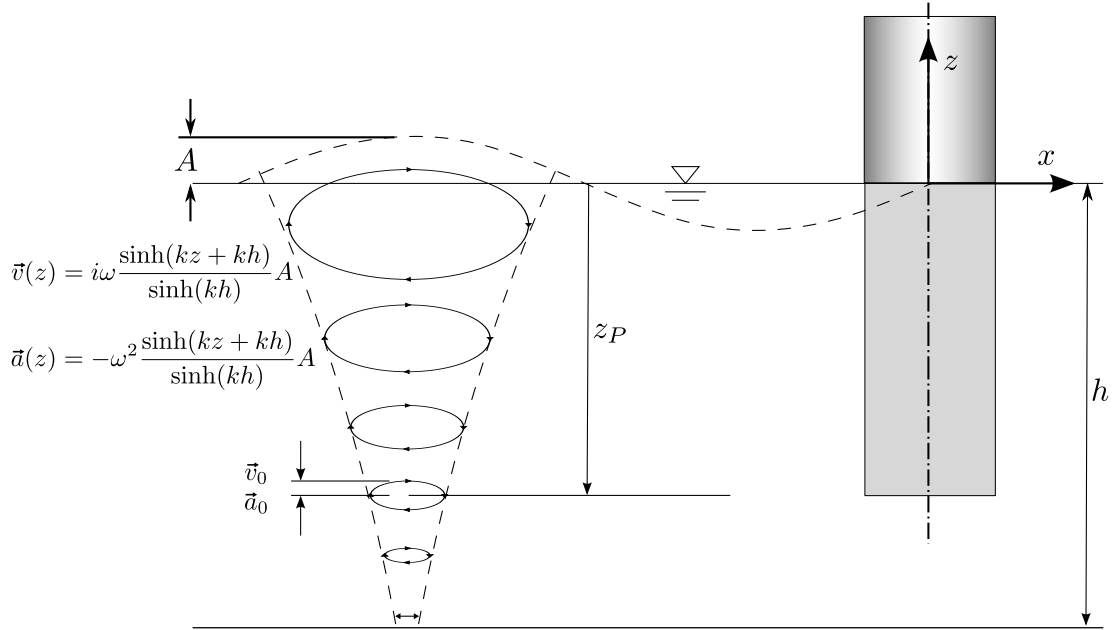


Figure 1.7: Orbital fluid particle motion of Airy waves. The expressions for vertical particle velocities and accelerations are both time and depth dependent, given by $v(z, t) = \vec{v}(z) \cos \omega t$ and $a(z, t) = \vec{a}(z) \cos \omega t$ respectively.[16]

ever, the small body approximation neglects the variation of the pressure distribution along the horizontal plane of the body resulting in much simpler expressions[15]. The excitation force of a sinusoidal Airy wave on an immersed body along the heave axis is expressed as:

$$f_e(t) = \Re \left\{ \vec{f}_e e^{i\omega t} \right\} \quad (1.1)$$

The complex amplitude of the force excitation is given by

$$\vec{f}_e(\omega) = [(m + m_a(\omega)) \vec{a}_0 + c_a(\omega) \vec{v}_0 + kA] \quad (1.2)$$

The first term on the right-hand side of Equation (1.2) is proportional to the devices true mass m and is associated with the pressure gradient of the accelerating fluid in the undisturbed wave integrated over the wetted surface of the immersed body and represents an effect similar in nature to a buoyancy force. The frequency dependent added mass, $m_a(\omega)$, is associated with an additional pressure gradient required to accelerate the fluid surrounding the immersed body around the impermeable hull[17].

The velocity dependent term on the right-hand side of Equation (1.2) represents the cumulative forces acting on the immersed body due to the velocity of the surrounding fluid, \vec{v} , including viscous drag effects and the force due to the radiated waves which is dependent on the damping coefficient, $c_a(\omega)$. The final term on the right-hand side of Equation (1.2) is associated with the hydrostatic pressure changes over the submerged hull that result from the changing surface elevation of the fluid.

The acceleration and velocity of the fluid particles in the undisturbed wave will vary greatly depending on the depth of the particle under consideration. This is of particular importance for devices with components that have a large draft – a characteristic that is wide spread in self-reacting point absorbers. In the linear wave theory proposed by Sir George Biddell Airy, the water particle accelerations and velocities can be expressed as a function of the depth, incident wave frequency, wavenumber, and water depth, as shown in Figure 1.7 [18]. This relationship was found assuming small amplitudes, linearizing the surface boundary condition, and solving the Laplace equation for potential flow. His results allow the amplitude of the forcing function of Equation (1.2) to be expressed at the immersed body's reference depth, z_P – the depth at which the water particle velocity and acceleration are considered to interact with the body:

$$\vec{f}_e(\omega) = \left[-\omega^2(m + m_a(\omega)) \frac{\sinh(kz_p + kh)}{\sinh(kh)} A + i\omega c(\omega) \frac{\sinh(kz_p + kh)}{\sinh(kh)} A + kA \right] \quad (1.3)$$

Wet Oscillator Model

The dynamics of the immersed body reacting to the incident wave forcing can be modelled in two separate ways; using a wet oscillator or a dry oscillator model. Presented below is a frequency domain wet oscillator model of an immersed body subject to incident waves.

$$\vec{f}_e(\omega) = -\omega^2[m + m_a(\omega)]\zeta(\omega) + i\omega[c + c_a(\omega)]\zeta(\omega) + k\zeta(\omega) \quad (1.4)$$

This model uses the small body approximation described earlier to assume the motion of the immersed body is purely along the heave axis of motion, where $\zeta(\omega)$ is Fourier transform of the body's post-transient amplitude heave response. The complex amplitude of the excitation force, $\vec{f}_e(\omega)$, is as described in Equation (1.3). The coefficients m , c , and k are the true mass, damping, and stiffness associated with

heave displacements of the immersed body in quiescent fluid, respectively. For a simple immersed body the damping coefficient, c , would be set to zero. However, if the body is to represent a point absorber with a hydraulic power take-off unit, this term must be present to capture the viscous behaviour of the power take-off unit. The power take-off unit is often modelled as a linear viscous dashpot[6]; while a practical implementation of the linear damper is not realistic, several high pressure accumulators could be used to approximate a continuous linear damper, as suggested by Babarit in [19].

In the wet oscillator model, the added mass and damping terms, m_a and c_a respectively, are shown to be functions of the incident wave frequency ω . These terms represent the waves shed by a heaving body in a quiescent fluid - these waves persist and effect the body's motion in the future. To produce a time-domain equivalent of the wet oscillator model, Equation (1.4) is rearranged to a form where the multiplication of frequency dependent functions are grouped:

$$\vec{f}_e(\omega) = -\omega^2[m + m_\infty]\zeta(\omega) + i\omega B(\omega)\zeta(\omega) + k\zeta(\omega) \quad (1.5)$$

Where

$$B(\omega) = [c + c_a(\omega)] + i\omega[m_a(\omega) - m_\infty] \quad m_\infty = \lim_{\omega \rightarrow \infty} m_a(\omega) \quad (1.6)$$

Applying an inverse Fourier transform reveals a time-domain convolution of the device's radiation impedance with the velocity of the body through the still fluid, whereas calculation of the post-transient response with the frequency domain model requires only multiplication.

$$f_e(t) = [m + m_\infty]a(t) + \int_0^t B(\tau)v(t - \tau)d\tau + kz(t) \quad (1.7)$$

Equations (1.5) and (1.5) are commonly referred to as the Cummins decomposition [20].

This convolution correctly models the radiation memory of the device and, as such, both the frequency domain model presented here and the equivalent time-domain wet oscillator model with the convolution integral are able to correctly evaluate a body's

response to polychromatic waves. In established works, the frequency-domain wet oscillator model is strictly limited to the post-transient oscillation of the device, while the time domain model is capable of analyzing the transient response as well[5].

Dry Oscillator Model

Similar to the wet oscillator model of the previous section, the dry oscillator model given in Equation (1.8) also includes the added mass and damping terms [5]. However, this model uses added mass and damping coefficients associated with a particular frequency of oscillation, ω_s , and assumes that these coefficients are applicable across the frequency bandwidth[5].

$$\vec{f}_e(\omega) = -\omega^2[m + m_a(\omega_s)]\zeta(\omega) + i\omega[c + c_a(\omega_s)]\zeta(\omega) + k\zeta(\omega) \quad (1.8)$$

Unlike the wet oscillator model, the inverse Fourier transform of the dry oscillator model does not contain a multiplication of two frequency dependent terms and, as a result, the equivalent time-domain model contains only constant coefficients:

$$f_e(t) = [m + m_a(\omega_s)]a(t) + [c + c_a(\omega_s)]v(t) + kz(t) \quad (1.9)$$

Both the time and frequency domain dry oscillator models presented above are capable of analyzing the post-transient response of the immersed body. However, as shown, the dry oscillator model does not include the convolution integral present in the wet oscillator model. As a result, the dry oscillator model is not capable of correctly modeling the radiation memory of the device. This limits both the time and frequency domain dry oscillator models to monochromatic waves and limits the time-domain model to the post-transient response of the immersed body. Price suggests, “Here correctness is qualitative, rather than quantitative. For [immersed bodies] that are small compared to typical wave lengths, a dry oscillator may simulate polychromatic behaviour to an acceptable degree of accuracy” [5].

1.3.3 WEC Control

A combination of widely varying and irregular ocean wave conditions, and a multitude of WEC designs and WEC control concepts, make the selection of WEC physical parameters which allow the device to absorb the largest amount of energy an inde-

terminant problem, and there is yet to be a convergence of modern point absorber designs.

Within a point absorber's operational bandwidth, device operation tends to be optimal at an incident wave period that is proximal to that of a power producing mode of motion. When not operating within the optimal bandwidth, the WEC's response is attenuated. Oscillating attenuators and terminators have the advantage of having a rather broad operational bandwidth, whereas point absorbing devices tend to have a narrow bandwidth where the device performs well. As a result of the large variation in sea-states over the course of a given year, point absorbing WECs will typically be operating outside their resonant bandwidth[4]. This requires the point-absorber to utilize control techniques to maximize power conversion, whereas the benefits of applying control techniques to attenuators and terminator devices, with their larger resonance bandwidths, may result in only marginal improvements[21].

Linear Control

Optimum control of WECs has long been a subject of a research in the field of wave energy. Early work was concentrated on linear control, in which the change in control parameter can be considered time-invariant in the mathematical model: adjustments are made and then held constant over a 30 minute to one hour period. Linear control does not result in the introduction of any further frequencies into the response of the device, and can be analyzed and optimized relatively quickly in the frequency-domain.

Early theoretical studies have shown that for a resonant point absorber in regular waves the maximum amount of absorbed energy from an incident wave is the energy associated with a wave-front that is one wave-length divided by 2π wide[22]. To compare the response given by one set of control parameters to the response given by another, the metric of average absorbed power by the device is often used. To obtain optimal power absorption by a single mode, one degree of freedom, device subject to regular waves, two conditions must be satisfied:

1. The velocity of a device oscillating in one mode must be in phase with the excitation force.
2. The amplitude of the oscillating device must be such that the destructive interference between the re-radiated wave and the incoming waves is at its greatest.

For a single mode device operating in a resonant condition, the first condition is automatically satisfied. In the existing wave energy literature, it has been shown that the resonant condition is achieved when the impedance of the power take-off device equals the complex conjugate of the WEC's mechanical impedance with respect to the incident wave[4]. Where the internal impedance is a complex entity comprised of the body's mechanical, power take-off loss, and radiation impedances. To achieve the complex conjugate of the WEC's mechanical impedance across the power take-off unit it may be required introduce inverse spring force behaviour into the power take-off mechanics. As result, the instantaneous power conversion may be reversed for short periods of time during the oscillation of the device[23]. For this reason this type of control is called "reactive control". This short period of time where the power take-off is operating in reverse will result in a negative power flow; however, it will theoretically put the device within it's resonant bandwidth and ideally capture an increased net power absorption. These theoretical analysis often do not account for any losses that are present in the power take-off and do not take into consideration the physical constraints of the device, including the power take-off. As a result, the constant reciprocation losses of the power take-off may result in a net negative power absorption over time. Adjustments made to the stiffness, viscosity, and/or inertia of the power take-off on a 30 minute to one hour basis and, as a result, can be modelled as a steady state system without introducing multiple response frequencies. It is important to note that these optimal conditions are for a device who's oscillation amplitude is unconstrained.

Optimal power absorption for a WEC oscillating with more than one mode, multi-body or irregular waves, may not follow the same conditions. A self-reacting point absorber operating in heave is an example of a device with more than one mode of oscillation, it has the equivalent of a two modes (each body is responsible for a mode of oscillation). For an axisymmetric self-reacting point-absorber, an equivalent one-body mathematical model can be created for the two-body system by considering only the relative heave motion between the bodies. Using this approach for a regular wave when complex impedance condition is met, it has been shown that equivalent optimal power absorption conditions for the one mode system hold true for the self-reacting system and the device could absorb the theoretical maximum of the wave power associated with a wave-crest that is equivalent length of the wave-length divided by 2π [8].

For real sea-states, optimizing a devices power take-off impedance for optimal power absorption at each frequency in a linear manner is not possible. One technique, sea-state tuning, adjusts the power take-off impedance such that it optimally absorbs the most power over the incident wave spectra[24][9]. To correctly model the response of the device in an irregular sea-state, the wet oscillator model presented in Section 1.3.2 must be used, whereas the a dry oscillator model is suffice for a linearly controlled device in a monochromatic sea-state.

Non-Linear Control

As presented by Falnes in [4], the use of non-linear control techniques are capable of drastically increasing the power absorbed by a device. These techniques introduce time-varying control parameters that result in the introduction of more than one oscillation frequency in the response. As a result, to correctly model these devices, a wet oscillator model should be used.

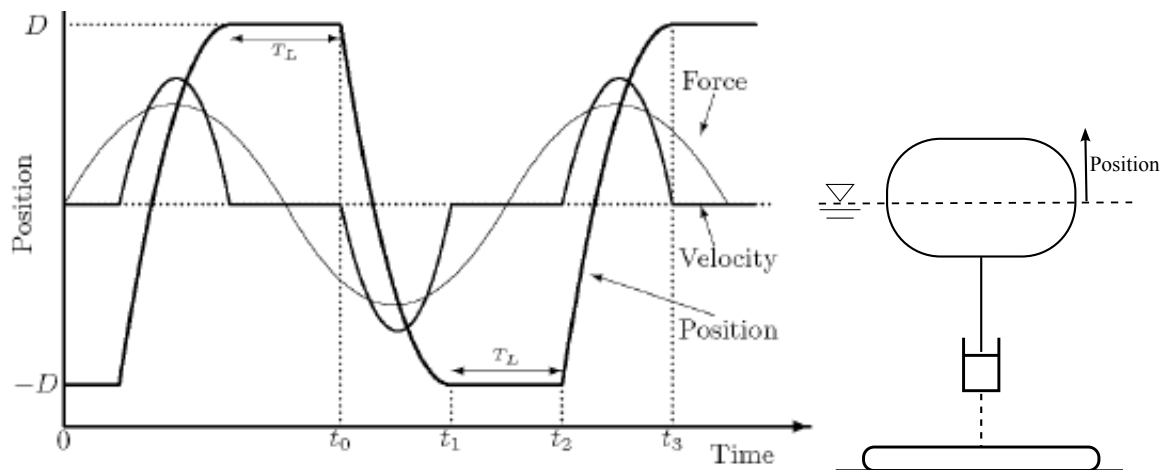


Figure 1.8: Latching control matches the phase of the forcing wave by holding the device fixed at the end of an oscillation for a latching period, T_L . [25]

One form of non-linear control, proposed by Budal and Falnes for a heaving point-absorber, is “latching control” [26]. This technique does not fully meet the requirement conditions discussed above and, as a result, is sub-optimal. However, the benefit of this technique is that it is passive. That is, it does not require the reversal of power flow and does not incur the losses associated with reactive control. Latching control

consists of locking the motion of the device at the exact moment when heaving motion of the device is at the end of an oscillation and the velocity of the device vanishes. The device is then held in position until being released at an optimal time to maximize power absorption, Figure 1.8. This type of control is advantageous when the period of incident waves is longer than the natural period of the wave energy converter. If one attempts to minimize device tonnage, this will generally be the case[27]. The optimal amount of time that the system remains locked is highly dependent on the sea-state and is an area of continued research in the field of wave energy. In real sea conditions, irregular waves, it noted that this type of control requires prior knowledge of the approaching incident waves to make an optimal decision. This type of control is referred to as “causal”. The duration of the advance knowledge of the wave field required to make this decision is on the order of half of the eigen period of the wave energy converter[4].

Similar to latching control, another phase control technique called “de-clutching” or “un-latching” seeks to enact sudden changes in the power take-off mechanics. Originally proposed by Salter et al, the de-clutching control technique consists of setting the power take-off damping to zero for short periods of time, enabling the device to oscillate more freely with the forcing wave[28]. When an optimal length of time of free movement has occurred and the device is moving at a desired velocity, the power take-off is engaged and energy is absorbed[19]. As with latching control, this technique is sub-optimal and passive. This technique is often implemented when the incident wave period is shorter than the natural period of the device or in conjunction with latching control[27]. If latching and de-clutching are used in combination, the device’s latch is applied with the bodies velocity is zero and released at an optimal time. The device then goes through a relatively short period of power absorption prior being de-clutched and being allowed to stay within phase with the incident wave.

The relatively simple device geometries used, allowed the analysis these theoretically optimal control strategies to be done analytically. The mathematics involved in undertaking a similar analysis technique on a device with multiple modes of oscillation, or differing control mechanisms, becomes unmanageable. One approach to analyze these devices is to use a standard time-domain model of the WEC in conjunction with an optimization algorithm to determine the optimal path for the WEC’s time-varying control parameter. One such approach was done for a single mode de-

vice by Gunn et al. in [27]. In which, an optimization technique was used to generate an optimal input-output relationship between the wave forcing and the power take-off damping coefficient. Although, this work was used to validate the latching and de-clutching control techniques for a single mode device, the approach proposed in that work could be extended to optimize any control strategy.

1.3.4 SyncWave Case Study

The WEC considered in this work is a floating vertically-oriented point absorber device under development by SyncWave Systems Inc. and the Wave Energy Research Group at the University of Victoria. This device, shown in Figure 1.9, is a self-reacting point absorber and extracts energy from incident waves from the relative motion between the float and spar buoys using a hydraulic power take-off. A unique characteristic of the SyncWave device is an internal third body located within the spar. This internal body, a reaction mass, is supported via an elastic element inside the spar and is kinematically coupled to a variable inertia assembly via a ball screw. By expanding or contracting the radial position of rotating rigid arms fixed to the base of the ball screw, the rotational inertia of this assembly can be continuously adjusted. Due to the kinematic coupling with the reaction mass, the rotational inertia changes can dramatically affect the heave accelerations of the reaction mass and thus induce an additional translational inertia, or effective mass, for the reaction mass. The effective mass can be characterized using the lead of the ball screw, l :

$$m_4 = \frac{J}{l^2} \quad (1.10)$$

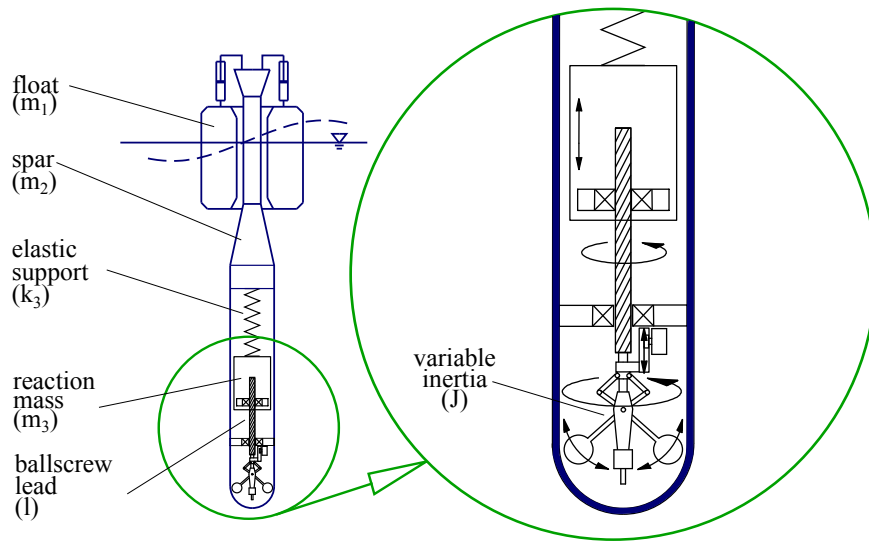


Figure 1.9: Schematic of the SyncWave WEC device.

The concept of the variable inertia unit is to ensure a strong tendency for relative motion of the spar and float, allowing for maximum electricity generation despite constantly changing frequencies and heights of incident waves. The variable inertia adjustments provide an additional control lever not found in most WECs. Using the variable effective mass and variable generator damping of the power take-off unit, initial performance estimates of the devices frequency response have been carried out by Beatty et al. [16] and Beatty [10] for regular waves and irregular seas. In those works an effective mass of the reaction mass and the hydraulic power take-off damping level, were determined on the basis of fixing the control parameter values for a persistent regular wave or a wave spectra. This constitutes a linear control action, and as a result was easily analyzed in the frequency-domain. The studies showed that the variable effective mass unit increased the power absorption over a simple two-body equivalent device for the majority of the operational bandwidth considered.

The SyncWave device has been selected as the basis for the development of the new frequency-domain mathematical modelling methodology as it includes the widest variety of possible time varying control parameters of the point absorbers considered in Section 1.3.1. As well, the device's variable effective mass unit has only been subject to linear control studies and, as a result, the full benefit of this extra control parameter is not yet fully understood. The development of this methodology will

serve as the foundation for future comparisons of the SyncWave device to other devices with non-linear control such as those given in [25] and [19].

It is important to note that the parameters characterizing the device used in this work are that of a scaled device intended for wave tank testing, differing from those used in previous studies, such as [16]. The WEC's parameters correspond to a 1:6 Froude scaled model of a proposed demonstration SyncWave device to be deployed in Hesquiaht Sound, British Columbia. A table of the scaled models parameters with corresponding full-scale parameters are given below in Table 1.1.

Table 1.1: Scaled SyncWave WEC Demonstration Device Parameters

Parameter	Model	Original
Mass (kg)		
Float Mass	139.1	25945
Spar Mass	410.2	76540
Reaction Mass	423.9	79100
Generator		
Control Range (Ns/m)		
Lower Limit	12.81136	1000
Upper Limit	128113.6	1.00E+07
Effective Mass		
Control Range(kg)		
Lower Limit	2512.932	468885
Upper Limit	13018.86	2429175
Relative		
Travel Limits(m)		
Spar-Slug Amplitude	0.525	3
Float-Spar Amplitude	0.4375	2.5

In the evaluation of device and control strategy performance it is important to utilize relevant combinations of wave heights and periods. Using a near-shore wave modeling software, REF/DIF, directional wave spectra have been computed at a monthly resolution over the course of a characteristic year for the community of Hot Springs Cove on the shore of Hesquiaht Sound, British Columbia[29]. This data has been synthesized and scaled for five off-shore positions located within Hesquiaht Sound using bathymetric data, shown in Figure 1.10 and Wave Watch 3 archives to propagate the off-shore data to each of the locations, as described by Hiles in [30].

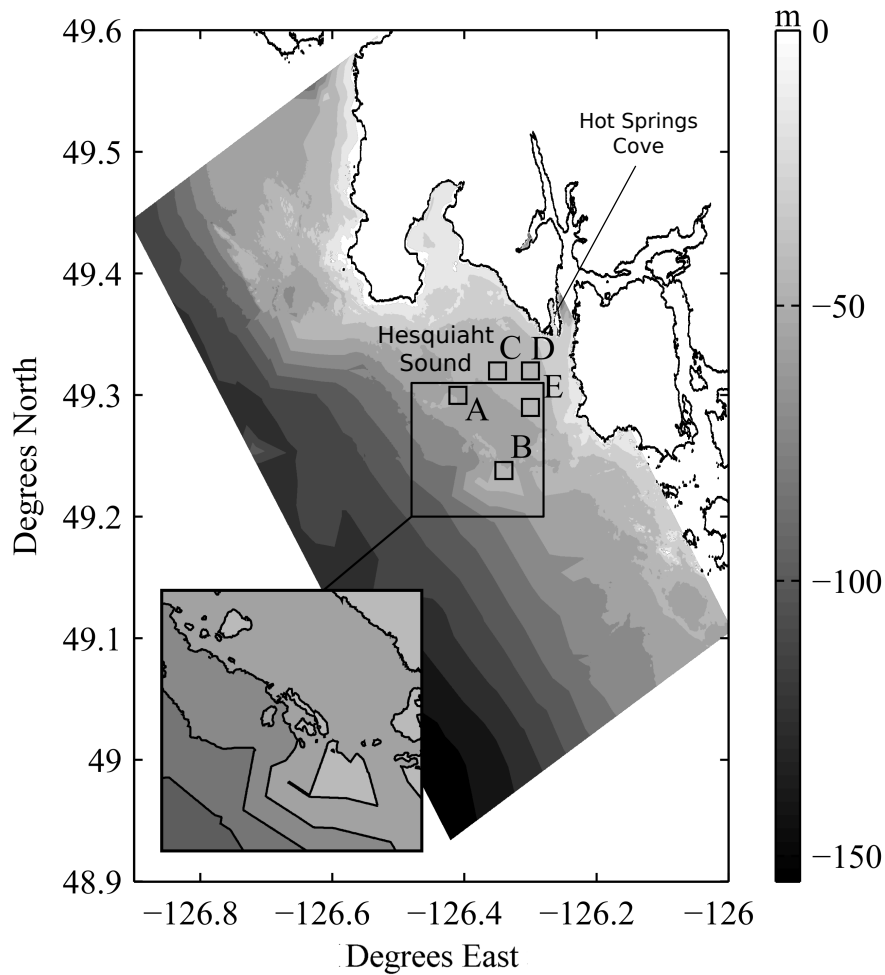


Figure 1.10: Bathymetric data for Hesquiaht Sound, British Columbia. Labeled are five potential test sites A-E.[29]

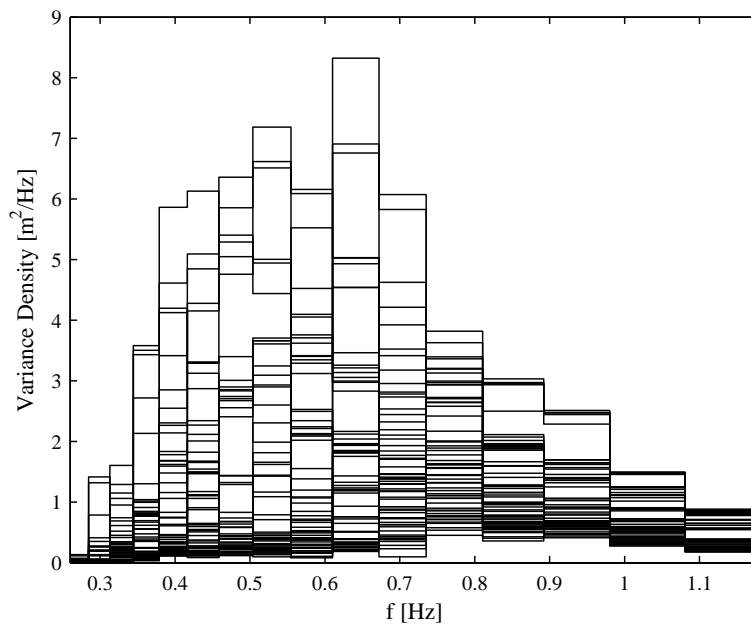
The monthly amplitude spectra for each of the five locations have been converted into variance density spectra and plotted below in Figure 1.11(a). The wide variation in the variance densities can be attributed to the dramatic changes in seasonal sea-state, as well as, the unique bathymetric profiles of each location. The variance density at each location has been used to determine a significant wave height, H_s , and energy period, T_e , for each month. This was done using the spectral moments of each locations monthly variance density spectrum, $E(f)$, according to Equation (1.11)[31].

$$m_n = \int_0^{\infty} f^n E(f) df \text{ for } n = \dots, -3, -2, -1, 0, 1, 2, 3, \dots \quad (1.11)$$

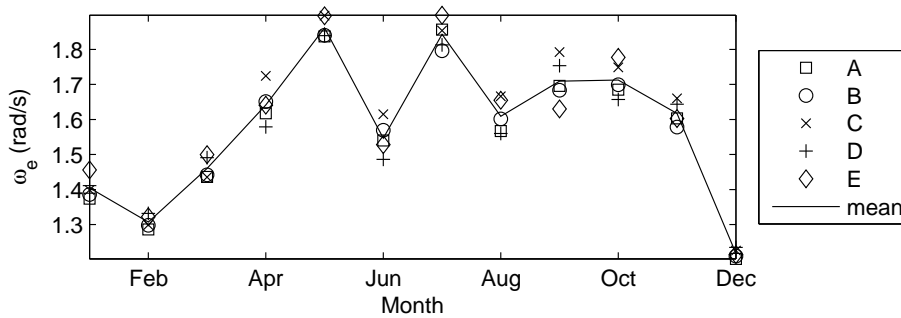
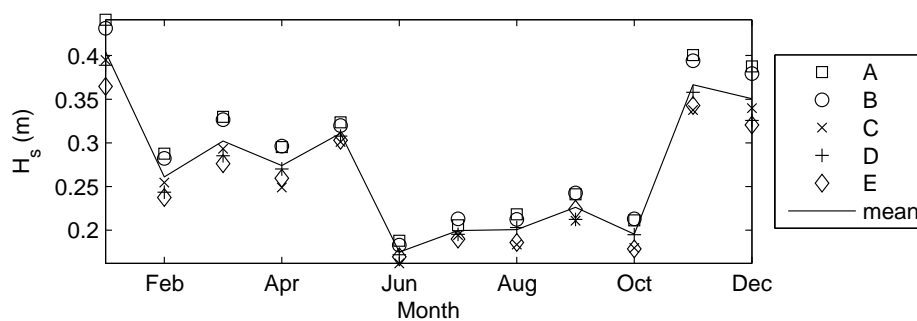
$$H_s = 4.004\sqrt{m_0} \quad (1.12)$$

$$T_e = \frac{m_{-1}}{m_0} \quad (1.13)$$

The significant wave heights and energy periods are then used to characterize a representative sea-state found in Hesquiaht Sound on a monthly basis, Figure 1.11(b).



(a) Variance Density Spectrum



(b) Monthly Significant Wave Height and Energy Period

Figure 1.11: Variance density spectrum and resulting monthly significant wave height and energy periods of a characteristic year for five potential test sites, ‘A’ through ‘E’, in Hesquiaht Sound, British Columbia [29].

1.4 Thesis Overview

For a case study, this thesis has focused its work with the SyncWave wave energy converter. As discussed in Section 1.3.4, this device was selected because of its large suite of control variables - not only a variable power take-off generator damping, but also an additional variable effective mass term - and the subsequent ability for the equations of motion modelling the SyncWave device to encompass most other vertically oriented point absorbers.

In Chapter 2 of this thesis, a mathematical model of a wave energy converter with a periodically-varying physical parameter is developed. It is shown why this model cannot be analyzed using standard frequency-domain techniques and a new methodology is developed to accurately approximate the response of the device to regular waves. In Chapter 3 an investigation into the computational efficiency of the methodology developed in the previous chapter is given. Techniques to drastically improve the efficiency of the solution process, with little-to-no loss in response accuracy, are proposed.

Through the proposed techniques, it is shown that of the hundreds of solutions components calculated in Chapter 2, only a small number are required to represent the device's motion response. In the final section of Chapter 3, this compressed representation of the device's relative travel is used to develop a closed form expression capable of evaluating if any physical travel constraint were violated.

Using the same compressed relative travel response representation, Chapter 4 develops the means to assess the absorbed energy through the power take-off in a closed form manner. The ability to evaluate the amount of energy required to actuate the inertial arms in the manner required by the desired fluctuation in effective mass control parameter is also developed in Chapter 4. In doing so, the ability to determine the average net power absorbed by the device can be analyzed.

Chapter 2

Mathematical Modelling of WECs

In this chapter a mathematical model is generated to analyze the SyncWave WEC, a vertically oriented point absorber described in Section 1.3.4, that is representative of a broader class of WEC concepts. An additional complication of the SyncWave technology is that a time-variant effective mass parameter exists in the equations of motion. The variation of this effective mass is akin to the more common variation of power take-off impedance, whether continuous or discontinuous, and so the process demonstrated here is not limited to this specific device; the techniques developed here are equally applicable for addressing the variation of any intrinsic physical property of a point absorber. A method for evaluating the steady-state motion of the time-variant system within the frequency-domain is presented and validated against a numerically integrated time-domain response for the same regular wave conditions. In Section 2.3 it is discussed how the current work is restricted to a periodic variation of the effective mass parameter subject to regular wave excitation of the WEC.

2.1 Governing Dynamic Equations

A mathematical model for the Sync-Wave device has been previously determined by Beatty in [10]. However, that model assumes that the WEC physical parameters are time-invariant, and thus the effective mass control parameter is only included in a linear manner. With the current investigation of time-variant effective mass behaviour this assumption is no longer valid, and the mathematical model used to describe the dynamics of the system must be adjusted.

Lagrange's equations are derived from the scalar quantities of kinetic energy, T , potential energy, V , and non-conservative forces, Q , of the system shown in Figure 2.1 and are of the form [32]:

$$\frac{d}{dt}\left(\frac{\partial T}{\partial \dot{q}_i}\right) - \frac{\partial T}{\partial q_i} + \frac{\partial V}{\partial q_i} = Q_i \quad (2.1)$$

Where

$$T = \frac{m_2 \dot{z}_s(t)^2}{2} + \frac{m_3 \dot{z}_r(t)^2}{2} + \frac{J(\underline{z}, t)}{2} \dot{\theta}^2 \quad (2.2)$$

$$V = \frac{k_3 z_r(t)^2}{2} + \frac{k_2 (z_r(t) - z_s(t))^2}{2} \quad (2.3)$$

In a real world implementation, variation of the rotational inertia control parameter, $J(\underline{z}, t)$, would be a function of both WEC state and time. The rotational velocity of the variable inertia assembly, $\dot{\theta}$, can be represented using the known kinematic coupling between the reaction mass and the ball screw:

$$\dot{\theta} = \frac{\dot{z}_s(t) - \dot{z}_r(t)}{l} \quad (2.4)$$

The non conservative forces, including the forces associated with drag, radiation damping and the external wave excitation, are given for both the spar and reaction mass in Equation (2.6). Because the reaction mass is located within the spar body, no hydrodynamic force is directly applied to body from an incident wave. For the purposes of this work, the radiation damping and drag forces, as well as the body mass and added mass, have been modelled as lumped constant coefficients, this approximation is discussed further in Section 2.2.

$$Q_s = -c_2 \dot{z}_s(t) + c_3 (\dot{z}_r(t) - \dot{z}_s(t)) + f_{e,s}(t) \quad (2.5)$$

$$Q_r = -c_3 (\dot{z}_r(t) - \dot{z}_s(t)) \quad (2.6)$$

Substituting Equation (2.2)-(2.6) into Equation (2.1), and carrying out the partial

differentiation with respect to z_s , z_r , \dot{z}_s , and \dot{z}_r as per Equation (2.1), yields:

$$\begin{aligned}
\begin{bmatrix} \underline{f}_{e,s}(t) \\ 0 \end{bmatrix} &= \begin{bmatrix} m_4(\underline{z}, t) + m_2 & -m_4(\underline{z}, t) \\ -m_4(\underline{z}, t) & m_4(\underline{z}, t) + m_3 \end{bmatrix} \begin{bmatrix} \ddot{z}_s(t) \\ \ddot{z}_r(t) \end{bmatrix} \\
&+ \begin{bmatrix} \dot{m}_4(\underline{z}, t) + c_2 + c_3 & -\dot{m}_4(\underline{z}, t) - c_3 \\ -\dot{m}_4(\underline{z}, t) - c_3 & \dot{m}_4(\underline{z}, t) + c_3 \end{bmatrix} \begin{bmatrix} \dot{z}_s(t) \\ \dot{z}_r(t) \end{bmatrix} \\
&+ \begin{bmatrix} k_2 + k_3 & -k_3 \\ -k_3 & k_3 \end{bmatrix} \begin{bmatrix} z_s(t) \\ z_r(t) \end{bmatrix} \tag{2.7}
\end{aligned}$$

This variation in effective mass is produced by adjusting the inertia in the variable inertia assembly and dividing by the ball screw's lead:

$$m_4(\underline{z}, t) = \frac{J(\underline{z}, t)}{l^2} \tag{2.8}$$

At this point, one must recognize that the state dependence is a choice of the WEC designer: the coupling of the effective mass variation to the WEC's motion is based on rules proposed by the human designer. In the process of searching for optimal control parameter variation, a wide range of dependencies should be considered. This is accomplished here by abandoning any explicit state dependence and considering only purely time-varying functions, $m_4(t)$. If an optimal variation of $m_4(t)$ can be found, one could extract optimal state relationships through observation of $m_4(t)$ and $\underline{z}(t)$. Adding the dynamics of the simply coupled float and removing control parameter variation state dependence results in the following matrix form of the WEC motion equations:

$$\underline{f}_c(t) = \mathbf{M}(t)\ddot{\underline{z}}(t) + \mathbf{C}(t)\dot{\underline{z}}(t) + \mathbf{K}\underline{z}(t) \tag{2.9}$$

Where,

$$\mathbf{M} = \begin{bmatrix} m_1 & 0 & 0 \\ 0 & m_4(t) + m_2 & -m_4(t) \\ 0 & -m_4(t) & m_4(t) + m_3 \end{bmatrix} \quad (2.10)$$

$$\mathbf{C} = \begin{bmatrix} c_1 + c_g & -c_g & 0 \\ -c_g & m_4(t) + c_2 + c_g + c_3 & -m_4(t) - c_3 \\ 0 & -m_4(t) - c_3 & m_4(t) + c_3 \end{bmatrix} \quad (2.11)$$

$$\mathbf{K} = \begin{bmatrix} k_1 & 0 & 0 \\ 0 & k_2 + k_3 & -k_3 \\ 0 & -k_3 & k_3 \end{bmatrix} \quad (2.12)$$

$$\underline{z}(t) = \begin{bmatrix} z_f(t) \\ z_s(t) \\ z_r(t) \end{bmatrix} \quad (2.13)$$

Where the regular wave excitation force on each body is represented as follows:

$$\underline{f}_e(t) = \begin{bmatrix} f_{e,f}(t) \\ f_{e,s}(t) \\ 0 \end{bmatrix} = \begin{bmatrix} |\vec{f}_{e,f}| \left[\frac{e^{i(\omega_i t + \theta_{e,f})} + e^{-i(\omega_i t + \theta_{e,f})}}{2} \right] \\ |\vec{f}_{e,s}| \left[\frac{e^{i(\omega_i t + \theta_{e,s})} + e^{-i(\omega_i t + \theta_{e,s})}}{2} \right] \\ 0 \end{bmatrix} \quad (2.14)$$

By dropping the state dependence, the non-linear differential equations presented in Equation (2.7) become linear. The resulting expression is quite similar to that of the one found in [10]; however, there are additional terms within the damping matrix associated with the change in the effective mass through time. These additional terms in the damping matrix, as well as the time-varying effective mass term in the mass matrix result in a set linear differential equations with time-varying parameters for which the steady state response of the system cannot be obtained using traditional frequency-domain analysis techniques.

The system response could be obtained by numerically integrating the second-order differential equations with time-varying parameters, allowing sufficient time to pass such that the steady-state response is revealed. Although the detail of a time-domain response can be useful, it must be post-processed to extract motion amplitude, phase, net and gross power values, and it is not ideal for the purposes of

optimization. Consequently, a closed form frequency-domain solution is desired that will remove any ambiguity in the response of the WEC to a regular wave input and a periodic variation of the effective mass.

2.2 Added Mass, Hydrodynamics and Radiation

A constant coefficient added mass and damping model has been adopted for the purposes of this study. The body mass present in Equation (2.11) contains both the physical mass and estimated added mass terms of the bodies at their respective natural frequencies, Equations (2.15) and (2.16). The third body, the reaction mass, is not in contact with the fluid surrounding the spar and, as a result, there are no added mass or damping terms associated with it.

$$m_1 \simeq m_f + m_{a,f}(\omega_{n,f}) \quad (2.15)$$

$$m_2 \simeq m_s + m_{a,s}(\omega_{n,s}) \quad (2.16)$$

The damping coefficients c_1 and c_2 of Equation (2.12) are also a lumped coefficient containing both the viscous drag coefficient, $c_{v,j}$, and the radiation damping coefficient, b_j , for body j .

$$c_1 \simeq c_{v,f} + b_f(\omega_{n,f}) \quad (2.17)$$

$$c_2 \simeq c_{v,s} + b_s(\omega_{n,s}) \quad (2.18)$$

Referring to Section 1.3.2, the added mass and damping hydrodynamic coefficients will exhibit frequency dependence, and to be evaluated correctly a wet oscillator model should be used. Currently, the frequency dependence of each of the above terms are being investigated for the SyncWave device using WAMIT; a computer program to assess the motion and load felt by an offshore structure subject to waves. While the frequency dependence of these values is not included in this work, the solution method being developed is formulated in terms of the complete mass and damping matrices given in Equation (2.11)-(2.12). As such, the method will place no restrictions on the m_{ij} and c_{ij} values, and updated frequency dependent coefficients can be applied

directly in the evaluation process presented at the time they are available.

2.3 Intrinsic Periodically Varying Control Actions

In order for the time-variant effective mass to be analyzed within the frequency-domain, its variation must be periodic. This is a logical requirement, as the proper control adjustments should be periodic for a device subject to regular wave forcing. Beyond this requirement, it is unclear as to what specific effective mass motion will produce improved power conversion. It is suggested here that the effective mass variation, $m_4(t)$, should be represented as a Fourier series. The Fourier series representation provides a suitable compromise between simplicity and flexibility: this mathematical form expands the range of control parameter wave forms that can be considered while limiting the definition of $m_4(t)$ to a finite parameter set. To consider a periodic $m_4(t)$ within an optimization, the various amplitudes, ϵ , and phase values, ϕ , of the different levels of the Fourier series, as well as, the fundamental control frequency variation, ω_c , become additional design variables in a system optimization:

$$m_4(t) = \epsilon_0 + \epsilon_1 \cos(\omega_c t + \phi_1) + \epsilon_2 \cos(2\omega_c t + \phi_2) + \epsilon_3 \cos(3\omega_c t + \phi_3) + \dots \quad (2.19)$$

For the purpose of methodology development, a truncated form of Equation (2.19) is sufficient and appropriate. As such, the first two levels of the Fourier series are examined. That is, the effective mass variation will be governed by a sinusoid with amplitude ϵ_1 , phase ϕ_1 , control frequency ω_c , and a bias ϵ_0 :

$$\begin{aligned} m_4(t) &= \epsilon_0 + \epsilon_1 \cos(\omega_c t + \phi_1) \\ &= \epsilon_0 + \epsilon_1 \left[\frac{e^{i(\omega_c t + \phi_1)} + e^{-i(\omega_c t + \phi_1)}}{2} \right] \end{aligned} \quad (2.20)$$

This simplifies the process of methodology development while providing a basis for a further extension of the method to build a Fourier series to describe the change in effective mass through time. In Appendix A, the process of extending the two-term Fourier series to a three-term Fourier series is examined.

Here, m_4 is strictly real and can be represented by a phase shifted cosine term. To simplify the derivation, complex notation of the cosine term is used. Substituting the form of effective mass variation into the mass and damping matrices results in the following expressions:

$$\begin{aligned}
\mathbf{M} &= \begin{bmatrix} m_1 & 0 & 0 \\ 0 & \epsilon_0 + m_2 & -\epsilon_0 \\ 0 & -\epsilon_0 & \epsilon_0 + m_3 \end{bmatrix} \\
&+ \frac{\epsilon_1}{2} \left\{ \begin{bmatrix} 0 & 0 & 0 \\ 0 & 1 & -1 \\ 0 & -1 & 1 \end{bmatrix} e^{i(\omega_c t + \phi_1)} + \begin{bmatrix} 0 & 0 & 0 \\ 0 & 1 & -1 \\ 0 & -1 & 1 \end{bmatrix} e^{-i(\omega_c t + \phi_1)} \right\} \\
&= \mathbf{M}_L + \frac{\epsilon_1}{2} \mathbf{Q} [e^{i(\omega_c t + \phi_1)} + e^{-i(\omega_c t + \phi_1)}] \tag{2.21}
\end{aligned}$$

$$\begin{aligned}
\mathbf{C} &= \begin{bmatrix} c_1 + c_g & -c_g & 0 \\ -c_g & c_2 + c_g + c_3 & -c_3 \\ 0 & -c_3 & c_3 \end{bmatrix} \\
&+ i\omega_c \frac{\epsilon_1}{2} \left\{ \begin{bmatrix} 0 & 0 & 0 \\ 0 & 1 & -1 \\ 0 & -1 & 1 \end{bmatrix} e^{i(\omega_c t + \phi_1)} - \begin{bmatrix} 0 & 0 & 0 \\ 0 & 1 & -1 \\ 0 & -1 & 1 \end{bmatrix} e^{-i(\omega_c t + \phi_1)} \right\} \\
&= \mathbf{C}_L + i\omega_c \frac{\epsilon_1}{2} \mathbf{Q} [e^{i(\omega_c t + \phi_1)} - e^{-i(\omega_c t + \phi_1)}] \tag{2.22}
\end{aligned}$$

$$\begin{aligned}
\mathbf{K} &= \begin{bmatrix} k_1 & 0 & 0 \\ 0 & k_2 + k_3 & -k_3 \\ 0 & -k_3 & k_3 \end{bmatrix} \\
&= \mathbf{K}_L \tag{2.23}
\end{aligned}$$

Where

$$\mathbf{Q} = \begin{bmatrix} 0 & 0 & 0 \\ 0 & 1 & -1 \\ 0 & -1 & 1 \end{bmatrix} \tag{2.24}$$

The subscript ‘L’ indicates the portion of the overall system matrix that would present if the control technique under consideration were linear (i.e. $\epsilon_1 = 0$ and

$\epsilon_0 \neq 0$) and, as a result, are the the same mass, damping, and stiffness matrices found in [16].

2.4 Steady State Solution

Over the past few decades there has been enormous growth in computational power and, as a result, the solution of ordinary differential equations has been drastically accelerated. Consequently, the use of asymptotic approximation methods has dropped dramatically in favour iterative numerical methods; however, for this particular problem an asymptotic approximation is of particular interest as it allows for a closed form representation of the device response.

Perturbation analysis is one example of asymptotic approximation and is widely used in the physical sciences [33]. Perturbation analysis, as described in [32] and [34], allows for an approximate solution to the non-linear vibration problem by assessing the solution to a closely related linear problem and augmenting it with a power series based on a suitable perturbation parameter. The perturbation parameter quantifies the deviation from the linear portion of the problem. The perturbation parameter chosen for this analysis is the amplitude of the effective mass variation, ϵ_1 , of Equation (2.20).

2.4.1 Governing Equations

In the solution of Equation (2.9), $\underline{z}(t)$, is assumed to be in the form of a perturbation parameter power series with the leading term in the series being the solution to the original linear problem and each subsequent term to be a contribution to the deviation from the linear problem:

$$\underline{z}(t) = \underline{z}_0(t) + \epsilon_1^1 \underline{z}_1(t) + \epsilon_1^2 \underline{z}_2(t) + \dots \quad (2.25)$$

Where each of the solution levels, $\underline{z}_n(t)$, have units of $[\text{kg}^{-n}\text{m}]$.

In traditional perturbation analysis, the perturbation parameter is required to be small (i.e. $\epsilon_1 < 1$). This ensures that the assumed form of the solution is bounded and thus can converge on a viable solution. The perturbation parameter used in the evaluation of the SyncWave device is a control design variable and can take on

solved as a linear system subject to steady forced vibration. The expressions of Equation (2.27) must be solved sequentially, as the forcing term of any level requires the solution of the preceding level. For cases where there are two or more forcing terms with distinct frequencies, superposition can be applied. If a wet oscillator model were to be used, the frequency dependent mass and damping coefficients would be included within their respective matrices on the left-hand side of Equation (2.27) in the \mathbf{M}_L and \mathbf{C}_L matrices for each of the superimposed oscillator equations.

The forcing for the zeroth order expression, ϵ_1^0 , has been represented as a cosine term in phasor form, this ensures that the solution to the expression is strictly real. Traditionally in frequency-domain analysis, the imaginary portion of the solution is allowed to remain and is simply ignored; however, doing so in this scenario will result in complex artifacts occurring on the forcing side on the succeeding expression. These complex artifacts will combine with the complex term in the control wave form, the ω_c dependence in Equation (2.27), to create incorrect real valued contributions to $\underline{z}_i(t)$ which then propagate throughout the successive levels of the solution response.

At this stage, it is unknown how many terms in the power series of Equation (2.25) will be required to converge on the solution. In the following section, a programmable calculation loop is presented that can be executed to a desired level of the solutions. To demonstrate the calculation pattern, the process of deriving the solution to the first three terms of the solution is presented below in Section 2.4.2, and a closed form expression for any arbitrary level in the solution will be given.

2.4.2 Recursive Procedure

Here, the terminology used in the discussion of the solution process is defined. “The solution” will refer to the complete motion response of the WEC’s three bodies, $\underline{z}(t)$. The solution is found by summing the power series terms found on the right-hand side of Equation (2.25). Because each of the terms in the power series must be evaluated sequentially, it is useful to think of each term in the solution as a “level”. As will be seen, each level may contain more than one “component”—resulting from the superposition of forcing terms with different frequencies in each level’s second order ordinary differential equation, shown in Equation (2.27). Figure 2.2 illustrates

the terminology that will be used.

The Solution

$$\underline{z}(t) = \underline{z}_0(t) + \epsilon_1^1 \underline{z}_1(t) + \epsilon_1^2 \underline{z}_2(t) + \cdots + \epsilon_1^n \underline{z}_n(t) + \cdots$$

n^{th} Level

$$\epsilon_1^n : \underline{z}_n(t) = \underline{z}_n^{(1)}(t) + \underline{z}_n^{(2)}(t) + \cdots + \underline{z}_n^{(j)}(t) + \cdots$$

j^{th} Component

$$\underline{z}_n^{(j)}(t) = |\zeta_n^{(j)}| \left[e^{i(\omega_n^{(j)}t + \theta_n^{(j)})} + e^{-i(\omega_n^{(j)}t + \theta_n^{(j)})} \right]$$

Component's Complex Amplitude

Component's Frequency

Component's Phase

Figure 2.2: Clarification of the terminology used throughout this work.

Zeroth Level: The zeroth level expression is associated with the group of variables in Equation (2.27) that do not contain the perturbation parameter:

$$\epsilon_1^0 : \mathbf{M}_L \ddot{\mathbf{z}}_0 + \mathbf{C}_L \dot{\mathbf{z}}_0 + \mathbf{K}_{\mathbf{z}_0} = |\vec{\mathbf{f}}_e| \frac{1}{2} \left[e^{i\omega_i t + \theta_e} + e^{-i\omega_i t - \theta_e} \right] \quad (2.28)$$

The zeroth level of the solution is unique; it is the only level that depends entirely on incident wave forcing frequency and contains no information from any subsequent or proceeding level of the solution. The zeroth level's expression contains two forcing terms, built from a complex conjugate pair in the square brackets on the right-hand side of Equation (2.28). Applying superposition, two ordinary differential equations are produced.

$$\mathbf{M}_L \ddot{\mathbf{z}}_0^{(1)}(t) + \mathbf{C}_L \dot{\mathbf{z}}_0^{(1)}(t) + \mathbf{K}_{\mathbf{z}_0} \mathbf{z}_0^{(1)}(t) = |\vec{\mathbf{f}}_e| \frac{1}{2} e^{i(\omega_i t + \theta_e)} \quad (2.29)$$

$$\mathbf{M}_L \ddot{\mathbf{z}}_0^{(2)}(t) + \mathbf{C}_L \dot{\mathbf{z}}_0^{(2)}(t) + \mathbf{K}_{\mathbf{z}_0} \mathbf{z}_0^{(2)}(t) = |\vec{\mathbf{f}}_e| \frac{1}{2} e^{-i(\omega_i t + \theta_e)} \quad (2.30)$$

$$\mathbf{z}_0(t) = \mathbf{z}_0^{(1)}(t) + \mathbf{z}_0^{(2)}(t) \quad (2.31)$$

Where the superscripts (1) and (2) identify the components of the zeroth level's contribution to the overall WEC response to the wave excitation. Each of these components can then be solved using traditional frequency-domain analysis, by assuming the device will reach a steady-state oscillation equivalent to that of the forcing frequency, the device's acceleration, velocity, and position can be represented as follows:

$$-\omega_i^2 \mathbf{M}_L \zeta_0^{(1)}(t) + i\omega_i \mathbf{C}_L \zeta_0^{(1)}(t) + \mathbf{K}_{\zeta_0} \zeta_0^{(1)}(t) = |\vec{\mathbf{f}}_e| \frac{1}{2} e^{i\theta_e} \quad (2.32)$$

$$-\omega_i^2 \mathbf{M}_L \zeta_0^{(2)}(t) - i\omega_i \mathbf{C}_L \zeta_0^{(2)}(t) + \mathbf{K}_{\zeta_0} \zeta_0^{(2)}(t) = |\vec{\mathbf{f}}_e| \frac{1}{2} e^{-i\theta_e} \quad (2.33)$$

Solving for each component's complex amplitude of oscillation, $\vec{\zeta}_0$:

$$\vec{\zeta}_0^{(1)} = [-\omega_i^2 \mathbf{M}_L + i\omega_i \mathbf{C}_L + \mathbf{K}]^{-1} \left[|\vec{\mathbf{f}}_e| \frac{1}{2} e^{i\theta_e} \right] \quad (2.34)$$

$$\vec{\zeta}_0^{(2)} = [-\omega_i^2 \mathbf{M}_L - i\omega_i \mathbf{C}_L + \mathbf{K}]^{-1} \left[|\vec{\mathbf{f}}_e| \frac{1}{2} e^{-i\theta_e} \right] \quad (2.35)$$

Both amplitude and phase information for each body of the WEC: the spar, float, and reaction mass are contained in $\vec{\zeta}_0$. To express the device's motion as a function of time, these complex amplitudes are then multiplied by their corresponding oscillation

wave form.

$$\underline{z}^{(1)}(t) = \bar{\zeta}_0^{(1)} e^{i\omega_i t} \quad (2.36)$$

$$\underline{z}^{(2)}(t) = \bar{\zeta}_0^{(2)} e^{-i\omega_i t} \quad (2.37)$$

Both components are phasors rotating in the complex plane at the same frequency and magnitude, but with different directions of rotation. It can be shown that:

$$\bar{\zeta}_0^{(2)} = \bar{\zeta}_0^{*(1)} \quad (2.38)$$

and thus:

$$\underline{z}_0^{(2)} = \bar{\zeta}_0^{*(1)} e^{-i\omega_i t} \quad (2.39)$$

Splitting each of the complex amplitudes into their respective real and imaginary portions and expanding each of the components into their respective sine and cosine terms results in some cancellation, providing a simplification that can be made to reduce the number terms used to assemble $\underline{z}_0(t)$.

$$\zeta_{0R}^{(1)} = \Re \left\{ \bar{\zeta}_0^{(1)} \right\} \quad \zeta_{0I}^{(1)} = \Im \left\{ \bar{\zeta}_0^{(1)} \right\} \quad (2.40)$$

$$\underline{z}_0(t) = \left(\zeta_{0R}^{(1)} + i\zeta_{0I}^{(1)} \right) (\cos(\omega_i t) + i \sin(\omega_i t)) + \left(\zeta_{0R}^{(1)} - i\zeta_{0I}^{(1)} \right) (\cos(\omega_i t) - i \sin(\omega_i t)) \quad (2.41)$$

$$\underline{z}_0(t) = \left(2\zeta_{0R}^{(1)} \cos(\omega_i t) - 2\zeta_{0I}^{(1)} \sin(\omega_i t) \right) \quad (2.42)$$

Which is equivalent to:

$$\underline{z}_0(t) = \Re \left\{ \left(2\zeta_{0R}^{(1)} + i2\zeta_{0I}^{(1)} \right) (\cos(\omega_i t) + i \sin(\omega_i t)) \right\} \quad (2.43)$$

$$\underline{z}_0(t) = \Re \left\{ \left(2\zeta_{0R}^{(1)} + i2\zeta_{0I}^{(1)} \right) e^{i\omega_i t} \right\} \quad (2.44)$$

$$\underline{z}_0(t) = \Re \left\{ 2\bar{\zeta}_0^{(1)} e^{i\omega_i t} \right\} \quad (2.45)$$

Finally, the summation of the zeroth level's two components can be represented by a

single amplitude multiplied by a cosine term represented in complex notation:

$$\underline{z}_0 = 2|\underline{\zeta}_0^{(1)}| \left[\frac{e^{i(\omega t + \underline{\theta}_0^{(1)})} + e^{-i(\omega t + \underline{\theta}_0^{(1)})}}{2} \right] \quad (2.46)$$

Where

$$\underline{\theta}_0^{(1)} = \text{atan2} \left(\frac{\underline{\zeta}_{0I}^{(1)}}{\underline{\zeta}_{0R}^{(1)}} \right) \quad (2.47)$$

As a result, the zeroth level solution, $\underline{z}_0(t)$, can be written using only the output of Equation (2.34). This saves computational time and also simplifies the forcing input to the next level of the solution. As a result, the second component of the zeroth level will be ignored from this point forward. The complex conjugate simplification shown above is valid for any second order ordinary differential equation in which the forcing term contains a complex conjugate pair. As will be seen, the number of components in each level's solution grows at an exponential rate, and the introduction of this simplification drastically reduces the number of expressions that must be evaluated.

First Level: Substituting the result of the zeroth level expression, Equation (2.46), back into the first level expression found in Equation (2.27) results in the following:

$$\begin{aligned} \mathbf{M}_{\underline{L}}\ddot{\underline{z}}_1 + \mathbf{C}_{\underline{L}}\dot{\underline{z}}_1 + \mathbf{K}_{\underline{L}}\underline{z}_1 &= \frac{\mathbf{Q}}{2}\omega^2 [e^{i(\omega_c t + \phi_1)} + e^{-i(\omega_c t + \phi_1)}] |\underline{\zeta}_0^{(1)}| \left(e^{i(\omega t + \underline{\theta}_0)} + e^{-i(\omega t + \underline{\theta}_0)} \right) \\ &+ \frac{\mathbf{Q}}{2}\omega\omega_c [e^{i(\omega_c t + \phi_1)} - e^{-i(\omega_c t + \phi_1)}] |\underline{\zeta}_0^{(1)}| \left(e^{i(\omega t + \underline{\theta}_0)} - e^{-i(\omega t + \underline{\theta}_0)} \right) \end{aligned} \quad (2.48)$$

Organizing the forcing terms into complex conjugate pairs so that the complex conjugate simplification seen in Equation (2.46) can be exploited:

$$\begin{aligned} \mathbf{M}_{\underline{L}}\ddot{\underline{z}}_1 + \mathbf{C}_{\underline{L}}\dot{\underline{z}}_1 + \mathbf{K}_{\underline{L}}\underline{z}_1 &= \frac{\mathbf{Q}}{2}(\omega^2 + \omega\omega_c) |\underline{\zeta}_0^{(1)}| \left[e^{i((\omega + \omega_c)t + \underline{\theta}_0 + \phi_1)} + e^{-i((\omega + \omega_c)t + \underline{\theta}_0 + \phi_1)} \right] \\ &+ \frac{\mathbf{Q}}{2}(\omega^2 - \omega\omega_c) |\underline{\zeta}_0^{(1)}| \left[e^{i((\omega - \omega_c)t + \underline{\theta}_0 - \phi_1)} + e^{-i((\omega - \omega_c)t + \underline{\theta}_0 - \phi_1)} \right] \end{aligned} \quad (2.49)$$

Even with the complex conjugate simplification, two forcing terms must be considered

on the right-hand side of Equation (2.49), requiring the use of superposition:

$$-(\omega + \omega_c)^2 \vec{\zeta}_1^{(1)} \mathbf{M}_L + i(\omega + \omega_c) \vec{\zeta}_1^{(1)} \mathbf{C}_L + \mathbf{K} \vec{\zeta}_1^{(1)} = \frac{\mathbf{Q}}{2} (\omega^2 + \omega \omega_c) |\vec{\zeta}_0| e^{i(\underline{\theta}_0 + \phi_1)} \quad (2.50)$$

$$-(\omega - \omega_c)^2 \vec{\zeta}_1^{(2)} \mathbf{M}_L + i(\omega - \omega_c) \vec{\zeta}_1^{(2)} \mathbf{C}_L + \mathbf{K} \vec{\zeta}_1^{(2)} = \frac{\mathbf{Q}}{2} (\omega^2 - \omega \omega_c) |\vec{\zeta}_0| e^{i(\underline{\theta}_0 - \phi_1)} \quad (2.51)$$

$$\vec{\zeta}_1^{(1)} = [-(\omega + \omega_c)^2 \mathbf{M}_L + i(\omega + \omega_c) \mathbf{C}_L + \mathbf{K}]^{-1} \frac{\mathbf{Q}}{2} (\omega^2 + \omega \omega_c) |\vec{\zeta}_0| e^{i(\underline{\theta}_0 + \phi_1)} \quad (2.52)$$

$$\vec{\zeta}_1^{(2)} = [-(\omega - \omega_c)^2 \mathbf{M}_L + i(\omega - \omega_c) \mathbf{C}_L + \mathbf{K}]^{-1} \frac{\mathbf{Q}}{2} (\omega^2 - \omega \omega_c) |\vec{\zeta}_0| e^{i(\underline{\theta}_0 - \phi_1)} \quad (2.53)$$

The first level's solution is then given by the summation of the following two components:

$$z_1(t) = |\vec{\zeta}_1^{(1)}| \left[e^{i((\omega + \omega_c)t + \underline{\theta}_1^{(1)})} + e^{-i((\omega + \omega_c)t + \underline{\theta}_1^{(1)})} \right] + |\vec{\zeta}_1^{(2)}| \left[e^{i((\omega - \omega_c)t + \underline{\theta}_1^{(2)})} + e^{-i((\omega - \omega_c)t + \underline{\theta}_1^{(2)})} \right] \quad (2.54)$$

Where

$$\underline{\theta}_1^{(1)} = \text{atan2} \left(\frac{\zeta_{1I}^{(1)}}{\zeta_{1R}^{(1)}} \right) \quad \underline{\theta}_1^{(2)} = \text{atan2} \left(\frac{\zeta_{1I}^{(2)}}{\zeta_{1R}^{(2)}} \right) \quad (2.55)$$

Second Level: The evaluation of the second level expression is quite similar to that of the the first level problem. It will be the last level shown for the purposes of development of a solution pattern.

Substituting the result of the first level's expression, Equation (2.54), back into the second-order expression found in Equation (2.27) results in the following expression:

$$\begin{aligned} \mathbf{M}_L \ddot{z}_2 + \mathbf{C}_L \dot{z}_2 + \mathbf{K} z_2 &= \frac{\mathbf{Q}}{2} (\omega + \omega_c)^2 [e^{i(\omega_c t + \phi_1)} + e^{-i(\omega_c t + \phi_1)}] |\vec{\zeta}_1^{(1)}| \left(e^{i((\omega + \omega_c)t + \underline{\theta}_1^{(1)})} + e^{-i((\omega + \omega_c)t + \underline{\theta}_1^{(1)})} \right) \\ &+ \frac{\mathbf{Q}}{2} (\omega + \omega_c) \omega_c [e^{i(\omega_c t + \phi_1)} - e^{-i(\omega_c t + \phi_1)}] |\vec{\zeta}_1^{(1)}| \left(e^{i((\omega + \omega_c)t + \underline{\theta}_1^{(1)})} - e^{-i((\omega + \omega_c)t + \underline{\theta}_1^{(1)})} \right) \\ &+ \frac{\mathbf{Q}}{2} (\omega - \omega_c)^2 [e^{i(\omega_c t + \phi_1)} + e^{-i(\omega_c t + \phi_1)}] |\vec{\zeta}_1^{(2)}| \left(e^{i((\omega - \omega_c)t + \underline{\theta}_1^{(2)})} + e^{-i((\omega - \omega_c)t + \underline{\theta}_1^{(2)})} \right) \\ &+ \frac{\mathbf{Q}}{2} (\omega - \omega_c) \omega_c [e^{i(\omega_c t + \phi_1)} - e^{-i(\omega_c t + \phi_1)}] |\vec{\zeta}_1^{(2)}| \left(e^{i((\omega - \omega_c)t + \underline{\theta}_1^{(2)})} - e^{-i((\omega - \omega_c)t + \underline{\theta}_1^{(2)})} \right) \end{aligned} \quad (2.56)$$

Organizing the forcing terms into complex conjugate pairs so that the complex con-

jugate simplification seen in Equation (2.46) can be exploited:

$$\begin{aligned}
\mathbf{M}_L \ddot{\underline{z}}_2 + \mathbf{C}_L \dot{\underline{z}}_2 + \mathbf{K} \underline{z}_2 &= \frac{\mathbf{Q}}{2} ((\omega + \omega_c)^2 + (\omega + \omega_c)\omega_c) |\bar{\zeta}_1^{(1)}| \left[e^{i((\omega+2\omega_c)t + \underline{\theta}_1^{(1)} + \phi_1)} + e^{-i((\omega+2\omega_c)t + \underline{\theta}_1^{(1)} + \phi_1)} \right] \\
&+ \frac{\mathbf{Q}}{2} ((\omega + \omega_c)^2 - (\omega + \omega_c)\omega_c) |\bar{\zeta}_1^{(1)}| \left[e^{i(\omega t + \underline{\theta}_1^{(1)} - \phi_1)} + e^{-i(\omega t + \underline{\theta}_1^{(1)} - \phi_1)} \right] \\
&+ \frac{\mathbf{Q}}{2} ((\omega - \omega_c)^2 + (\omega - \omega_c)\omega_c) |\bar{\zeta}_1^{(2)}| \left[e^{i(\omega t + \underline{\theta}_1^{(2)} + \phi_1)} + e^{-i(\omega t + \underline{\theta}_1^{(2)} + \phi_1)} \right] \\
&+ \frac{\mathbf{Q}}{2} ((\omega - \omega_c)^2 - (\omega - \omega_c)\omega_c) |\bar{\zeta}_1^{(2)}| \left[e^{i((\omega-2\omega_c)t + \underline{\theta}_1^{(2)} - \phi_1)} + e^{-i((\omega-2\omega_c)t + \underline{\theta}_1^{(2)} - \phi_1)} \right]
\end{aligned} \tag{2.57}$$

Similarly to the zeroth and first level calculations, the complex conjugate simplification is applied to the paired forcing functions of Equation (2.57). In this expression there are four paired forcing functions that must be considered and thus superposition is again exploited.

$$\begin{aligned}
-(\omega + 2\omega_c)^2 \bar{\zeta}_2^{(1)} \mathbf{M}_L + i(\omega + 2\omega_c) \bar{\zeta}_2^{(1)} \mathbf{C}_L + \mathbf{K} \bar{\zeta}_2^{(1)} &= \frac{\mathbf{Q}}{2} ((\omega + \omega_c)^2 + (\omega + \omega_c)\omega_c) |\bar{\zeta}_1^{(1)}| e^{i(\underline{\theta}_1^{(1)} + \phi_1)} \\
-\omega^2 \bar{\zeta}_2^{(2)} \mathbf{M}_L + i\omega \bar{\zeta}_2^{(2)} \mathbf{C}_L + \mathbf{K} \bar{\zeta}_2^{(2)} &= \frac{\mathbf{Q}}{2} ((\omega + \omega_c)^2 - (\omega + \omega_c)\omega_c) |\bar{\zeta}_1^{(1)}| e^{i(\underline{\theta}_1^{(1)} - \phi_1)} \\
-\omega^2 \bar{\zeta}_2^{(3)} \mathbf{M}_L + i\omega \bar{\zeta}_2^{(3)} \mathbf{C}_L + \mathbf{K} \bar{\zeta}_2^{(3)} &= \frac{\mathbf{Q}}{2} ((\omega - \omega_c)^2 + (\omega - \omega_c)\omega_c) |\bar{\zeta}_1^{(2)}| e^{i(\underline{\theta}_1^{(2)} + \phi_1)} \\
-(\omega - 2\omega_c)^2 \bar{\zeta}_2^{(4)} \mathbf{M}_L + i(\omega - 2\omega_c) \bar{\zeta}_2^{(4)} \mathbf{C}_L + \mathbf{K} \bar{\zeta}_2^{(4)} &= \frac{\mathbf{Q}}{2} ((\omega - \omega_c)^2 - (\omega - \omega_c)\omega_c) |\bar{\zeta}_1^{(2)}| e^{i(\underline{\theta}_1^{(2)} - \phi_1)}
\end{aligned} \tag{2.58}$$

Solving for each component's complex amplitude of oscillation:

$$\bar{\zeta}_2^{(1)} = [-(\omega + 2\omega_c)^2 \mathbf{M}_L + i(\omega + 2\omega_c) \mathbf{C}_L + \mathbf{K}]^{-1} \frac{\mathbf{Q}}{2} ((\omega + \omega_c)^2 + (\omega + \omega_c)\omega_c) |\bar{\zeta}_1^{(1)}| e^{i(\underline{\theta}_1^{(1)} + \phi_1)} \tag{2.59}$$

$$\bar{\zeta}_2^{(2)} = [-\omega^2 \mathbf{M}_L + i\omega \mathbf{C}_L + \mathbf{K}]^{-1} \frac{\mathbf{Q}}{2} ((\omega + \omega_c)^2 - (\omega + \omega_c)\omega_c) |\bar{\zeta}_1^{(1)}| e^{i(\underline{\theta}_1^{(1)} - \phi_1)} \tag{2.60}$$

$$\bar{\zeta}_2^{(3)} = [-\omega^2 \mathbf{M}_L + i\omega \mathbf{C}_L + \mathbf{K}]^{-1} \frac{\mathbf{Q}}{2} ((\omega - \omega_c)^2 + (\omega - \omega_c)\omega_c) |\bar{\zeta}_1^{(2)}| e^{i(\underline{\theta}_1^{(2)} + \phi_1)} \tag{2.61}$$

$$\bar{\zeta}_2^{(4)} = [-(\omega - 2\omega_c)^2 \mathbf{M}_L + i(\omega - 2\omega_c) \mathbf{C}_L + \mathbf{K}]^{-1} \frac{\mathbf{Q}}{2} ((\omega - \omega_c)^2 - (\omega - \omega_c)\omega_c) |\bar{\zeta}_1^{(2)}| e^{i(\underline{\theta}_1^{(2)} - \phi_1)} \tag{2.62}$$

The second level response is then given by the summation of the four component's complex amplitudes multiplied by their respective phase shifted waveforms:

$$\begin{aligned}
\underline{z}_2(t) &= |\bar{\zeta}_2^{(1)}| \left(e^{i((\omega+2\omega_c)t + \underline{\theta}_2^{(1)})} + e^{-i((\omega+2\omega_c)t + \underline{\theta}_2^{(1)})} \right) + |\bar{\zeta}_2^{(2)}| \left(e^{i(\omega t + \underline{\theta}_2^{(2)})} + e^{-i(\omega t + \underline{\theta}_2^{(2)})} \right) \\
&+ |\bar{\zeta}_2^{(3)}| \left(e^{i(\omega t + \underline{\theta}_2^{(3)})} + e^{-i(\omega t + \underline{\theta}_2^{(3)})} \right) + |\bar{\zeta}_2^{(4)}| \left(e^{i((\omega-2\omega_c)t + \underline{\theta}_2^{(4)})} + e^{-i((\omega-2\omega_c)t + \underline{\theta}_2^{(4)})} \right)
\end{aligned} \tag{2.63}$$

nth Level: The solution to the each level becomes progressively more involved. However, within the three levels presented, some patterns begin to emerge that can be used to automate the process. First, it is noted that at any arbitrary level, the forcing function that is constructed on the preceding level's solution will produce two motion components on the next successive level. As such, the number of portions to a solution will increase exponentially as the number of levels increase as:

$$\underline{z}_n = \underline{z}_n^{(1)} + \underline{z}_n^{(2)} + \cdots + \underline{z}_n^{(M)}; \quad M = 2^n \quad (2.64)$$

Next, a relationship between the frequency of oscillation of the solution component and the frequency of oscillation of the previous levels solution can be programmed. As stated above, the frequency of oscillation of a preceding level's solution component, $\omega_{n-1}^{(j)}$, is responsible for producing two solution components on the next successive level, resulting in two oscillation frequencies $\omega_n^{(2j-1)}$ and $\omega_n^{(2j)}$. These successive oscillation frequencies must follow:

$$\omega_n^{(2j-1)} = \omega_{n-1}^{(j)} + \omega_c \quad (2.65)$$

$$\omega_n^{(2j)} = \omega_{n-1}^{(j)} - \omega_c \quad (2.66)$$

Where j is the component number on the previous level, $n - 1$, and could be any integer value within the following range:

$$1 \leq j \leq 2^{n-1} \quad (2.67)$$

Finally, over the first three levels of the solution, a pattern has emerged for how the preceding level components's frequencies of oscillation $\omega_{n-1}^{(j)}$ and phase $\theta_{n-1}^{(j)}$ present in the n^{th} level. As stated above, each component of the preceding level is responsible for the construction of two components on the next successive level. However, the pattern for each of the newly constructed components is different. The frequency coefficients in front of the forcing function and the phase of the forcing function differ by a sign for each component. This pattern has been described in Figure 2.3 and shown in expression is given for the first and $j^{n\text{-th}}$ components for an arbitrary level n below:

$$\begin{aligned}
 \mathbf{M}_{\mathbf{L}\ddot{\mathbf{z}}_n}^{(2j-1)} + \mathbf{C}_{\mathbf{L}\dot{\mathbf{z}}_n}^{(2j-1)} + \mathbf{K}_{\mathbf{L}\mathbf{z}_n}^{(2j-1)} &= \frac{\mathbf{Q}}{2} ((\omega_{n-1}^{(j)})^2 \oplus \omega_{n-1}^{(j)} \omega_c) |_{\zeta_{n-1}}^{(j)} \left[e^{i((\omega_{n-1}^{(j)}) \oplus \omega_c)t + \theta_{n-1}^{(j)} \phi_1} + e^{-i((\omega_{n-1}^{(j)}) \oplus \omega_c)t + \theta_{n-1}^{(j)} \phi_1} \right] \\
 \mathbf{z}_{n-1}^{(j)}(t) &= |_{\zeta_{n-1}}^{(j)} \left[e^{i(\omega_{n-1}^{(j)}t + \theta_{n-1}^{(j)})} + e^{-i(\omega_{n-1}^{(j)}t + \theta_{n-1}^{(j)})} \right] \\
 \mathbf{M}_{\mathbf{L}\ddot{\mathbf{z}}_n}^{(2j)} + \mathbf{C}_{\mathbf{L}\dot{\mathbf{z}}_n}^{(2j)} + \mathbf{K}_{\mathbf{L}\mathbf{z}_n}^{(2j)} &= \frac{\mathbf{Q}}{2} ((\omega_{n-1}^{(j)})^2 \ominus \omega_{n-1}^{(j)} \omega_c) |_{\zeta_{n-1}}^{(j)} \left[e^{i((\omega_{n-1}^{(j)}) \ominus \omega_c)t + \theta_{n-1}^{(j)} \phi_1} + e^{-i((\omega_{n-1}^{(j)}) \ominus \omega_c)t + \theta_{n-1}^{(j)} \phi_1} \right]
 \end{aligned}$$

Figure 2.3: The frequency and phase coefficients for an arbitrary level, n , are mapped from a component in the previous level's solution, $\mathbf{z}_{n-1}^{(j)}(t)$. The preceding level's component is responsible for generating two components on the n^{th} level. Note: the generated components share similar coefficient mapping, but differ by a sign.

$$\begin{aligned}
\mathbf{M}_L \ddot{\zeta}_n + \mathbf{C}_L \dot{\zeta}_n + \mathbf{K}_L \zeta_n &= \frac{\mathbf{Q}}{2} ((\omega_{n-1}^{(1)})^2 + \omega_{n-1}^{(1)} \omega_c) |\bar{\zeta}_{n-1}^{(1)}| \left[e^{i((\omega_{n-1}^{(1)} + \omega_c)t + \underline{\theta}_{n-1}^{(1)} + \phi_1)} + e^{-i((\omega_{n-1}^{(1)} + \omega_c)t + \underline{\theta}_{n-1}^{(1)} + \phi_1)} \right] \\
&+ \frac{\mathbf{Q}}{2} ((\omega_{n-1}^{(1)})^2 - \omega_{n-1}^{(1)} \omega_c) |\bar{\zeta}_{n-1}^{(1)}| \left[e^{i((\omega_{n-1}^{(1)} - \omega_c)t + \underline{\theta}_{n-1}^{(1)} - \phi_1)} + e^{-i((\omega_{n-1}^{(1)} - \omega_c)t + \underline{\theta}_{n-1}^{(1)} - \phi_1)} \right] \\
&\vdots \\
&+ \frac{\mathbf{Q}}{2} ((\omega_{n-1}^{(j_n)})^2 + \omega_{n-1}^{(j_n)} \omega_c) |\bar{\zeta}_{n-1}^{(j_n)}| \left[e^{i((\omega_{n-1}^{(j_n)} + \omega_c)t + \underline{\theta}_{n-1}^{(j_n)} + \phi_1)} + e^{-i((\omega_{n-1}^{(j_n)} + \omega_c)t + \underline{\theta}_{n-1}^{(j_n)} + \phi_1)} \right] \\
&+ \frac{\mathbf{Q}}{2} ((\omega_{n-1}^{(j_n)})^2 - \omega_{n-1}^{(j_n)} \omega_c) |\bar{\zeta}_{n-1}^{(j_n)}| \left[e^{i((\omega_{n-1}^{(j_n)} - \omega_c)t + \underline{\theta}_{n-1}^{(j_n)} - \phi_1)} + e^{-i((\omega_{n-1}^{(j_n)} - \omega_c)t + \underline{\theta}_{n-1}^{(j_n)} - \phi_1)} \right]
\end{aligned} \tag{2.68}$$

Where j_n corresponds to the last component in the previous level's solution:

$$j_n = 2^{(n-1)} \tag{2.69}$$

The patterns described in Equations (2.64)-(2.68), allow for each component's complex amplitude to be evaluated at any arbitrary level in a closed form expression as follows:

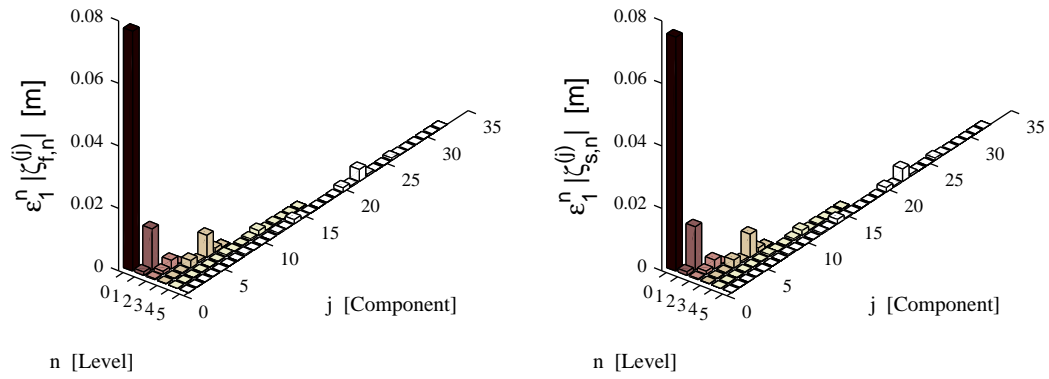
$$\begin{aligned}
\bar{\zeta}_n^{(1)} &= \left[-(\omega_{n-1}^{(1)} + \omega_c)^2 \mathbf{M}_L + i(\omega_{n-1}^{(1)} + \omega_c) \mathbf{C}_L + \mathbf{K} \right]^{-1} \frac{\mathbf{Q}}{2} ((\omega_{n-1}^{(1)})^2 + \omega_{n-1}^{(1)} \omega_c) |\bar{\zeta}_{n-1}^{(1)}| e^{i(\underline{\theta}_{n-1}^{(1)} + \phi_1)} \\
\bar{\zeta}_n^{(2)} &= \left[-(\omega_{n-1}^{(1)} - \omega_c)^2 \mathbf{M}_L + i(\omega_{n-1}^{(1)} - \omega_c) \mathbf{C}_L + \mathbf{K} \right]^{-1} \frac{\mathbf{Q}}{2} ((\omega_{n-1}^{(1)})^2 - \omega_{n-1}^{(1)} \omega_c) |\bar{\zeta}_{n-1}^{(1)}| e^{i(\underline{\theta}_{n-1}^{(1)} - \phi_1)} \\
&\vdots \\
\bar{\zeta}_n^{(2j_n-1)} &= \left[-(\omega_{n-1}^{(j_n)} + \omega_c)^2 \mathbf{M}_L + i(\omega_{n-1}^{(j_n)} + \omega_c) \mathbf{C}_L + \mathbf{K} \right]^{-1} \frac{\mathbf{Q}}{2} ((\omega_{n-1}^{(j_n)})^2 + \omega_{n-1}^{(j_n)} \omega_c) |\bar{\zeta}_{n-1}^{(j_n)}| e^{i(\underline{\theta}_{n-1}^{(j_n)} + \phi_1)} \\
\bar{\zeta}_n^{(2j_n)} &= \left[-(\omega_{n-1}^{(j_n)} - \omega_c)^2 \mathbf{M}_L + i(\omega_{n-1}^{(j_n)} - \omega_c) \mathbf{C}_L + \mathbf{K} \right]^{-1} \frac{\mathbf{Q}}{2} ((\omega_{n-1}^{(j_n)})^2 - \omega_{n-1}^{(j_n)} \omega_c) |\bar{\zeta}_{n-1}^{(j_n)}| e^{i(\underline{\theta}_{n-1}^{(j_n)} - \phi_1)} \tag{2.70}
\end{aligned}$$

The patterns have been carefully investigated and have been found to hold true for any level with the exception of the zeroth-order solution. These rules allow for a series of conditional, computational loops to be programmed such that the solution can be evaluated to any desired level. Upon each iteration level it is required that the frequency of oscillation, amplitude, and phase of each component of the solution be stored in memory, such that it can be used in succeeding level's solution. The motion

can then be represented as follows:

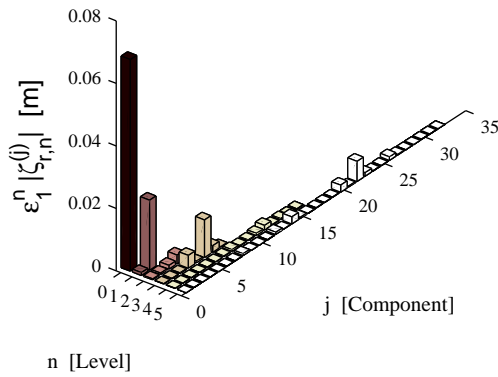
$$\begin{aligned} \underline{z}(t) = & |\underline{\zeta}_0^{(1)}| \left[e^{i(\omega_0^{(1)}t + \underline{\theta}_0^{(1)})} + e^{-i(\omega_0^{(1)}t + \underline{\theta}_0^{(1)})} \right] + \\ & \sum_{n=1}^{N_{max}} \epsilon_1^n \sum_{j=1}^{j_n} \left\{ |\underline{\zeta}_n^{(2j-1)}| \left[e^{i(\omega_n^{(2j-1)}t + \underline{\theta}_n^{(2j-1)})} + e^{-i(\omega_n^{(2j-1)}t + \underline{\theta}_n^{(2j-1)})} \right] \right. \\ & \left. + |\underline{\zeta}_n^{(2j)}| \left[e^{i(\omega_n^{(2j)}t + \underline{\theta}_n^{(2j)})} + e^{-i(\omega_n^{(2j)}t + \underline{\theta}_n^{(2j)})} \right] \right\} \end{aligned} \quad (2.71)$$

A visual representation of a solution's components, and the construction of the components into a response, can be found in Figure 2.4.2 and Figure 2.5, respectively. Physical parameters for this case are given in Table 2.1 in Section 2.5. As shown, each level's components get progressively less significant, suggesting the method will converge on a solution. A convergence analysis will be given in Section 2.5.



(a) Float

(b) Spar



(c) Reaction mass

Figure 2.4: The construction of the solution for an example case. The magnitude of each level's components are shown in relation to their position in the solution array. Physical parameters for this simulation are given in Table 2.1

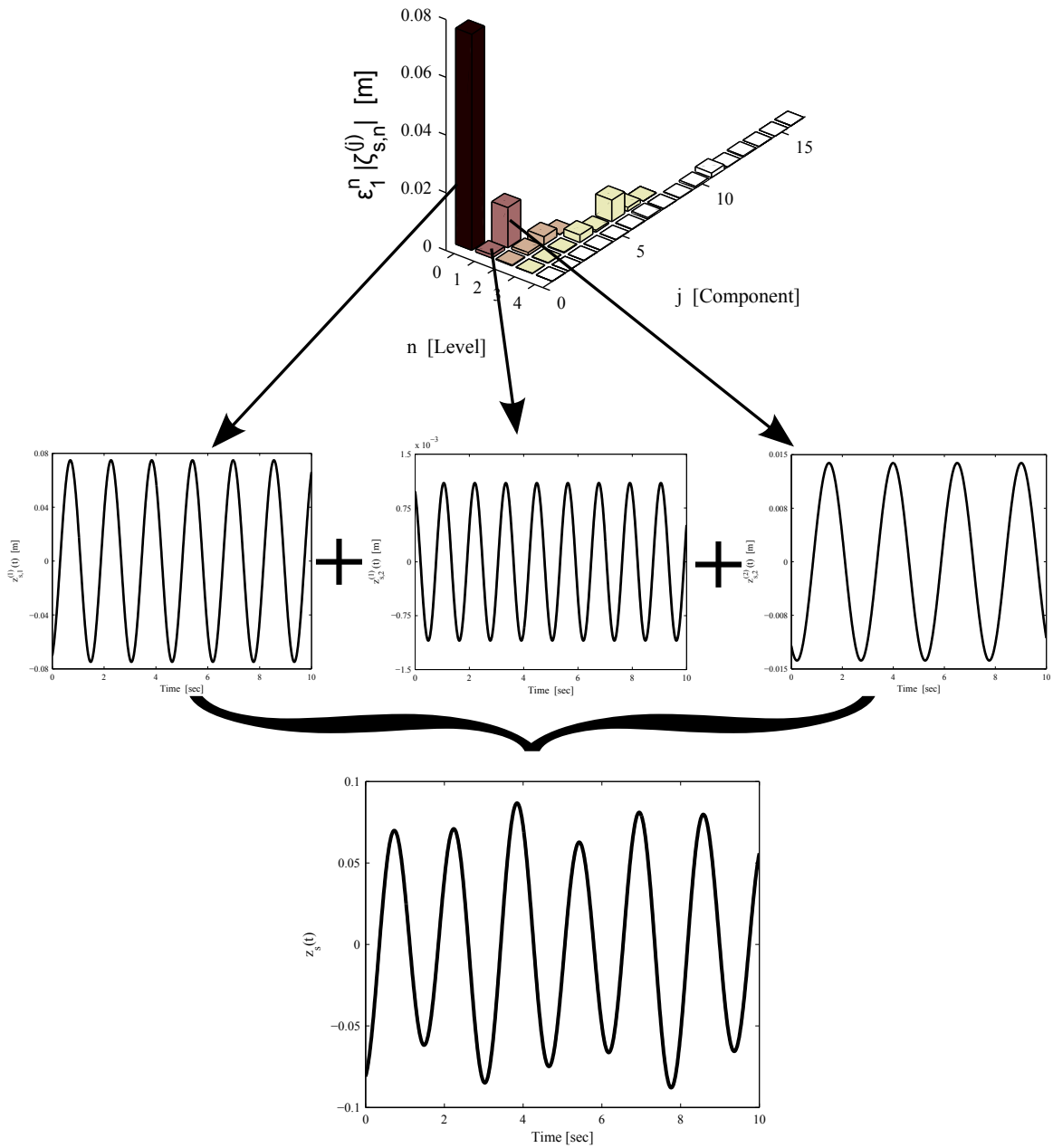


Figure 2.5: Construction of the spar response using the perturbation method.

2.5 Convergence Analysis

For the closed form perturbation method to converge on the device's motion the following criteria must be met: the rate of which each level's component amplitudes decays must be greater than the exponential growth exhibited by perturbation parameter:

$$\lim_{n \rightarrow \infty} \epsilon_1^n z_n(t) = 0 \quad (2.72)$$

If the solution does indeed converge, the next task is to determine at which level the solution can be truncated without losing any pertinent detail. To verify convergence and to determine an adequate number of levels, the perturbation method response is compared to a numerically integrated time-domain response to the motion equations of Equation (2.9).

A sample case based on the device parameters of the Froude scaled SyncWave demonstration device outlined in Section 1.3.4 is given in Table 2.1. For the purpose of consistency, the physical control parameters and wave characteristics used in the convergence analysis example will also be used throughout the remainder of this work. The regular forcing wave under consideration has a height and frequency of 0.4 meters and $1.725 \frac{\text{rad}}{\text{s}}$, respectively. This regular wave would be similar to a significant wave found in the month of November in Hesquiaht Sound, British Columbia as per Figure 1.11(b). The physical control parameters used in this demonstration case were chosen to create a significant disturbance to the linear response, so as to ensure that a significant number of levels would be required. These control parameters are a distinguishing feature of the case study and have also been tabulated below in Table 2.1.

A time-domain simulation was evaluated over an extended period of time to ensure the response had reached steady-state. This response is compared against the time-series motion response evaluated from the closed-form perturbation method approximation – found using the programmed pattern arrived at in Equations (2.70) and (2.71). To evaluate the convergence of the motion responses, there is a need for a quantitative scalar measure that depicts the difference between the two solutions at each level of the closed form perturbation method. For this purpose, the following 2-norm function is used to define the accumulation of the differences between each body's numerically integrated position and the position extracted from the closed form perturbation analysis.

Table 2.1: Wave and physical control parameters used in demonstration case.

Parameter	Name	Units	Value
H_s	Significant Wave Height	[m]	0.4
ω_i	Incident Wave Frequency	$\frac{\text{rad}}{\text{s}}$	1.725
c_g	Generator Damping	$\frac{\text{Ns}}{\text{m}}$	3000
ϵ_0	Effective Mass Bias	[kg]	10000
ϵ_1	Effective Mass Amplitude	[kg]	2000
ϕ_1	Effective Mass Phase	[rad]	0
ω_c	Effective Mass Control Frequency	$\frac{\text{rad}}{\text{s}}$	0.2

$$\Delta = \frac{\|z_{\text{time-domain}}(t) - z_{\text{perturbation}}(t)\|}{\|z_{\text{time-domain}}(t)\|} \quad 500s \leq t \leq 1000s \quad (2.73)$$

The two calculated responses were compared over the region of time where the body's motion was at a steady-state, $500s \leq t \leq 1000s$, to neglect any expected differences in the responses during the transient phase. To ensure both responses were compared at equivalent times, the time vector provided by the numerical integrator was used to synthesize a time-series of WEC motion for the results of the perturbation method. The wave forcing on the spar and float in both cases contain the same frequency and phase information and, as a result, both the time-domain and perturbation method motion responses should be in phase when the steady-state condition is achieved in the numerically integrated solution.

The results of this particular convergence test are shown in Figure 2.6. In this example, it is shown that the frequency-domain approximation converges to the time-domain motion in an exponentially decaying manner. Truncating the solution after the 30th level would appear to give an accurate motion response with minimal differences between the numerically integrated time-domain response and the response extracted from the perturbation method.

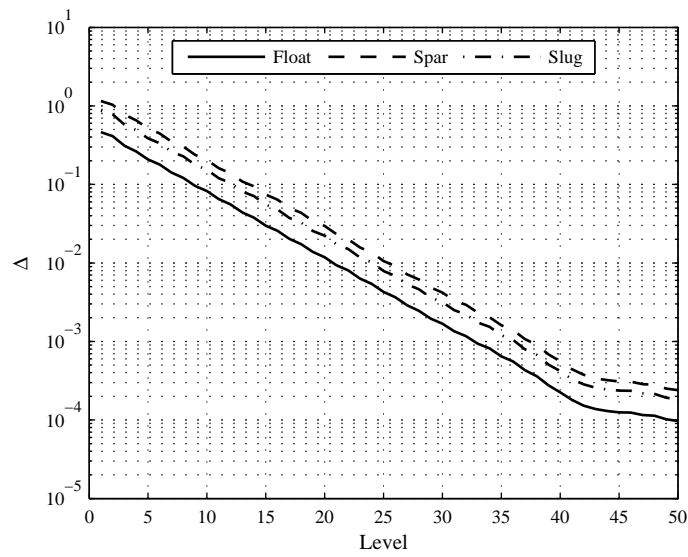
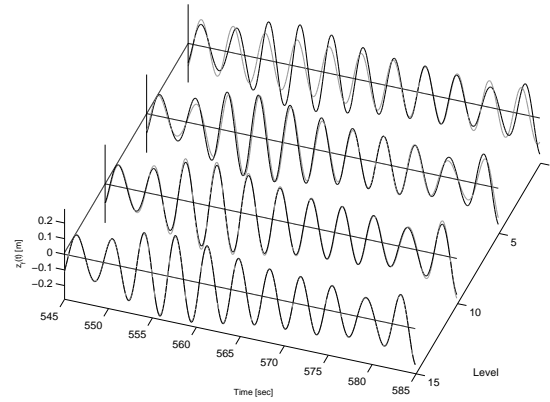
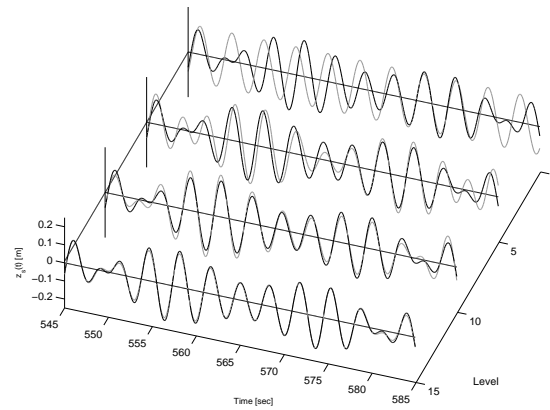


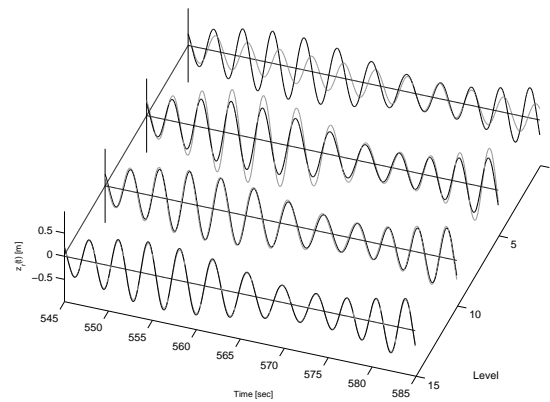
Figure 2.6: The convergence of perturbation method motion response to the time-domain simulation is measured using the norm of the difference between the two responses. $\underline{z}(t)$, $500s \leq t \leq 1000s$, was calculated using the time-domain integration approach and the perturbation approach outlined in this chapter.



(a) Float motion



(b) Spar motion



(c) Reaction mass motion

Figure 2.7: Time-series motion for each of the device's bodies are shown at different perturbation method solution levels in grey, and compared to the motion of the time-domain simulation shown in black. Physical parameters for this simulation are given in Table 2.1

As an alternative measure of convergence, the motion responses of the bodies have been visually compared in time, Figure 2.7. Both the numerically integrated position and the position extracted from the closed form perturbation analysis are given for a short period of time, $545\text{s} \leq t \leq 585\text{s}$, at various truncation levels to depict the visual convergence between the two solutions.

In this example case, the total response differs greatly from the purely linear response – the motion achieved with the ϵ_1 term set to zero. This is shown on the zeroth level’s time-motion response for each body where the linear response is extracted from the perturbation method and shown in gray. The complete numerically integrated time-domain response is shown black. This suggests that the manner in which the effective mass parameter is varied, as described in Table 2.1, has had a significant impact on the system’s response. As the number of levels used in the perturbation method increases, its response begins to converge on the time-domain response. In this particular scenario, the spar’s motion is the last to converge. For a different case in which the chosen physical control parameter variation does not significantly effect the system, the linear problem will match the actual response quite closely and very few levels will be required to converge on the proper motion response.

As a result, the extra information added by the higher levels of the perturbation analysis may not be needed. A suitable level to truncate the approximation at will be dependent on the intended use of the solution. In Section 4.2 a suitable level is determined for the above problem based on the convergence of the WEC’s absorbed power.

One could argue that if the run time to evaluate the response of the WEC with a particular control input was sufficiently fast, the truncation level could be set to a very high, practically unlimited, value to ensure convergence using brute force. Unfortunately, the methodology, as presented in its current form, is unable to efficiently evaluate the response with a large number of levels, and an intelligent means to detect convergence and curtail the solution is needed to meet the objective of a computationally efficient calculation. Figure 2.8 gives the amount of computational time and memory required to run the perturbation method versus the selected truncation level. For reference, the computational time required to evaluate the response in the time-domain using numerical-integration for 1000 seconds is provided.

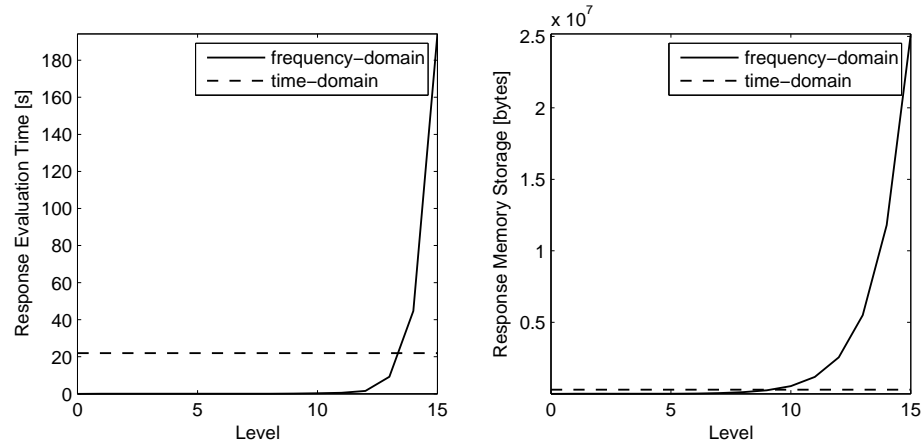


Figure 2.8: Computational efficiency comparison between the perturbation method and traditional time-domain numerical integration. The evaluation speed and memory required for the proposed methodology, in its current state, is much too demanding past the level of $N=13$.

In Figure 2.8, the amount of computational time required to evaluate the WEC's response with the closed form perturbation method described in this chapter grows at an exponential rate with the number of levels required in the solution. After a truncation level of 13, the computational time required to evaluate the perturbation method becomes greater than that of the time-domain response. For the 13th level solution, there is still a benefit to using the proposed perturbation method as it presents the solution as a closed form expression that is favoured for use in an optimization problem. However, soon after this point, the exponential growth in the computation time nullifies the advantages of having the closed form expressions obtained. For a truncation level of $N=22$, the method takes a period of greater than a week to produce a solution.

In Chapter 3, the reasoning behind the exponential growth in computational time is investigated and some adaptations to the methodology presented in this chapter are made to drastically reduce the evaluation time.

Chapter 3

Computational Efficiency

One of the major incentives in moving to a frequency-domain model of a WEC is the robustness and utility of a closed form solution. Unfortunately, these traits, for the perturbation analysis presented in the previous chapter, are compromised by excessively long calculation times. The enormous amount of computational time needed for the perturbation method of Chapter 2 to converge on the motion of the WEC device can be attributed to an exponentially increasing number of linear oscillators equations that are solved on each successive level. In addition, the exponential growth of the number of components within each level of the solution, $\underline{z}_n(t)$, and the subsequent storage of each component's frequency, amplitude, and phase, consumes an amount of memory that is disproportionate to the level of detail that is seen in a complete response: when reviewing the waveforms of Figure 2.7, there should not be a need for a Mb of data in the solution (Figure 2.8). At this point, the number of levels one can include is limited by amount of memory available. Growing at an exponential rate, the array size for a truncation level of $N=20$ would be $3 \times 20 \times 2^{20}$. Even with memory pre-allocated, this memory requirement results in a very inefficient solution procedure.

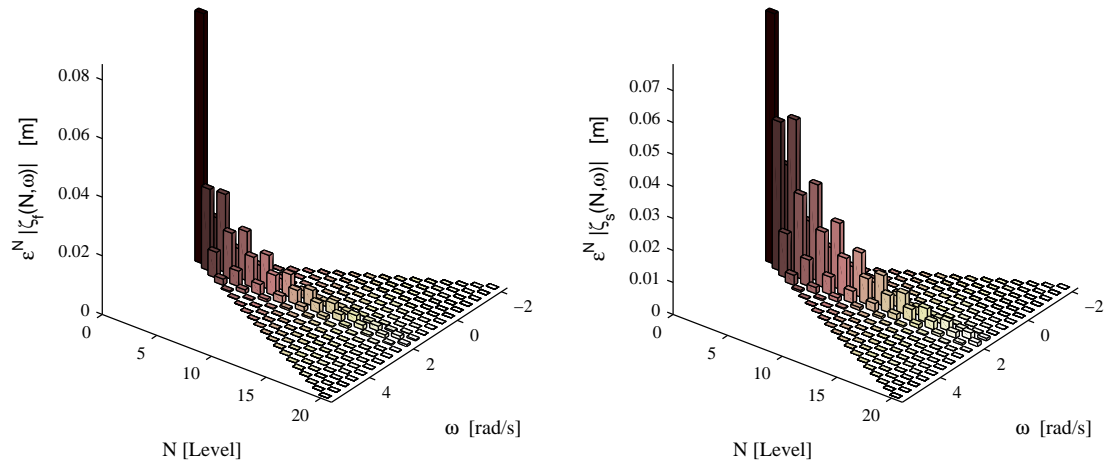
In this chapter the inadequacies of the perturbation method are investigated and drastic improvements are made by reducing the number of component evaluations on each level of the solution. This is done by combining components with shared frequencies, as well as, identifying and eliminating components with negligible contribution to the overall solution.

These time savings strategies present a new way to represent a complete solution with far fewer solution components. As shown in Section 3.3, this improved solution representation permits the development of a closed form expression to gauge the relative travel between the bodies of a WEC.

3.1 WEC Motion Response Calculation

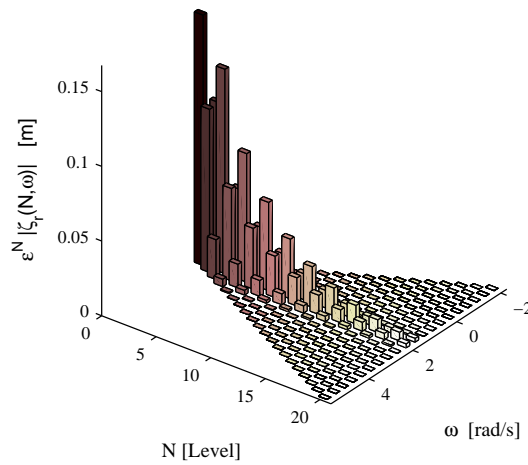
To demonstrate what portions of the solution are essential in producing an accurate response and which components of the solution are superfluous, all of the components calculated in the 20 level solution of the perturbation method are visualized in Figure 3.1 for the system parameters given in Table 2.1. The bar chart of Figure 3.1 displays the absolute magnitudes of each component in the solution versus their respective level and oscillation frequency. It should be noted that the absolute magnitudes displayed in Figure 3.1 contain the ϵ_1^n scalar multiple corresponding to each components respective level. By including the perturbation parameter, a dimensionally consistent comparison of component magnitudes is ensured: the scale of the vertical axis is in meters.

Figure 3.1 shows that the amplitudes of oscillation for the components decay towards a negligible magnitude as the level of the perturbation method is increased. As such, at least for the example case considered, the solution process is stable and given a sufficient amount of computational time and memory, the method should converge on a bounded solution.



(a) Float motion components

(b) Spar motion components



(c) Reaction mass motion components

Figure 3.1: Absolute motion components for each body – the phase information for each component has been removed. All solution components with equivalent frequencies are summed in complex form. Physical parameters for this simulation are given in Table 2.1

3.1.1 Perturbation Method with Shared Frequency Improvements

In the formation of Figure 3.1, components within a specific level that share an oscillation frequency are combined to form a single complex amplitude of oscillation. Analyzing various levels of the solution, it is found that many of the components' oscillation frequencies were repeated both within a level and between levels of the solution. This can be attributed to the fact that each motion component in a preceding level produces two forcing terms in the subsequent level, each differing by the addition or subtraction of the control frequency (for example see Equation (2.66)). These resulting components will then give rise to four new components on the next succeeding level, two of which will be at a frequency that is the same as that which originated the chain of calculations. The difference between the two methods is shown in Figure 3.2 and 3.3.

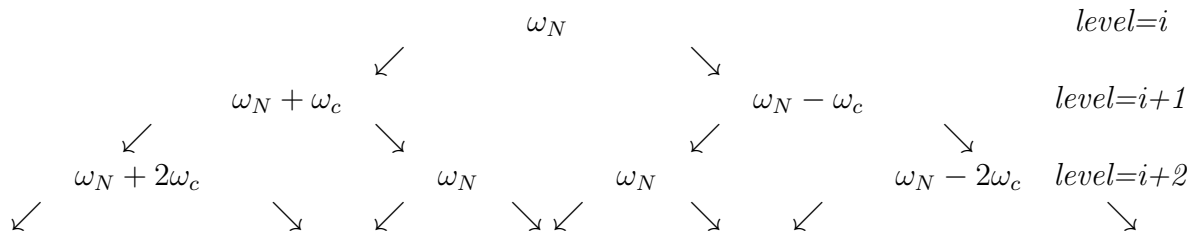


Figure 3.2: The formulation of each subsequent level's oscillation frequencies without the summation of amplitudes of components with equivalent oscillation frequencies

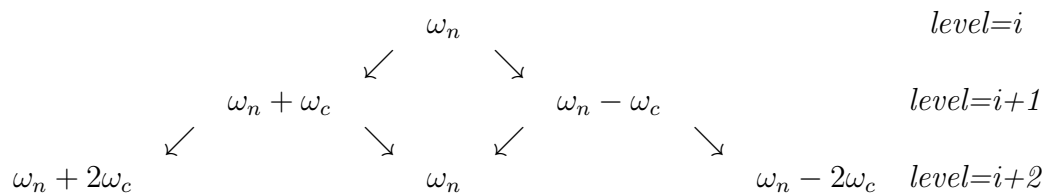


Figure 3.3: The formulation of each subsequent level's oscillation frequencies with the summation of amplitudes of components with shared oscillation frequencies

In either case, only two new unique frequencies present themselves on each successive level, one on each end of the frequency spectrum. This suggests that a mathematical equivalent of the current methodology, which currently grows exponentially from

level-to-level, could be created that exhibits linear growth from level-to-level. This simplification can be executed by summing the complex amplitudes of repeated frequency components of each level before proceeding to the next level. This realization results in some very large computational savings, both in the number of computations saved and the memory required to evaluate a high number of levels.

As shown in Figure 3.1, there is also recurrences of oscillation frequency between the levels. This realization results in two further simplifications: one to the solution process itself and another to the representation of the complete solution with a minimal number of terms.

As discussed in Section 2.4.2, a component's complex amplitude can be evaluated at any arbitrary level of the solution using expressions found in Equation (2.70). The "complex impedance" matrices being inverted on the right-hand side of these expressions contain the same mass, stiffness, and damping components, but differ in the oscillation frequency under consideration for a particular component. Performing the complex impedance matrix inversion for each individual component's frequency is a repeated process performed at a significant computational cost over the duration of a full solution process. Alternatively, if the matrix inversion for a specific frequency is stored in memory, it can be accessed for any subsequent component sharing the same oscillation frequency. Since, only two new unique frequencies are introduced on each successive level, this bookkeeping of the inverted complex impedance is possible, and amounts to substantial computational savings. If the number of levels required for a converged solution are known, along with the incident wave frequency and control frequency parameters, these matrix inversions can be pre-processed, resulting in further savings.

The combined efficiency improvements, resulting from the summation of complex amplitudes sharing oscillation frequency and the bookkeeping of complex impedance matrix inversions, will here after be referred to as the *perturbation method with shared frequency improvements*. The computational savings resulting from these improvements are drastic, and computational time and memory storage requirements have been tabulated for various solution truncation levels in Table 3.1. As shown, the improved method is capable of evaluating the device's response in a fraction of the time required by traditional time-domain techniques. This is a drastic improvement

over the original method presented in Chapter 2, where the time required to evaluate to a truncation level of $N=20$ has been reduced from a week (or more) to a fraction of a second.

Table 3.1: Computational time and memory storage requirements of WEC device response evaluation for both a Runge-Kutta-Fehlberg numerical integration time-domain method and perturbation method with shared frequency improvements.

Time-Domain Numerical Integration		
Time Span [s]	Computational Time [s]	Memory Storage [bytes]
600	8	288048
Perturbation Method with Shared Frequency Improvements		
Truncation Level [s]	Computational Time [s]	Memory Storage [bytes]
5	0.05	408
10	0.07	1368
15	0.09	2928
20	0.11	5088
25	0.14	7248
30	0.18	11208
35	0.22	15168
40	0.26	19728
45	0.30	24888
50	0.35	29488

3.1.2 Solution Representation Simplification

In an effort to reduce the number components required to accurately model the final device response, the shared oscillation frequencies of components between levels are again exploited. The complex amplitudes of these components can be added together so long as each complex amplitude has been pre-multiplied by their level's corresponding scalar multiple of the perturbation parameter, ϵ_1^N . The three-dimensional bar chart of Figure 3.1 can then be projected onto an amplitude and oscillation frequency plane, as shown in Figure 3.4. Where the summed complex amplitudes are differentiated from their level dependent counter parts with the symbol that is independent on solution level, $\vec{\zeta}(\omega)$.

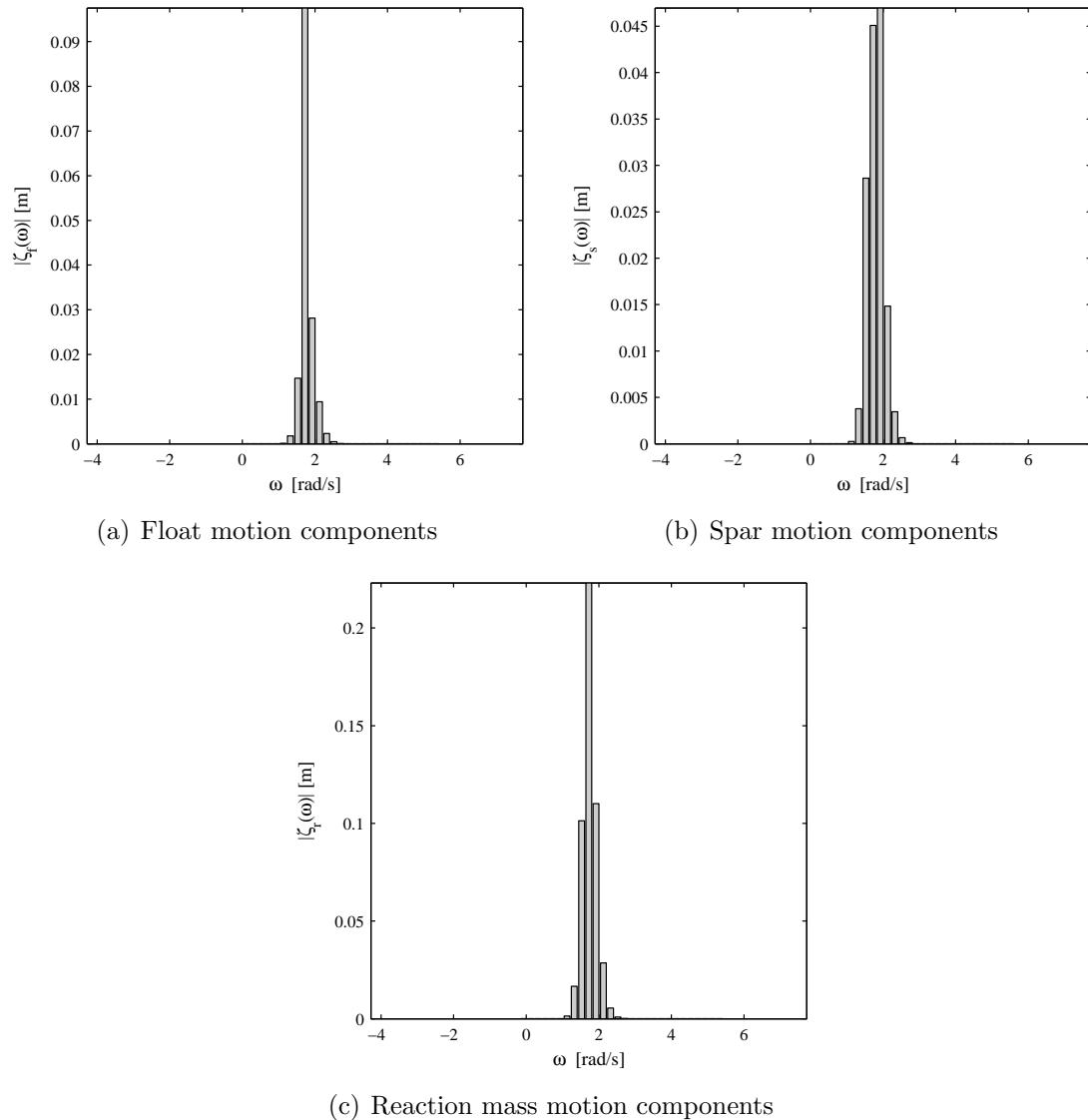


Figure 3.4: Absolute motion components for each body. All solution components with equivalent frequencies, both within and across levels of the solution, are summed in complex form and then reported as amplitudes. Physical parameters for this example problem that generated the solution are given in Table 2.1

This simplification does not produce any computational benefit in the component evaluation process, rather it compresses all the components within the solution allowing it to be represented as a superposition of far fewer components. The following can be used in place of Equation (2.71) to define the WEC motion, here after referred

to as the *compressed solution representation*:

$$\underline{z}(t) = \sum_{j=1}^{2N_{max}} \left\{ 2|\underline{\zeta}(\omega_j)| \cos(\omega_j t + \theta(\omega_j)) \right\} \quad (3.1)$$

Where

$$\omega_j = \omega_i - \omega_j(N_{max} - j) \quad (3.2)$$

At first glance, this simplification may seem to have limited benefit, as it does not provide any computational savings to the perturbation method itself; however, it has implications in the synthesis of a time-motion response of the WEC, the absorbed power calculation that is presented in Section 4.1, and the relative travel constraint analysis presented in Section 3.3.

The combination of components with equivalent oscillation frequencies across the levels, results in the computational time required to evaluate the power absorption expressions presented in Section 4.1 to be greatly reduced. Instead of evaluating $(2^N - 2)^2$ combinations of relative amplitude components using the definite integral expressions presented in that section, the compressed solution representation requires only $2N^2 - N$ function evaluations. When a high number of levels are required for a converged solution, the savings are quite large: for a solution with a truncation level of $N=20$, the number of terms in the gross power calculation drops from 1.1×10^{13} to 780. This is of particular importance when employing the methodology in an iterative optimization routine that depends on numerous evaluations of the converted power to guide the selection of physical specification and control inputs.

3.2 WEC Response Bandwidth Limitation

One observation drawn from Figures 3.1 and 3.4, is that there is a relatively narrow bandwidth exhibiting non-negligible component amplitudes. This is to be expected, as point-absorbing WECs typically perform optimally over a relatively narrow bandwidth. As a result, it is expected that substantial computational savings can be achieved by identifying that bandwidth and limiting the calculations to frequencies within it.

To assess an appropriate bandwidth limitation, the device's heave response amplitude operator is believed to be a suitable metric. A response amplitude operator, or RAO, is effectively a transfer function used to gauge the response of the device to a particular forcing frequency and shape. The forcing shape is the combination of complex force applied to the WEC's three bodies; the float, the spar and the reaction mass. For the zeroth level component, the RAO can be found by evaluating the right hand side of Equation 2.34 and dividing by its magnitude.

$$\frac{[-\omega^2 \mathbf{M}_L + i\omega \mathbf{C}_L + \mathbf{K}]^{-1} \left[\vec{\underline{f}}_e \left| \frac{1}{2} e^{i\theta_e} \right. \right]}{\| [-\omega^2 \mathbf{M}_L + i\omega \mathbf{C}_L + \mathbf{K}]^{-1} \left[\vec{\underline{f}}_e \left| \frac{1}{2} e^{i\theta_e} \right. \right] \|} \quad (3.3)$$

Where the zeroth level's forcing shape is as follows:

$$\frac{\vec{\underline{f}}_e}{\|\vec{\underline{f}}_e\|} \quad (3.4)$$

A common forcing shape for all other components of the solution can be found by evaluating the right-hand side of Equation (2.68). This is shown for a single arbitrary solution component $\vec{\zeta}_N^{(j)}$ below in Equation (3.5). Where 'const' corresponds to the remaining scalar multiples found on the right-hand side of Equation (2.70) for the j^{th} component.

$$\begin{bmatrix} 0 & 0 & 0 \\ 0 & 1 & -1 \\ 0 & -1 & 1 \end{bmatrix} \begin{bmatrix} \zeta_{f,N}^{(j)} \\ \zeta_{s,N}^{(j)} \\ \zeta_{r,N}^{(j)} \end{bmatrix} \times \text{const} = \begin{bmatrix} 0 \\ \zeta_{s,N}^{(j)} - \zeta_{r,N}^{(j)} \\ \zeta_{r,N}^{(j)} - \zeta_{s,N}^{(j)} \end{bmatrix} = \begin{bmatrix} 0 \\ 1 \\ -1 \end{bmatrix} \times \text{const} \quad (3.5)$$

The chosen control parameters, ϵ_0 and c_g , are then inserted into the mass and damping matrices, \mathbf{M}_L and \mathbf{C}_L , as per Equations (2.11) and (2.12) to form the complex impedance matrix below:

$$[-\omega^2\mathbf{M}_L + i\omega\mathbf{C}_L + \mathbf{K}_L] \quad (3.6)$$

The response amplitude operators can be evaluated by multiplying the inverted dynamics matrix by the normalized forcing shape and scaling by the effective mass variation, ϵ_1 , as shown in Equation (3.7). This multiplication by ϵ_1 ensures that the RAO remains dimensionless and is necessary to properly represent how the previous level's solution component - captured within the forcing shape - translates into magnitude of the current level's component.

$$\text{RAO}(\omega) = \epsilon_1 [-\omega^2\mathbf{M}_L + i\omega\mathbf{C}_L + \mathbf{K}_L]^{-1} \begin{bmatrix} 0 \\ \frac{1}{\sqrt{2}} \\ -\frac{1}{\sqrt{2}} \end{bmatrix} \quad (3.7)$$

The results of the RAO calculation, for the particular set of control variables considered in Table 2.1, are shown in Figures 3.5(a), 3.5(c) and 3.5(e) on the oscillation frequency-component magnitude plane. As shown, the RAO is symmetrical about the vertical axis - the device will react in the same manner to an equivalent phasor rotating in the opposite direction. From these figures, it is noted that there are no significant component magnitudes below corresponding to negative frequencies. This is to be expected, as the RAO's value between the two RAO lobes is small enough that all components propagating from the positive frequencies decay at a rate such that they are negligible when the second lobe is reached in the $\omega < 0$ range.

There is a strong correlation between the RAO and the magnitudes of components at their respective oscillatory frequencies. For these frequencies where the RAO approaches zero, the magnitude of the corresponding components are found to be negligible. This would suggest that the solution process can be restricted to the range of frequencies where RAO values are significant. This results in the elimination of a large number of superfluous linear oscillator equations being evaluated.

While the RAO provides a guideline for a low and high frequency cutoff, care must be taken in selection the cutoff values. Though a solution component's frequency of oscillation may appear to be in a region where the component will have a negligible effect on the overall solution, each component will be responsible for generating new components on subsequent levels which could propagate towards a region where the frequency of oscillation is non-negligible. If a component is sufficiently far outside the region where the RAO is non-negligible, the subsequent components will die out before getting to a frequency in the RAO where a significant magnitude could be produced. To determine at what upper and lower frequency the solution's bandwidth could be limited to without significantly effecting the solution, a test was done. The lower bandwidth limit was varied from the most negative frequency of a complete solution, evaluated to the 45th level and known to be converged from Figure 2.6, up to the incident wave forcing frequency. A normalized 2-norm error, Equation (3.8), was determined by comparing the time-series response of the WEC of the bandwidth limited solution, $\underline{z}_{band-lim}$, to the converged 45 level solution, \underline{z}_{true} , shown by \square 's in Figures 3.5(b), 3.5(d) and 3.5(f). This process was then repeated for the upper bandwidth limit, represented by \times 's in the same figures.

$$\Delta = \frac{\|\underline{z}_{true} - \underline{z}_{band-lim}\|}{\|\underline{z}_{true}\|} \quad (3.8)$$

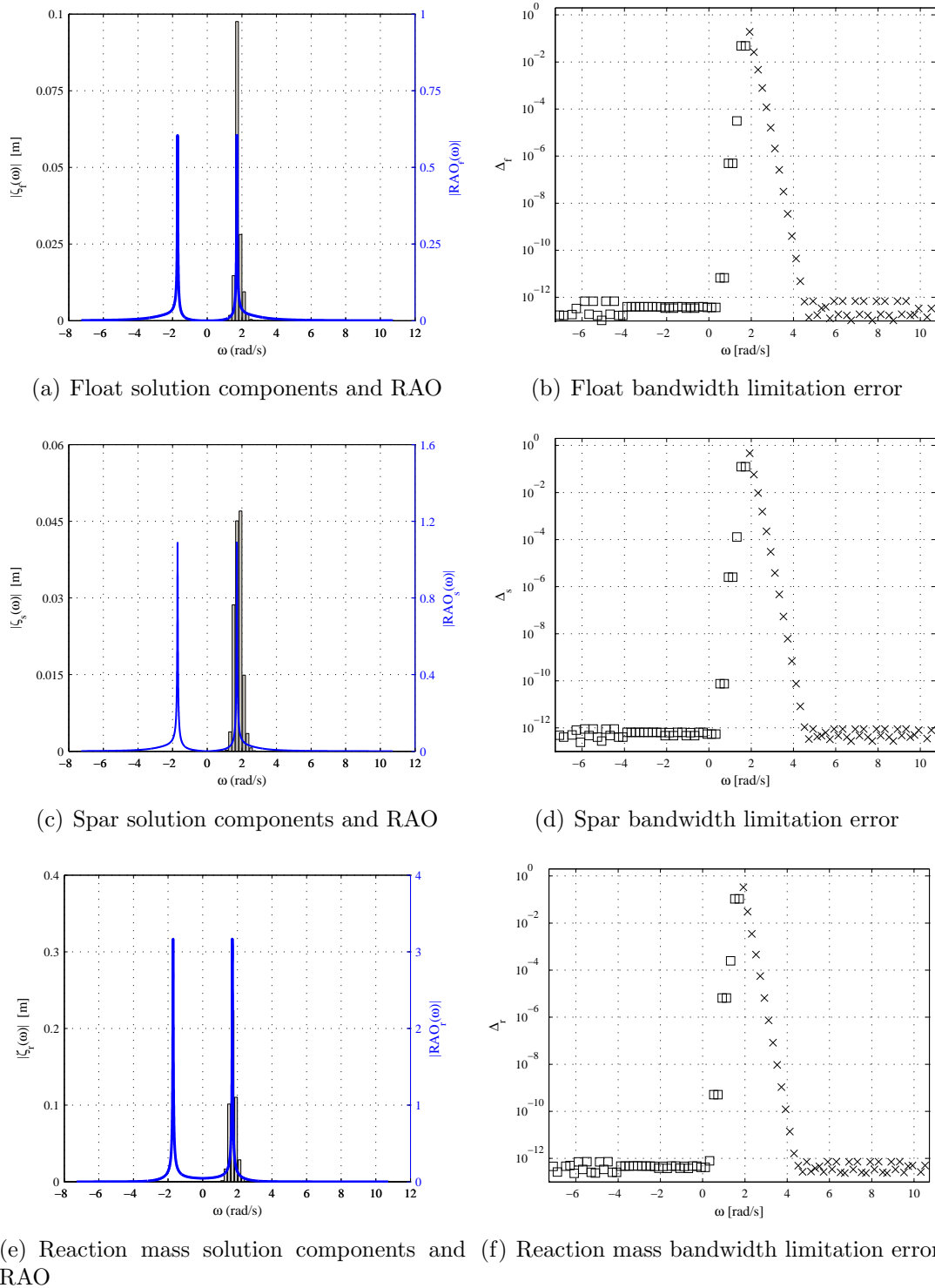


Figure 3.5: The solution components that are most important in creating an accurate time-motion response are visually evaluated by comparing the solution component magnitudes to their RAO (a),(c) and (e). The 2-norm errors associated with bandwidth limitation are shown in (b),(d) and (f).

The results of the bandwidth limiting test show that, for this particular test, the solution can still be adequately represented with a components that are limited to a much smaller oscillation frequency bandwidth than what has been suggested by the development of the perturbation method. This results in significantly fewer components required to be evaluated and stored in memory to produce an accurate device response.

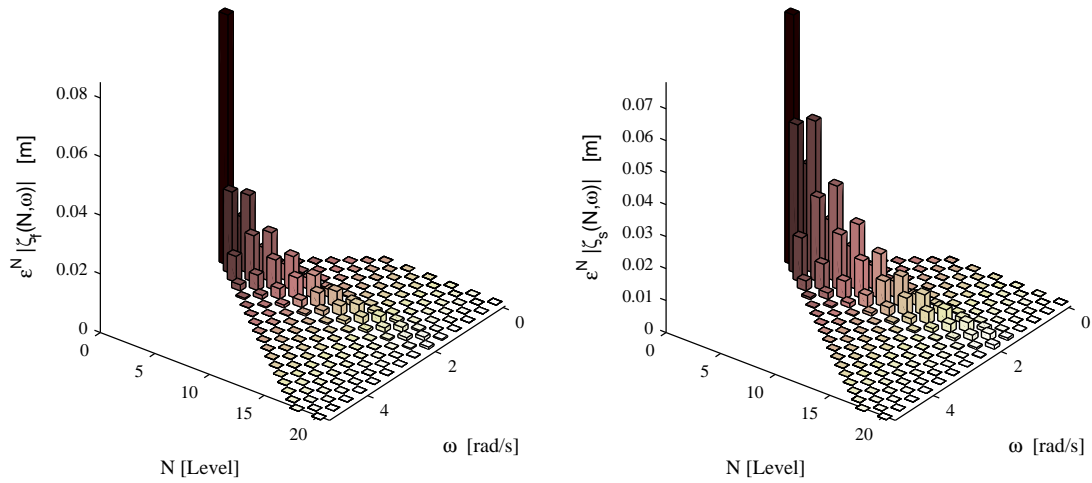
The manner in which the response of the device is evaluated does not allow for the bandwidth cut off to be different for each of the device's body. As a result, the limits must be set such that the response of each of the device's bodies are not compromised. Examining Figures 3.5(b), 3.5(d) and 3.5(f), there appears to be a frequency limit on each side of the incident wave forcing frequency where the response error starts to increase rapidly for each of the device's bodies - approximately $0 \frac{\text{rad}}{\text{s}}$ for the lower frequency limit and $5 \frac{\text{rad}}{\text{s}}$. These frequency limits roughly correspond to an RAO value of 0.04 and 0.004 for the lower and upper frequency limits, respectively. By precalculating the RAO for a particular parameter selection and determining the frequencies that correspond to the RAO limit values, 0.04 and 0.004, the components making up the solution can be limited to a bandwidth associated with that particular parameter selection. The RAO limits found above should act as a good guideline for other device parameter selection; however, without extensive testing the validity can't be known.

To display the computational benefits of limiting the bandwidth a comparison case was done where the component oscillation frequency bandwidth was limited to the range given above, $0 \frac{\text{rad}}{\text{s}} \leq \omega \leq 5 \frac{\text{rad}}{\text{s}}$. These results were then compared to the perturbation method with shared frequency improvements presented in Section 3.1.1, the results are shown in Table 3.2.

Table 3.2: Computational time and memory storage requirements of WEC device response evaluation for the improved perturbation method and the improved perturbation method with limited bandwidth, $0\frac{\text{rad}}{\text{s}} \leq \omega \leq 5\frac{\text{rad}}{\text{s}}$.

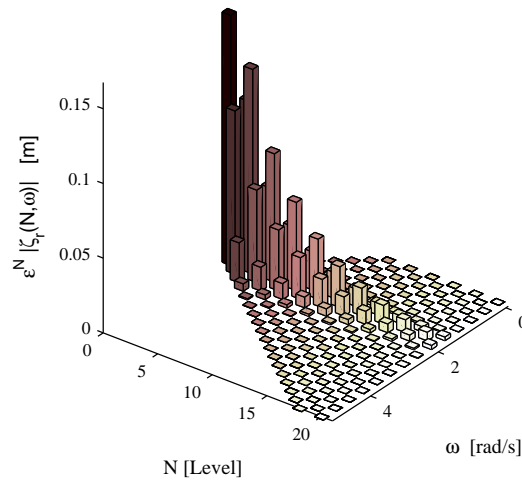
Perturbation Method with Shared Frequency Improvements		
Truncation Level [s]	Computational Time [s]	Memory Storage [bytes]
5	0.017	3848
10	0.026	12328
15	0.035	25608
20	0.059	43688
25	0.072	66568
30	0.095	94248
35	0.143	126728
40	0.182	164008
45	0.241	206088
50	0.278	252968
Perturbation Method with Shared Frequency Improvements and Bandwidth Limitation		
Truncation Level [s]	Computational Time [s]	Memory Storage [bytes]
5	0.017	3848
10	0.024	11256
15	0.036	20176
20	0.039	27432
25	0.047	33912
30	0.063	40392
35	0.072	46872
40	0.075	53352
45	0.087	59832
50	0.094	66312

The results given in Table 3.2 show that there are significant computational savings to be had by using bandwidth limitation in conjunction with the shared frequency improvements of Section 3.1.1. Although the RAO does act as a guide for bandwidth truncation, no formal rule has been found to determine appropriate bandwidth truncation for all cases. As a result, the expressions presented in the remainder of this thesis will assume the device's response is represented using the full frequency bandwidth.



(a) Float motion components

(b) Spar motion components



(c) Reaction mass motion components

Figure 3.6: Absolute motion components for each body for the bandwidth limited improved perturbation method. Solution components have been limited to oscillation frequencies within $0 \frac{rad}{s} \leq \omega \leq 5 \frac{rad}{s}$. Physical parameters for this simulation are given in Table 2.1

3.3 Significant Relative Travel

In the preceding sections a methodology was presented to evaluate the WEC motion response induced by regular wave forcing and periodic variations of an intrinsic control parameter. Given that the evaluation process is fast, robust and programmable, it can be embedded in an optimization routine used to search for optimal amplitude and phase of the control parameter. In that process, the obvious choice of objective function is the negative of the average absorbed power and the calculation of that metric is presented in Chapter 4. However, the WEC's motion response for a particular variation of the control parameters must not violate real world travel limitations. In keeping with the use of closed form expressions to this point, this section presents a closed form expression to gauge the relative travel between the bodies of a WEC and compare it to allowable levels.

As presented in Section 3.1.2, assuming a complete solution, the device's response can be adequately represented with significantly fewer solution components than that of the raw methodology presented in the previous chapter. This compressed solution representation, shown in Equation (3.1), can be easily modified to describe the relative motion between the WEC's bodies by evaluating relative travel component amplitudes, $\vec{\zeta}_f(\omega)$ and $\vec{\zeta}_s(\omega)$:

$$\vec{\zeta}_f(\omega) = \vec{\zeta}_f(\omega) - \vec{\zeta}_s(\omega) \quad (3.9)$$

$$\theta_{f/s}(\omega) = \text{atan2} \left\{ \frac{\Im \left\{ \vec{\zeta}_f(\omega) \right\}}{\Re \left\{ \vec{\zeta}_f(\omega) \right\}} \right\} \quad (3.10)$$

$$\vec{\zeta}_r(\omega) = \vec{\zeta}_r(\omega) - \vec{\zeta}_s(\omega) \quad (3.11)$$

$$\theta_{r/s}(\omega) = \text{atan2} \left\{ \frac{\Im \left\{ \vec{\zeta}_r(\omega) \right\}}{\Re \left\{ \vec{\zeta}_r(\omega) \right\}} \right\} \quad (3.12)$$

The maximum absolute relative travel could be evaluated by constructing a time-series from these relative travel components and obtaining its maximum, according to Equation (3.14) and (3.16).

$$z_{\frac{f}{s}}(t) = \sum_{j=1}^{2N_{max}} \left\{ 2|\vec{\zeta}_{\frac{f}{s}}(\omega_j)| \cos(\omega_j t + \theta_{\frac{f}{s}}(\omega_j)) \right\} \quad (3.13)$$

$$z_{\frac{f}{s}max} = \max \left\{ |z_{\frac{f}{s}}(t)| \right\} \quad (3.14)$$

$$z_{\frac{r}{s}}(t) = \sum_{j=1}^{2N_{max}} \left\{ 2|\vec{\zeta}_{\frac{r}{s}}(\omega_j)| \cos(\omega_j t + \theta_{\frac{r}{s}}(\omega_j)) \right\} \quad (3.15)$$

$$z_{\frac{r}{s}max} = \max \left\{ |z_{\frac{r}{s}}(t)| \right\} \quad (3.16)$$

Where ω_j are the discrete component frequencies governed by:

$$\omega_j = \omega_i - (N_{max} - j + 1)\omega_c \quad (3.17)$$

Constraint violations could be evaluated by comparing this singular maximum value against its respective travel limitation given in Table 1.1. However, this technique would be problematic if it were introduced into an automated optimization - a beneficial control parameter setting may be completely disregarded if a travel constraint was violated very infrequently. In actuality, any physical device would have some mechanical means for preventing travel constraint violations, or end-stop collisions, and it is entirely reasonable that such minuscule violations would be effectively mitigated. As such, what is desired here is a manner to quantify the magnitude of the violation and the level at which it persists. This condensed summary, a statistical description, must be capable of describing the extent of the violation without excessive computations.

The statistical description of the relative travel is similar to the definition of wave height in an irregular sea: the wave component magnitudes and frequencies are known, and the exact displacement from equilibrium is only attained through a time series expansion[31]. The main difference in the problem at hand is that the phase of the relative travel components are known, whereas they are assumed to be random, or Gauss distributed, in sea-state analysis. In sea-state analysis, a simple closed form expression using a probabilistic based approach is used to evaluate wave height metrics, avoiding the generation, storage, and analysis of a detailed time-series. A common wave height metric used by ocean engineers is a significant wave height - the average of the highest one-third of the waves produced by a given sea-state.

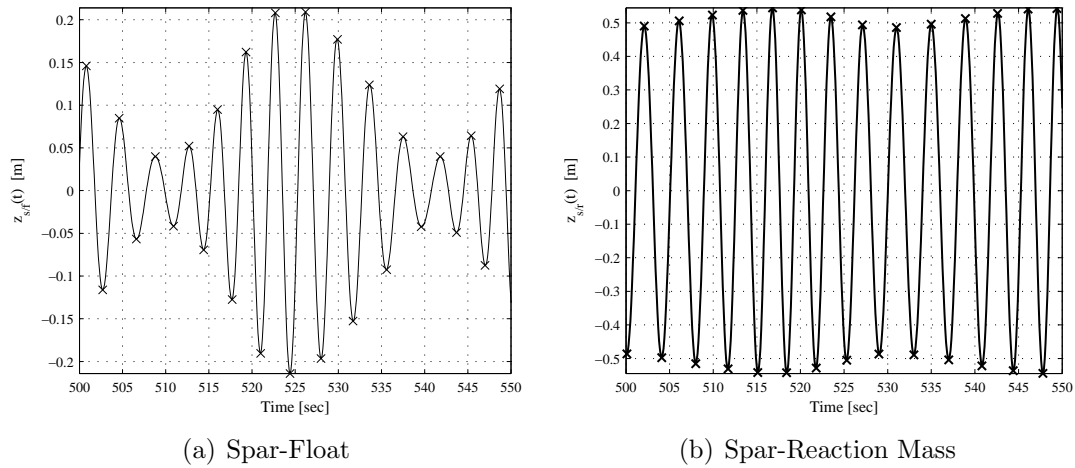


Figure 3.7: Relative motion response. Physical parameters for this simulation are given in Table 2.1.

Because of the similarity between the problems, the sea-state analysis techniques will be used to guide to generate a useful relative travel metric. To do so, two assumptions about the relative motion solution components must be made:

1. The relative travel components are assumed to be within a narrow bandwidth.
2. The known component phases must be neglected and the components phases will be assumed to be random.

The first assumption ensures that the majority of local maxima and minima associated with the relative travel of the WEC's bodies remain above and below the zero crossing, respectively. This is a valid assumption, as shown in Figure 3.3, and discussed in Section 3.2: the motion components which are of a significant amplitude tend to fall within a relatively narrow bandwidth.

The second assumption allows for the variance of each component to be summed together to obtain the variance in the overall travel. As shown in Figures 3.8(a) and 3.8(b), the relative travel component phases are not Gaussian; however, by neglecting the known phase and assuming a Gaussian distribution, this particular device response is encompassed by all the possible device responses created with relative travel components of the given magnitude. The random phase assumption enables one to determine the probability that, for the given relative travel component magnitudes, the relative motion exceeds a particular height.

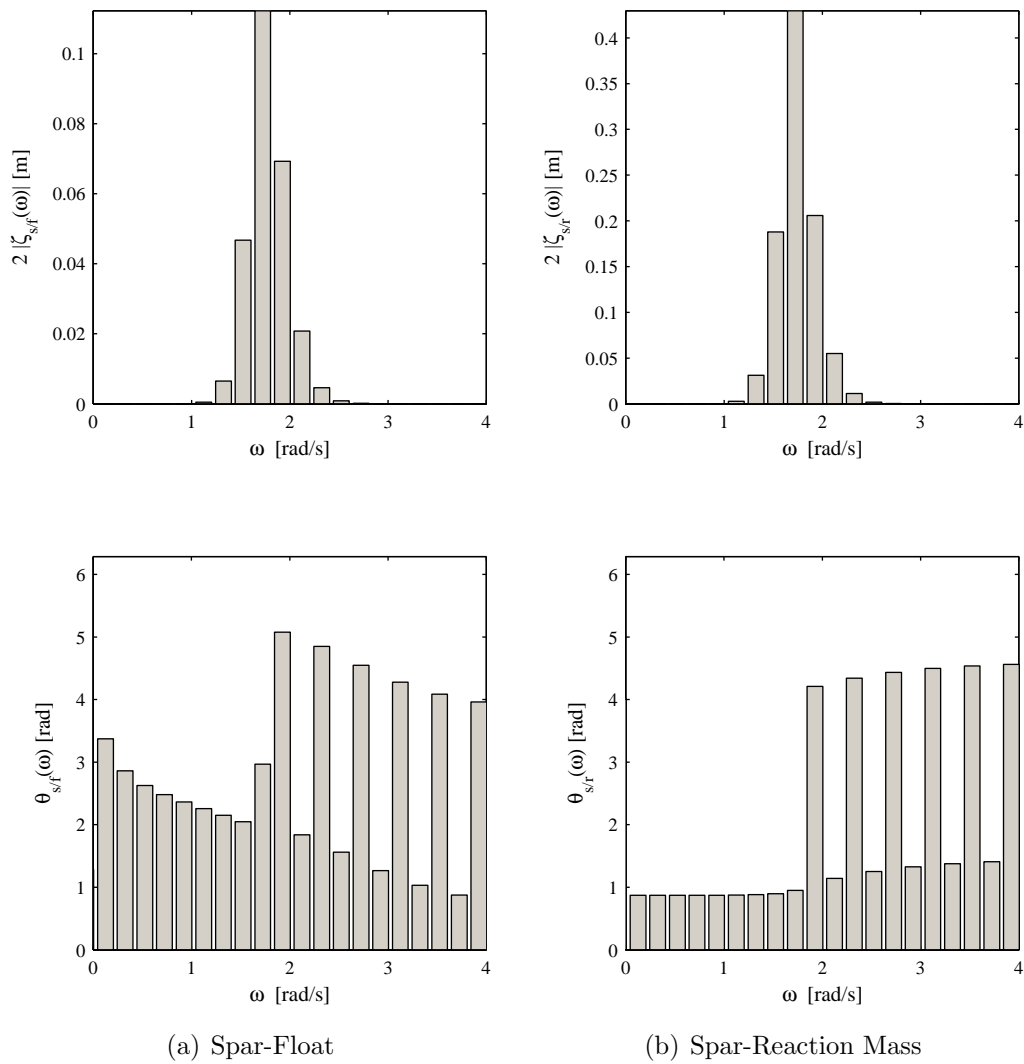


Figure 3.8: Relative motion component magnitudes and phases. Physical parameters for this simulation are given in Table 2.1. Note: the component magnitudes have been multiplied by two to adhere with the complex conjugate simplification introduced in Section 2.4.

With these assumptions the probability density function for the WEC bodies' relative travel heights, H_r , can be modelled as the Rayleigh distribution given below[31]:

$$p(H_r) = \frac{H_r}{4m_0} e^{\left(-\frac{H_r^2}{8m_0}\right)} \quad (3.18)$$

This probability density function is solely dependent on one parameter, the zeroth-ordered moment of the solution components' variance density spectrum:

$$\begin{aligned}
 m_0 &= \int_{-\infty}^{+\infty} |\vec{\zeta}(\omega)|^2 d\omega \\
 &= \omega_c \sum_{j=1}^{2N_{max}} |\vec{\zeta}(\omega_j)|^2
 \end{aligned}
 \tag{3.19}$$

Where the width of the discrete variance density spectrum is ω_c .

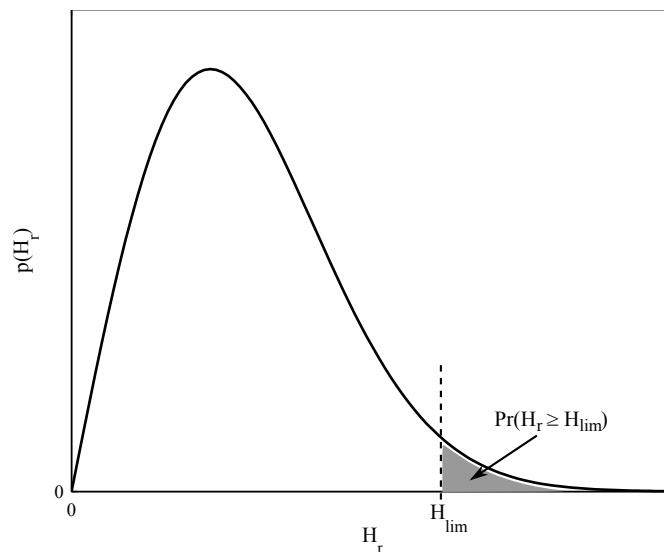


Figure 3.9: The Rayleigh probability density function for relative motion between a WEC's bodies. An area calculated under this function can be used to find the probability that the relative motion, H_r , exceeds a certain height, H_{lim} , shown here in grey.

An example Rayleigh distribution of the probability density function has been plotted in Figure 3.9. From this distribution the probability of relative travel motion exceeding a particular height can be found for a given set of relative travel components. This is done by integrating the probability density function from a lower-limit of the relative travel height of interest, $H_r = H_{lim}$, to the upper-limit of $H_r = H_\infty$, as seen in Equation (3.20).

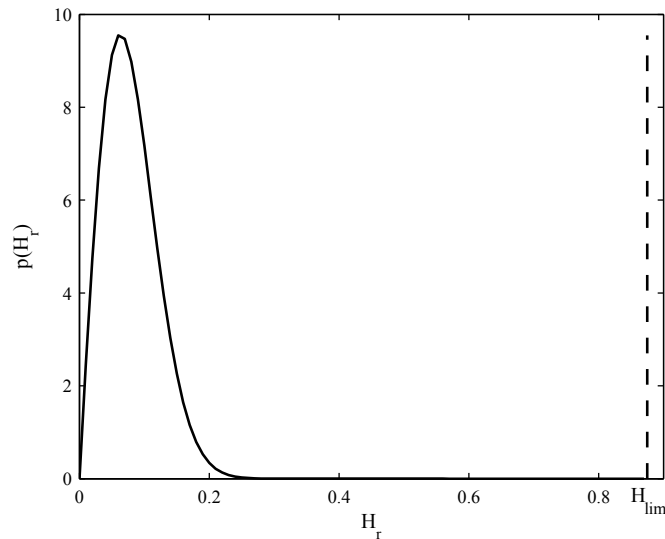
$$\begin{aligned}
Pr(H_r \geq H_{lim}) &= \int_{H_{lim}}^{+\infty} p(H_r) dH_r \\
&= \int_{H_{lim}}^{+\infty} \frac{H_r}{4m_0} e^{-\left(\frac{H_r^2}{8m_0}\right)} dH_r \\
&= e^{-\left(\frac{H_{lim}^2}{8m_0}\right)} - e^{-\left(\frac{\infty^2}{8m_0}\right)} \\
&= e^{-\left(\frac{H_{lim}^2}{8m_0}\right)}
\end{aligned} \tag{3.20}$$

With this result, a simple and succinct measure of probability that the WEC bodies' relative travel will exceed a certain motion height, $Pr(H_r \geq H_{lim})$, has been found. To ensure that the relative travel constraints given in Table 1.1 are not exceeded, their limits are placed into Equation (3.20) as the lower limit of integration. For the case study given in Table 2.1, the probability that the float-spar and spar-reaction mass relative travel motions exceeded their limits was found to be essentially zero, as shown in Figure 3.10. This result is expected as the inflated absolute maximum relative travel height that could occur, found by summing the set of relative motion amplitudes given in Figure 3.3, is even less than the physical constraint.

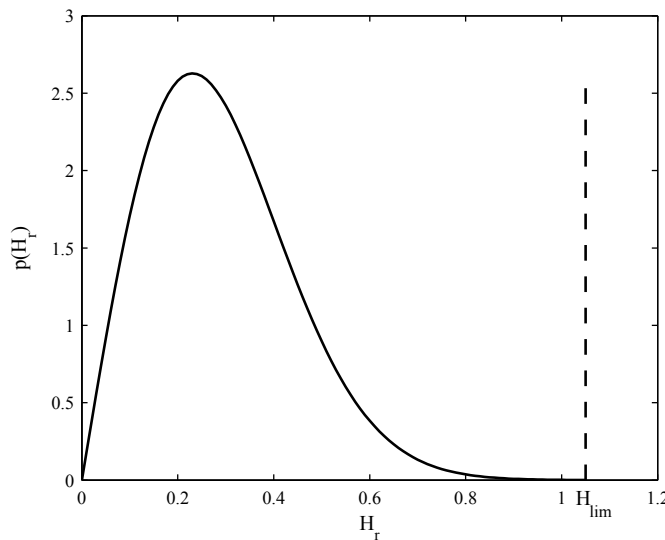
This closed form approach gives a good indication whether or not the relative motion constraints are likely to be violated, but it remains to include this measure include this measure in an automated search for a good control parameter selection. At this point, it is unclear what probability level would be acceptable. A very conservative approach would be to disregard any design iterations with any probability of a travel constraint violation; however, this would possibly eliminate some design iterations that have promising power absorption and managable travels. Alternatively, what is suggested here is a sliding penalty function that would incrementally penalize any design with incremented increases in the probability of constraint violation. A preliminary expression for the sliding penalty function is given in Equation (3.21); however, further investigation is needed to assess whether it is too lenient or too strict.

$$P_{net} = P_{net} (1 - \alpha Pr(H_r \geq H_{lim})) \tag{3.21}$$

Another approach could be setting a constraint on the probability of the relative travel violating the physical travel limits. If the probability of surpassing the physical travel limit, $Pr(H_r \geq H_{lim})$, were to exceed the constraint, Pr_{max} , the design iteration would be disregarded.



(a) Float-Spar



(b) Spar-Reaction Mass

Figure 3.10: Physical relative travel constraints are shown over the probability density function. The relative height travel constraints, H_{lim} , were taken as twice the amplitude constraints given in Table 1.1. Physical parameters for this simulation are given in Table 2.1

Chapter 4

Net Power Absorption

In the previous chapter, the perturbation method was improved by exploiting known repetition in some of the calculations, and an ability to limit the extent of calculations in the frequency domain. With these improvements, the motion response of a WEC, subject to regular waves and periodically varying control parameters, can be evaluated in a timely manner. However, to determine the benefits of a particular control strategy, there remains a need for a fast, accurate calculation of power that can be used as a metric for comparison of control strategies. In Section 4.1, a means to calculate average gross power absorption by the power take-off unit is investigated.

Unfortunately, this does not provide a complete image of the net power absorption of the device; to produce the desired effective-mass variation control, energy must be consumed. In Section 4.3, a means to accurately quantify the average power consumed to actuate the effective mass for any given control wave form is provided.

This provides the user with the ability to accurately analyze the net benefit associated with the addition of a periodically varying effective mass term, and provides a valuable tool to quantify the desirability of a particular control scheme within an optimization.

4.1 Gross Power Absorption Expression

For the purposes of this study, the power take-off has been modeled as a linear viscous dashpot. The force applied over a linear viscous dashpot is equal to the relative velocity of the float and spar multiplied by the dashpot's damping coefficient.

As suggested in Section 3.1.2, once the solution is complete, all levels' components can be compressed – terms with like frequencies are combined and the solution is expressed as a single summation across an array of frequency-dependent terms. This solution compression results in a significant reduction in the number of components required to accurately represent the relative motion of the device, and will significantly reduce the computational requirement of the power-absorption function. A compressed expression for the relative displacement and velocity of the float and spar bodies are given below in Equations (4.1) and (4.2). Here, ω_j corresponds to the component oscillation frequency under consideration with amplitude $2|\zeta_{\frac{f}{s}j}|$ and phase $\theta_{\frac{f}{s}j}$, which are a result of the complex summation of all the level's components with an oscillation frequency equivalent to ω_j .

$$z_{\frac{f}{s}}(t) = \sum_{j=1}^{2N_{max}} \left\{ 2|\zeta_{\frac{f}{s}}(\omega_j)| \cos(\omega_j t + \theta_{\frac{f}{s}}(\omega_j)) \right\} \quad (4.1)$$

$$\dot{z}_{\frac{f}{s}}(t) = \sum_{j=1}^{2N_{max}} \left\{ 2\omega_j |\zeta_{\frac{f}{s}}(\omega_j)| \sin(\omega_j t + \theta_{\frac{f}{s}}(\omega_j)) \right\} \quad (4.2)$$

Where

$$\omega_j = \omega_i - \omega_j(N_{max} - j) \quad (4.3)$$

$$\bar{\zeta}_{\frac{f}{s},N}^{(j)} = \bar{\zeta}_{f,N}^{(j)} - \bar{\zeta}_{s,N}^{(j)} \quad (4.4)$$

$$\theta_{\frac{f}{s},N}^{(j)} = \text{atan2} \left(\frac{\Im \left\{ \bar{\zeta}_{\frac{f}{s},N}^{(j)} \right\}}{\Re \left\{ \bar{\zeta}_{\frac{f}{s},N}^{(j)} \right\}} \right) \quad (4.5)$$

The energy dissipated over the linear viscous dashpot is then the time integration of the force applied over the dashpot multiplied by the relative velocity between the float and spar.

$$E = \int f(t) \dot{z}_{\frac{f}{s}}(t) dt \quad (4.6)$$

$$= \int c_g \dot{z}_{\frac{f}{s}}^2(t) dt \quad (4.7)$$

The average power dissipated over the linear dashpot is analogous to the average power absorbed by a WEC's power take-off, and is found by dividing the total energy dissipated over the dashpot by the device's oscillation period, T :

$$P_{avg} = \frac{c_g}{T} \int_0^T \dot{z}_{\frac{f}{s}}^2(t) dt \quad (4.8)$$

Substituting Equation (4.2) in Equation (4.8) results in:

$$P_{avg} = \frac{c_g}{T} \int_0^T \left[\sum_{j=1}^{2N_{max}} \left\{ 2\omega_j |\zeta_{\frac{f}{s}}(\omega_j)| \sin(\omega_j t + \theta_{\frac{f}{s}j}) \right\} \right]^2 dt \quad (4.9)$$

The relative velocity squared in Equation (4.9) results in each component being multiplied by each other component in the compressed solution, producing $4N_{max}^2$ terms in the integrand. Each of these terms can be categorized into three definite integral types based on their oscillation frequency and phase. The first type occurs when a portion of the motion response is multiplied by itself:

$$\int_0^T \sin(at + b)^2 dt = \frac{T}{2} + \frac{\sin(2b) - \sin(2b + 2aT)}{4a} \quad (4.10)$$

The second type occurs when a portion of the motion response is multiplied by another portion of the response with a different oscillation frequency and phase:

$$\begin{aligned} \int_0^T \sin(at + b) \sin(ct + d) dt &= -\frac{a(\cos(b + aT) \sin(d + cT) - \cos(b) \sin(d))}{a^2 - c^2} \\ &+ \frac{c(\cos(d + cT) \sin(b + aT) + \cos(d) \sin(b))}{a^2 - c^2} \end{aligned} \quad (4.11)$$

Finally, the third type occurs as a special case of the second type where the two multiplied responses oscillate at the same frequency but have a differing direction of phasor rotation. The solution provided below eliminates the possibility of having a zero in the denominator of Equation (4.11).

$$\int_0^T \sin(at + b) \sin(-at + d) dt = \frac{\sin(b - d + 2aT) - \sin(b - d)}{4a} - \frac{T \cos(b + d)}{2} \quad (4.12)$$

The power associated with each relative motion component is evaluated by it being multiplied by all of the components making up the solution; the oscillation frequency and phase of the components being multiplied are then used to determine the definite integral type and the average power associated with the term is evaluated. By summing each of these averaged absorbed power terms, the gross average power absorption by the WEC can be found.

4.2 Gross Power Absorption Convergence Analysis

To have a true average power, the time over which the definite integral of Equation (4.9) is evaluated should be a full period of periodic relative motion between the float and the spar, T . To determine this period for a device response with a large number of oscillatory components is extremely difficult. As a result, an approximation of Equation (4.9) is used to generate an accurate estimate of the average power absorbed.

To verify this approximation, the average absorbed power is first found for a relative motion time-series created using traditional time-domain based techniques. First, a time-domain simulation for the case study described in Table 2.1 is evaluated for an extended period of time – where there is little doubt that the motion has converged on steady state motion. Second, the end time of the simulation is set to the upper limit of the integration interval, while the lower limit of the integration interval is varied. The size of the interval will be dependent on how far the back in time the lower limit is taken. In doing so, the power is calculated at multiple different interval sizes to determine an adequate size at which the absorbed power converges. In this process, a trapezoidal numerical integration technique is used.

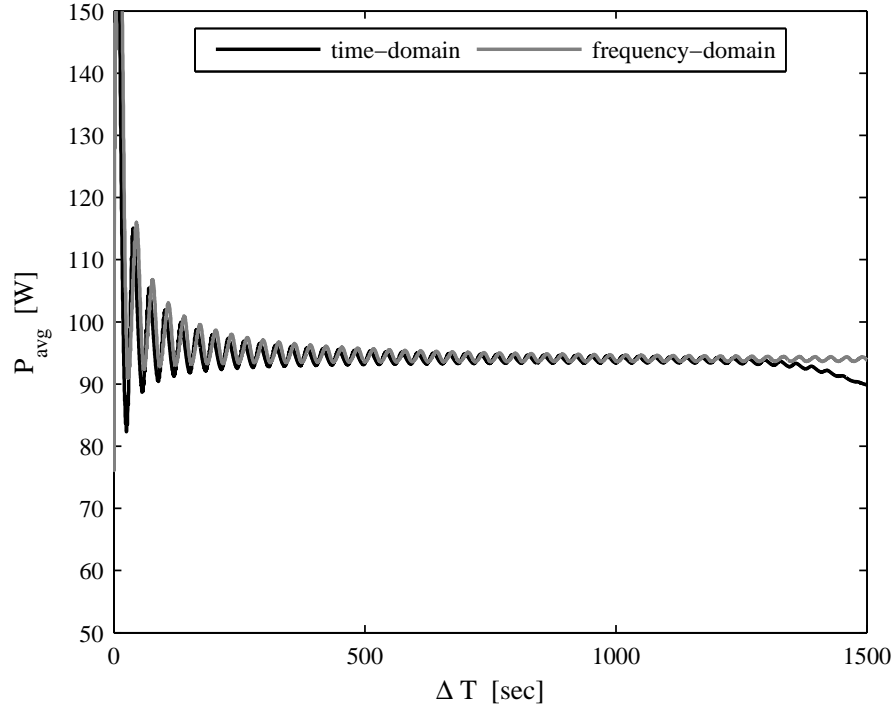


Figure 4.1: Convergence on a true average power. A numerically integrated average power for the time-domain’s motion response is shown in black, where the lower limit of the integration interval was extended from the end of the simulation to time zero. A series of definite integrals were carried out for the perturbation method simulation, where the upper-limit of integration was varied from time zero to the end of the time-motion response.

As shown in Figure 4.1, the average power absorbed by the linear viscous dashpot begins to converge on a average value with an integration interval greater than a thousand seconds. As shown, an insufficiently large interval could result in an inaccurate estimate of the absorbed power – the oscillatory motion exhibited in the convergence of the average absorbed power in can be attributed to an under- or over-estimate of the device’s full period. As the size of the time interval is increased, the portion of the response below or above an incomplete period becomes less significant, and the average absorbed power begins to converge. If the lower limit of the interval is extended too far, the integration begins to pick up the transient response, resulting in inaccurate estimate of the average power absorbed.

The approximation of the average absorbed power for the perturbation method solution components can be found using a similar technique. The solutions of the definite integrals found in Equations (4.10)-(4.12) require only the upper limit of integration to be set. If the upper limit is set to a sufficiently long time, the motion response between the float and spar are expected to have gone through a significant number of cycles, making the influence of a partially completed cycle become increasingly smaller. Shown in Figure 4.1, any upper limit of integration larger than 1000 seconds will provide a reasonably accurate approximation to the average absorbed power. Because the average absorbed power is a closed form expression, it does not require a time-series response. As a result, the upper-limit of integration can be set to a very long period of time to ensure the definite integral approaches the correct absorbed power at no additional computational cost.

The power absorption calculation is, however, heavily dependent on the number of levels used to approximate the motion response in the perturbation method. Continuing with the example problem of Section 2.5, the power absorption was evaluated using an upper-limit of integration of a thousand seconds at each of the levels used to provide the approximate motion response. As displayed in Figure 4.2, the perturbation method average power absorption approximation approaches the value found by the time-domain results in an exponentially decaying manner. This was found to be the case in all tests done where the periodically varying variable inertia unit had a non-negligible effect on the response of the system.

The result obtained by the perturbation method is quite similar to that of the value determined by the time-domain approximation. Because both of these values are approximations of the average absorbed power, one cannot say which is the true value. However, it is a good indication that the approximations are valid if their results are close in magnitude.

In the instance shown in Figure 4.2, the average power absorbed with the zeroth level alone, equivalent to a linearly controlled system, has a smaller absorbed power than the converged value over many levels. This suggests that the amount of power absorbed by the system is increasing as a result of the periodically varying effective mass for this particular scenario. This would suggest that there is indeed a benefit to periodically varying the effective mass in that particular scenario; however, the

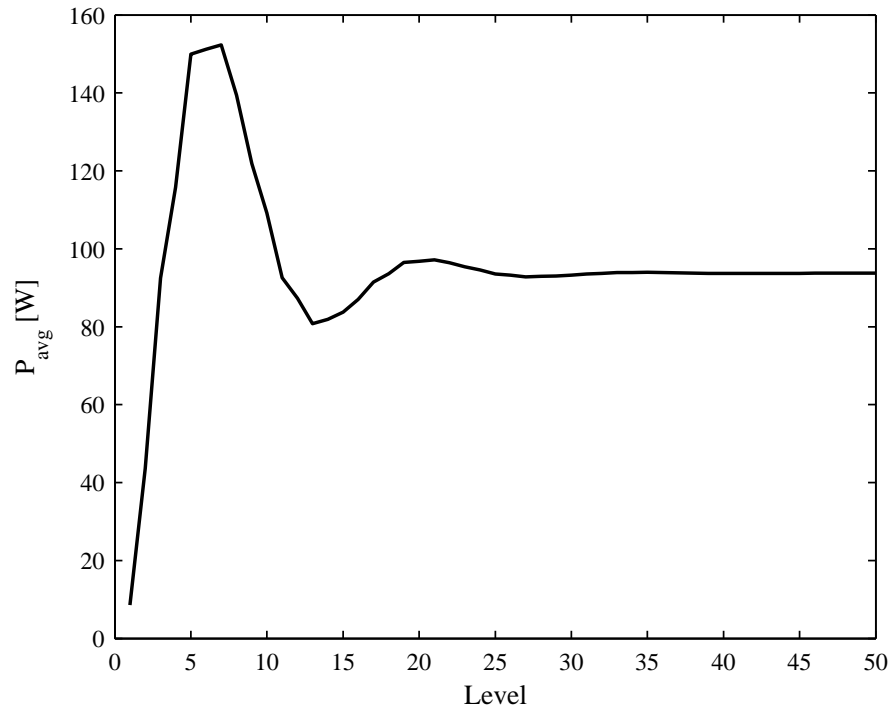


Figure 4.2: The number of levels required in the motion response to convergence on a true average power for the perturbation analysis. A series of definite integrals were carried out upon each level, where the upper-limit was set to a value of 1000 seconds.

power required to provide the inertial arms actuation associated with the variation in the effective mass may result in no net benefit. In Section 4.3 the average power associated with the inertial arm actuation is investigated.

4.3 Variable Effective-Mass Unit Kinematics & Energy Consumption

To this point, a methodology has been developed to evaluate both the motion response and the average absorbed power of three-body wave energy converter with a periodically varying effective mass term. To accurately analyze the net benefit associated with the addition of a periodically varying effective mass term, it is required to accurately quantify the energy consumed providing the effective mass variation.

In Section 4.3.1, a basic design concept for a variable effective-mass unit is presented. This design concept provides the foundation for a kinematic analysis, which, in turn, allows the calculation of consumed power to be completed. Although the analysis presented is specific to one particular design concept, the methodology used could be adapted for variations on that concept.

The kinematic analysis of the variable effective-mass unit presented in Section 4.3.2 provides a means to translate the device's motion response, $\underline{z}(t)$, and effective mass variation, $m_4(t)$, into a complete description of the inertial arm's radial motion. Section 4.3.3 provides a kinetic analysis to evaluate the instantaneous torque required actuate the inertial arms. Finally, in Section 4.3.4, the various ways in which the variation of effective mass could consume power are identified and measured for a particular case study.

4.3.1 Control System Design Concept

As described in Section 1.3.4, the SyncWave wave energy converter uses both variable power take-off damping and a variable effective-mass unit as control levers to tune the device. Up to this point, a particular wave form of the effective mass term has been prescribed without any concept of how the inertial arms of the device would actuate in time in order to provide this variation. In this section, a possible physical design of the variable effective-mass unit is provided.

The variable effective-mass unit design is subject to some physical constraints, as well as some parameters that have been previously specified by Beatty et al in [16]. Device parameters from this work, such as the maximum effective mass, ball screw

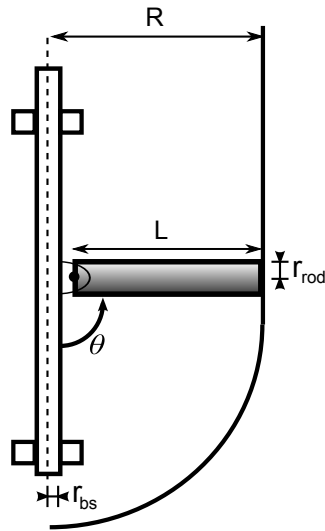


Figure 4.3: Variable effective-mass unit parameter design

lead, and spar hull radius, have been Froude scaled and presented in Table 1.1. Other device parameters have yet to be specified and will be derived for the design concept presented here.

The inertial arm(s) of the unit are assumed to rotate about a fixed pivot connected via a bracket to the ball screw. To allow the for a full 90° of rotation, the length of the inertial arm has been taken as the radius of the spar hull less the ball screw and inertial arm radii, Equation (4.13).

$$L = R - r_{bs} - r_{rod} \quad (4.13)$$

The elevation angle exhibited by the inertial arm is in accordance with the prescribed effective mass. A maximum inertia, or effective mass, that can be provided by the unit corresponds with a inertial arm elevation of 90° . If the scaled maximum effective mass of Table 1.1 is used, the maximum inertia required by the unit can be found by multiplying by the square of the ball screw's lead, l .

$$J_{max} = m_{max}l^2 \quad (4.14)$$

To determine the size and mass parameters of the inertial arm(s), a specific simple cross sectional shape is assumed. For this hypothetical design, it is assumed the shape of the inertial arm(s) is a slender cylindrical rod. In the position where the inertial arm is perpendicular to the ball screw's rotational axis, the mass of the rod required to achieve the maximum inertia value can be found according to Equation (4.16).

$$J_{max} = N_{arm} m_{rod} \left[\frac{L^2}{3} + (r_{bs} + r_{rod})^2 \right] \quad (4.15)$$

$$m_{rod} = \frac{m_{max} l^2}{N_{arm}} \frac{1}{\left[\frac{L^2}{3} + (r_{bs} + r_{rod})^2 \right]} \quad (4.16)$$

Where N_{arm} is the number of inertial arms, r_{bs} is the outer-most radius of the ball screw, and R is the radius of the spar hull. The mass of each rod can be related to the rod's radius, r_{rod} , by specifying a material density, ρ :

$$m_{rod} = \rho \pi (R - r_{bs}) r_{rod}^2 \quad (4.17)$$

Although any number of inertial arms are theoretically possible, practical implementation may not allow sufficient space for the rods to descend fully towards the ball screw (i.e. $\theta = 0$, Figure 4.4). For the purposes of this study, four equally sized inertial arms have been selected. To ensure that a practical implementation of the four inertial arms is possible, the following inequality must hold true:

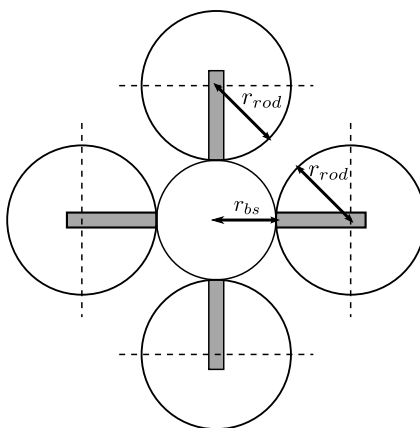


Figure 4.4: Top view of variable effective-mass unit with contracted inertial arms

$$r_{rod} < \frac{r_{bs}}{1 - \frac{1}{\sqrt{2}}} \quad (4.18)$$

This ensures that each inertial arm can expand and contract freely without contact with the other inertial arms. Lead was selected as the material of choice for the inertial arms for its high density. Equations (4.16) and (4.17) were used to evaluate the required radius of each inertial arm and the physical parameters defining the variable effective-mass unit are given in Table 4.1.

Table 4.1: Froude scaled variable effective-mass unit physical parameters.

Parameter	Model
Ballscrew	
Lead	$\left[\frac{\text{m}}{\text{rad}}\right]$ 0.006228
Radius	$[\text{m}]$ 0.013
Inertial Arm	
Length	$[\text{m}]$ 0.2636
Radius	$[\text{m}]$ 0.0234
Number	4
Effective Mass Control Range	
Lower Limit	$[\text{kg}]$ 850
Upper Limit	$[\text{kg}]$ 13000

The moment of inertia of each inertial arm can be found using an inertial arm fixed frame of reference located at the pinned point **A**, shown in Figure 4.6 for one arm. Each inertial arm is modeled as a slender rod rotating about its end. Equation (4.19)-(4.21) give the moments of inertia relative to that choice of reference point:

$$I_{xx} = \frac{m_{rod}L^2}{3} \quad (4.19)$$

$$I_{yy} = \frac{m_{rod}L^2}{3} \quad (4.20)$$

$$I_{zz} = \frac{m_{rod}r_{bs}^2}{2} \quad (4.21)$$

Each of these moments of inertia can then be rotated and shifted using the parallel axis theorem onto a fixed frame reference. The inertial arm angle, θ , can be repre-

sented as a function of the pre-prescribed desired change in effective mass through time, Figure 4.5. The effective mass at any angle can be shown to be:

$$m_4(t) = \frac{J}{l^2} \quad (4.22)$$

$$m_4(t) = \frac{I_{yy} \sin \theta(t) + I_{zz} \cos \theta(t) + m_{rod} r_{rb}^2}{l^2} \quad (4.23)$$

$$m_4(t) = \frac{I_{yy}(1 - \cos^2 \theta(t))^{1/2} + I_{zz} \cos \theta(t) + m_{rod} r_{rb}^2}{l^2} \quad (4.24)$$

Organizing Equation (4.24) in powers of $\cos \theta$ results in a quadratic function.

$$(I_{zz}^2 + I_{yy}^2) \cos^2 \theta(t) - 2(m_4(t)l^2 - m_{rod}r_{rb}^2)I_{zz} \cos \theta(t) + (m_4(t)l^2 - m_{rod}r_{rb}^2)^2 - I_{yy}^2 = 0 \quad (4.25)$$

Solving for θ results in four possible solutions, one in every quadrant, as would be expected.

$$\theta(t) = \cos^{-1} \left[\frac{2(m_4(t)l^2 - m_{rod}r_{rb}^2)I_{zz} \pm \sqrt{4(m_4(t)l^2 - m_{rod}r_{rb}^2)^2 I_{zz}^2 - 4(I_{zz}^2 + I_{yy}^2)((m_4(t)l^2 - m_{rod}r_{rb}^2)^2 - I_{yy}^2)}}{2(I_{zz}^2 + I_{yy}^2)} \right] \quad (4.26)$$

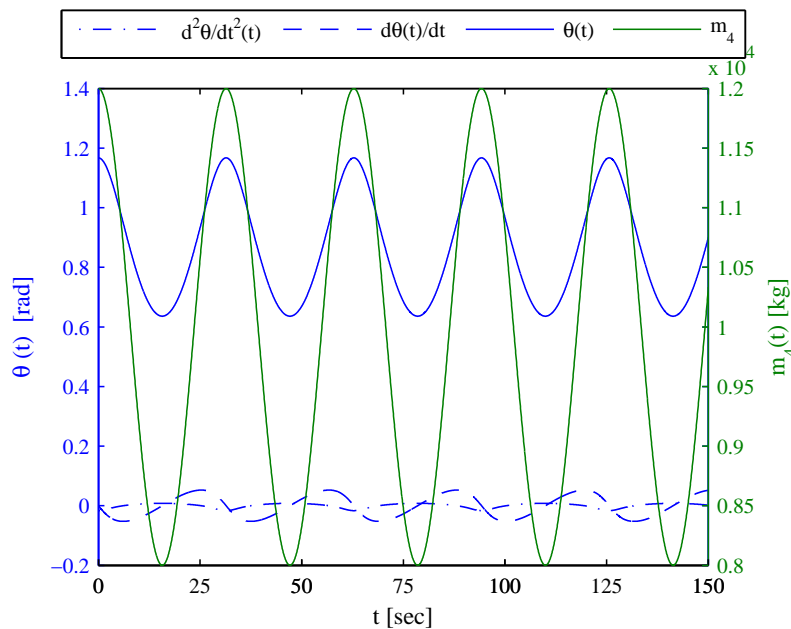


Figure 4.5: Inertial arm rotation angle as a function of the prescribed variation of the effective mass.

4.3.2 Variable Effective-Mass Unit Kinematics

The variable effective-mass unit has several degrees of freedoms, all oscillating with the motion of the spar. To determine an accurate measure of the energy required to actuate the effective mass in time, it is necessary to consider all of these motions that will have an effect on the torque required to adjust the rotational position of the inertial arm. In this analysis, two different coordinate systems will be used. These coordinate systems have been shown in Figure 4.6.

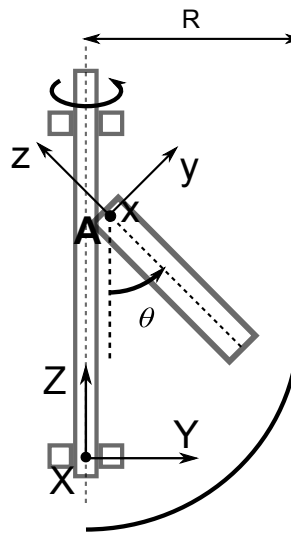


Figure 4.6: Coordinate systems for derivation of energy required to actuate the rotational position of the inertial arms. Note: in the orientation shown, both the \mathbf{x} and \mathbf{X} coordinates are pointing out of the page.

The angular velocity of the inertial arm about point \mathbf{A} on the device can be attributed to the change in rotational position of the inertial arm about its \mathbf{x} -axis and the angular velocity about the \mathbf{Z} -axis due to the rotational motion of the ball screw.

$$\vec{\omega}_A(t) = \Omega(t)\vec{K} + \dot{\theta}(t)\vec{i} \quad (4.27)$$

To add these terms together properly, it is required that the both terms be represented in the same coordinate system. Rotating the ball screw's angular velocity onto the inertial arm fixed frame:

$$\vec{\omega}_A(t) = \dot{\theta}(t)\vec{i} + \Omega(t) \sin \theta(t)\vec{j} + \Omega(t) \cos \theta(t)\vec{k} \quad (4.28)$$

Similarly, the angular acceleration of the inertial arm about point \mathbf{A} can be attributed to the change in rotational velocity of the inertial arm about the \mathbf{x} -axis, the change angular velocity about the \mathbf{Z} -axis due to the rotational motion of the ball screw, and the rotational velocity of the inertial arm multiplied by the change in the \mathbf{x} -axis through time resulting from the ball screw motion.

$$\frac{d\vec{\omega}_A(t)}{dt} = \vec{\alpha}_A(t) = \ddot{\theta}(t)\vec{i} + \dot{\Omega}(t)\vec{K} + \dot{\theta}(t)\vec{i} \quad (4.29)$$

The change in the \mathbf{x} -axis through time can be represented as the cross-product of the ball screws angular velocity and the \vec{i} unit vector.

$$\vec{\alpha}_A(t) = \ddot{\theta}(t)\vec{i} + \dot{\Omega}(t)\vec{K} + \dot{\theta}(t)(\Omega(t)\vec{K} \times \vec{i}) \quad (4.30)$$

All terms along the \mathbf{Z} -axis are then rotated onto the inertial arm fixed frame, resulting in the angular acceleration of the inertial arm about each axis of the body fixed frame given by Equation (4.31).

$$\vec{\alpha}_A(t) = \ddot{\theta}(t)\vec{i} + (\dot{\Omega}(t) \sin \theta(t) + \dot{\theta}(t)\Omega(t) \cos \theta(t))\vec{j} + (\dot{\Omega}(t) \cos \theta(t) - \dot{\theta}(t)\Omega(t) \sin \theta(t))\vec{k} \quad (4.31)$$

4.3.3 Variable Effective-Mass Unit Kinetics

Using Euler's three equations, the net torque about each axis of a rotating rigid body can be related to the moment of inertia tensor and the time-rate of change of the

angular momentum of the body, as in Equations (4.32)-(4.34). The net torque about the \mathbf{x} -axis can be attributed to the force due to gravitational effects and the force required to maintain the desired rotational position of the inertial arm. The torque about the other axes are the torques applied to the structural linkage. Although the second and third expression are useful in evaluating the structural strength required in designing the inertial arm linkages, it is the torque required to maintain the rotational position of the inertial arm about its \mathbf{x} -axis, τ_A , that is of particular interest.

$$\tau_x = \tau_A(t) - \frac{m_{rod}gL}{2} \sin \theta(t) = I_{xx} \frac{d\omega_x(t)}{dt} + (I_{zz} - I_{yy})\omega_y(t)\omega_z(t) \quad (4.32)$$

$$\tau_y = I_{yy} \frac{d\omega_y(t)}{dt} + (I_{xx} - I_{zz})\omega_z(t)\omega_x(t) \quad (4.33)$$

$$\tau_z = I_{zz} \frac{d\omega_z(t)}{dt} + (I_{yy} - I_{xx})\omega_x(t)\omega_y(t) \quad (4.34)$$

This form of Euler's equation only applies if the point \mathbf{A} , about which moments are taken, is stationary. The variable effective-mass unit is enclosed within the spar and, as a result, the entire unit will accelerate with the heave motion of the spar, \ddot{z}_s . This requires the addition of a $m_{rod}\vec{r}_{G/A} \times \vec{a}_A(t)$ term to the right hand side of Equation (4.32). Where $\vec{r}_{G/A}$ is the distance to the centre of mass relative to point \mathbf{A} and \vec{a}_A is the acceleration of the spar. For the orientation shown, this is half the length of the inertial arm along the \mathbf{z} -axis.

$$\tau_A(t) - \frac{m_{rod}gL}{2} \sin \theta(t) = -\frac{m_{rod}L}{2} \vec{k} \times \ddot{z}_s(t) \vec{K} + I_{xx} \frac{d\omega_x(t)}{dt} + (I_{zz} - I_{yy})\omega_y(t)\omega_z(t) \quad (4.35)$$

Solving for the required torque:

$$\tau_A(t) = \frac{m_{rod}gL}{2} \sin \theta(t) + \frac{m_{rod}L}{2} \ddot{z}_s(t) \sin \theta(t) I_{xx} \frac{d\omega_x(t)}{dt} + (I_{zz} - I_{yy})\omega_y(t)\omega_z(t) \quad (4.36)$$

The resultant torque required is a function of the inertial arm's position, angular velocity, angular acceleration, the heaving acceleration of the spar body, and moment of inertia tensors. The inertial arm's elevation, angular velocities, and acceleration – found using Equations (4.26), (4.28), and (4.31), respectively – can be substituted back into the required torque expression with a time series heave motion of the spar and evaluated using the methodology outlined in Section 3.1.2, to give an expression

of the torque required to maintain the inertial arm's radial position at any instant in time:

$$\tau_A(t) = \frac{m_{rod}(g + \ddot{z}_s(t))L}{2} \sin \theta(t) + I_{xx}\ddot{\theta}(t) + (I_{zz} - I_{yy})\Omega^2(t) \sin \theta(t) \cos \theta(t) \quad (4.37)$$

The angular velocity of the ball screw, $\Omega(t)$, is a result of the relative motion between the spar and reaction mass:

$$\Omega(t) = \frac{\dot{z}_s(t) - \dot{z}_r(t)}{l} \quad (4.38)$$

$$\tau_A(t) = \frac{m_{rod}(g + \ddot{z}_s(t))L}{2} \sin \theta(t) + I_{xx}\ddot{\theta}(t) + (I_{zz} - I_{yy}) \frac{(\dot{z}_s(t) - \dot{z}_r(t))^2}{l^2} \sin \theta(t) \cos \theta(t) \quad (4.39)$$

Substituting Equation (4.26) and its second derivative back into Equation (4.39) results in a torque expression that depends solely on the response of the spar, the reaction mass, and the variable effective-mass control parameters. Unfortunately, this substitution results in Equation (4.39) becoming heavily non-linear. Unlike the previous motion response analysis, the torque required to maintain the rotational position of the inertial arms can not be modeled as the super position of oscillatory components. Instead, the analysis requires a time-series response of the spar and reaction mass to evaluate the torque at every time-step. This does not nullify the benefit of the perturbation method, as the time-series response of these bodies can be produced from the perturbation method's components much quicker than a numerically integrated time-domain equivalent.

4.3.4 Variable Effective-Mass Unit Average Power Consumption

The instantaneous power required to maintain the inertial arms path of motion at any given moment can then be evaluated by multiplying the instantaneous torque by the rotational velocity of the inertial arm about point **A**, Equation (4.40).

$$P_1(t) = \tau_A(t)\dot{\theta}(t) \quad (4.40)$$

This model assumes that if the torque required to maintain the inertial arms' position is positive and the angular velocity of the inertial arm is negative, or vice

versa, that the device is capable of absorbing energy. Depending on the electromechanical device design, this may not be true. Two other scenarios are presented as possibilities. First, the device is not capable of absorbing energy during braking and it is assumed to be lost.

$$P_2(t) = \begin{cases} \tau_A(t)\dot{\theta}(t) & \tau_A(t)\dot{\theta}(t) \geq 0 \\ 0 & \tau_A(t)\dot{\theta}(t) < 0 \end{cases} \quad (4.41)$$

Second, the system can not be back-driven and, as a result, instead of absorbing that power, the unit is required to input the power to adjust the inertial arms.

$$P_3(t) = |\tau_A(t)\dot{\theta}(t)| \quad (4.42)$$

A plot showing the instantaneous torque and the three different instantaneous power scenarios through time is given for the case study used through the duration of this thesis in Figure 4.7.

To determine an appropriate measure of average power required to actuate the inertial arms, it is required to take the mean instantaneous power over its period. The average power to actuate the inertial arms is not solely dependent on the rotation of the inertial arm in time, but also the motion of the spar and the relative motion between the spar and reaction mass. As a result, a closed form expression for the instantaneous power's period is not easily found. To approximate the true average power, the time series over which the instantaneous power is evaluated is extended in time and the mean is taken of its values. Given a sufficiently long time series, the effect of an additional partial cycle on the overall mean will become negligible. A plot showing the convergence to a true average power for each of the actuation power scenarios discussed above has been displayed in Figure 4.8.

The average net power absorbed by the device can then be evaluated as the average actuation power subtracted from the gross average power absorbed by the power take-off unit given in Section 4.1.

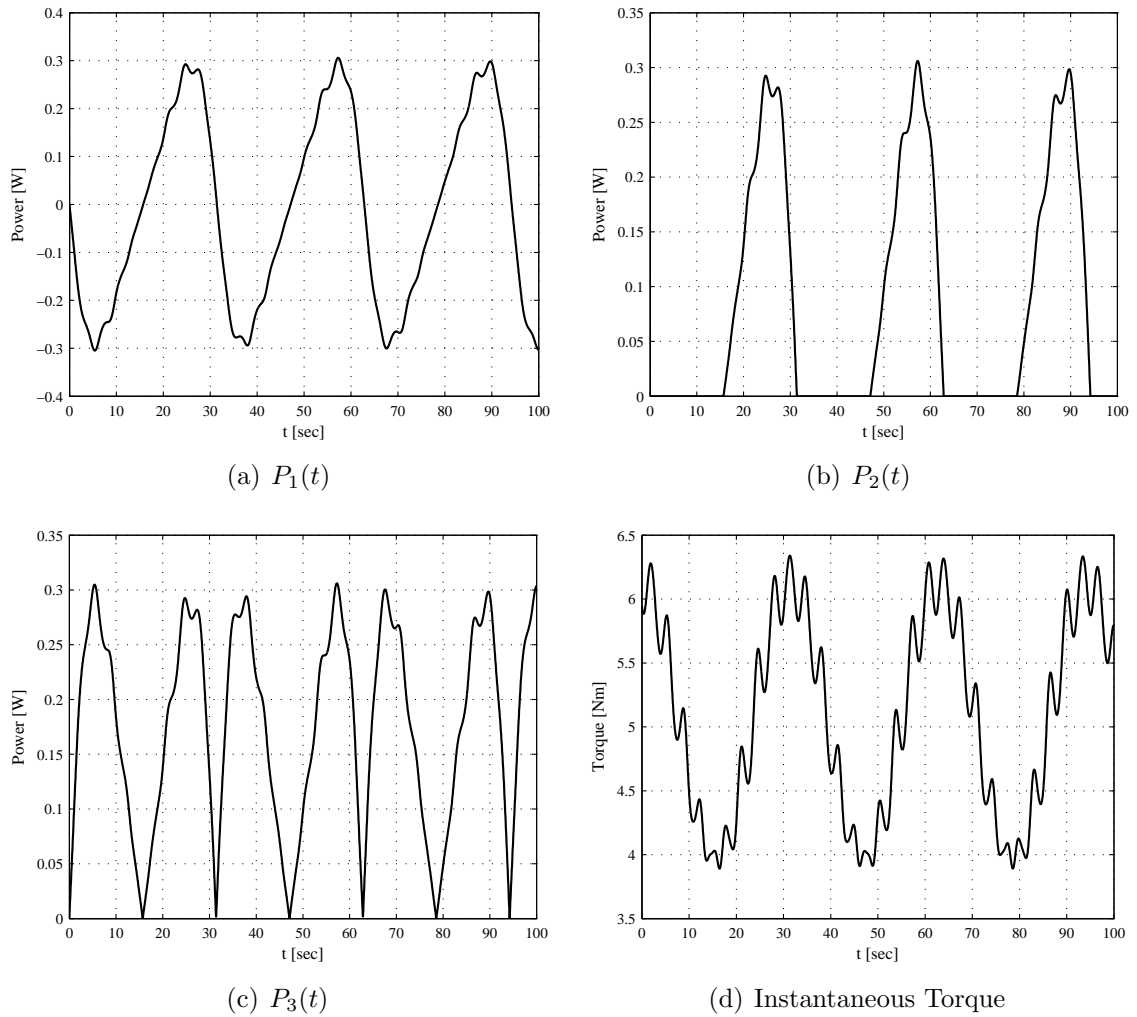


Figure 4.7: Instantaneous torque and power requirements of the variable effective-mass unit for the case study parameters given in Table 2.1. Three different power requirement scenarios are given according to possible physical designs.

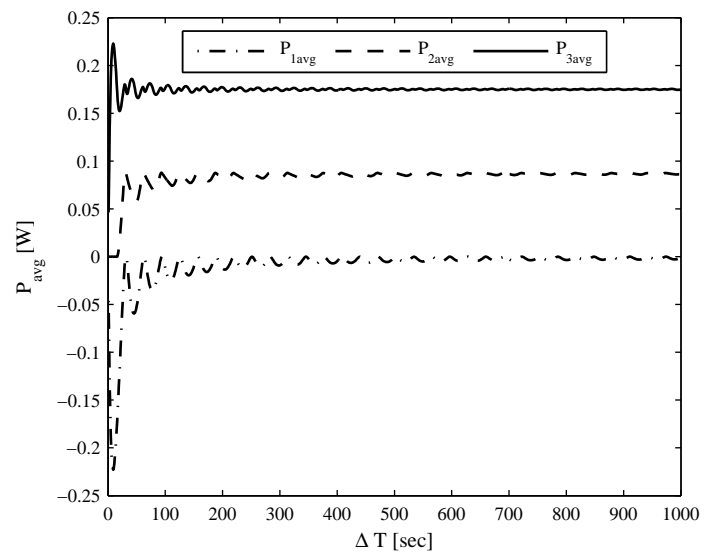


Figure 4.8: Convergence on average power required to accurate inertial arms for three different implementation cases.

Chapter 5

Conclusions & Future Work

5.1 Main Findings

The work presented in this thesis has provided a new means of evaluating the response of a WEC device subject to regular wave forcing and a periodically varied intrinsic physical parameter. The methodology developed provides the response as a closed-form expression using a perturbation method based approach. This technique stretches the commonly accepted bounds of WEC frequency-domain analysis methods and is of much practical importance in the evaluation of control techniques in the field of WEC technology.

Prior to this work, the analysis of a WEC's time-varying physical control parameters was strictly limited to the use of time-domain numerical integration. The work presented in this thesis provides a new computationally efficient means of analyzing the response of these devices and provides all the necessary components required for a design optimization. This allows for any point absorbing WEC with unique device geometry and/or control parameters to be refined at the conceptual level in a computationally efficient manner. A potential optimization process, using the functions provided in this thesis, is presented below in Figure 5.1.

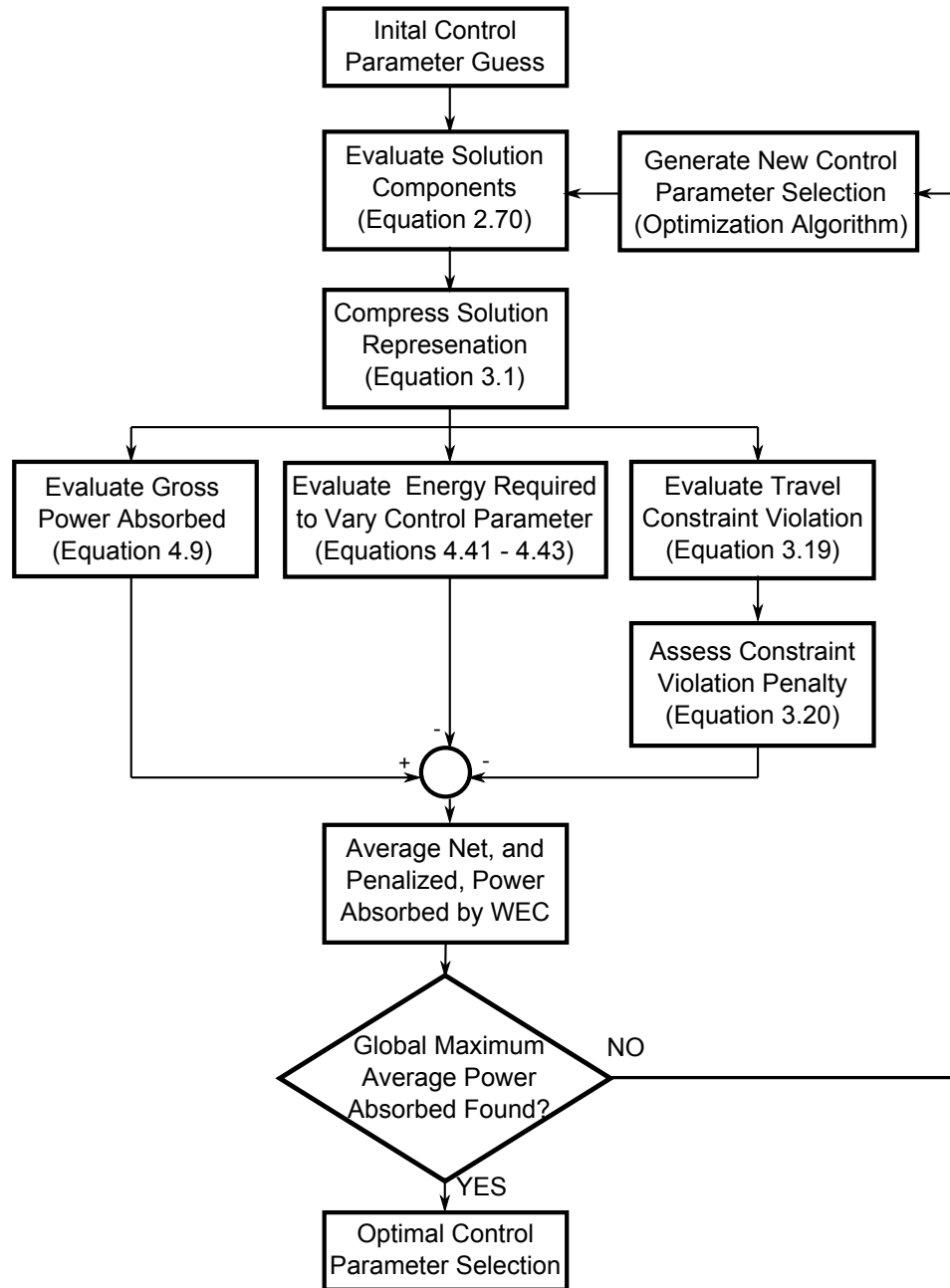


Figure 5.1: A flowchart depicting a potential automated optimization routine using the functions provided in this thesis.

For the developed methodology to have an advantage over existing techniques, the computational speed and memory required to evaluate the device's response must be comparable, or better, than that of traditional numerical integration analysis. This objective was achieved by providing a closed-form expression to evaluate the device's response in the frequency-domain. This closed-form solution provides a robust and concise description of the WEC motion. After ensuring the closed-form solution was accurate, as demonstrated in Figure 2.6, and applying essential time-saving techniques, it was found that the developed methodology does drastically reduce both computational time and memory required to evaluate the device's steady-state response, Table 3.1.

The perturbation based approach allows for the bodies response to be represented in a finite set of solution components, each defined by a complex amplitude and frequency, rather than a time-series containing hundreds or thousands of states as required in conventional techniques. This solution representation was used to create a closed form expression to determine the likelihood that resulting relative motion between bodies of the WEC exceed a given height limit. This expression was used to assess the probability that a WEC's physical travel constraints would be violated for a given regular input and control parameter variation. The method provides a much more computationally efficient means of evaluating constraint violations than a time-series based approach. In addition, it is easily adjusted to reflect a WEC designers confidence in the mechanical and electrical devices that manage end-stop collisions.

To quantitatively compare the desirability of a particular design iteration, a means to translate the steady-state motion response information into an estimate of the device's average gross absorbed power was developed. This calculation is consistent with existing frequency-domain approaches in that it provides an closed form expression that does not require processing time series data to evaluate gross power. To determine the average net-power absorbed by the WEC an estimate of the energy required to actuate the effective-mass term was created by considering a conceptual design for the effective mass device. Unfortunately, due to the nature of the problem, this expression requires the use of a time-series motion response to determine the energy required. However, the creation of a time-series motion response with the developed perturbation method is quite computationally efficient and the process of evaluating the net-power in this manner, rather than with a numerically integrated

approach, is still computationally advantageous.

The closed form nature of the device's motion response given by the perturbation method, as well as the closed form expressions used to characterize the device's response for the gross absorbed power and constraint violation metrics, bring a great deal of benefit to development process of a device's control technique design. The closed form representation facilitates direction calculation of response, constraint violation, and power absorbed.

In terms of time savings, consider the following factors that determine the computational time required for a global optimization technique, a particle swarm algorithm, to converge on an optimal effective mass variation waveform:

- The number of initial particles, $m_4(t)$ parameter sets, would be around 100.
- 1000 iterations of the particle swarm optimization routine would be required to drive each particle toward a global maximum of the device's average absorbed power.
- As such, for 100 initial particles, 100,000 total control parameter design iterations could be required.
- Considering the more than 7 second advantage of the proposed perturbation methodology over a time-domain analysis, there is a 700,000 time savings that could, considerably, be seen. In addition, the time required to post-process the time-series information to provide gross absorbed power and constraint violation metrics, would add to the savings realized.
- The 700,000 seconds of computational time translates to roughly 8 days of waiting time for the human designer. Using the perturbation method outlined in this work, roughly 4 hours would be needed to determine the optimal control parameter variation for a single regular wave.
- If the technique is extended to irregular eas, several (8-16) regular waves would have to be considered further exacerbating the time difference between the two approaches.

With these results, the work presented in this thesis has provided all the necessary required elements for a design optimization routine; a means to evaluate the motion response of a device, the net energy absorbed by the device, and the ability to assess constraint violations. The functions created have drastically reduced the computational time required to evaluate a potential design iteration and provide an advantageous alternative to traditional WEC analysis techniques. However, to expand the range of control circumstances that can be investigated, there are additional steps that need to be taken. These additional steps are outlined in the Section 5.2.

5.2 Future Work

5.2.1 Stability Analysis

The case study control parameter setting used throughout this thesis, given in Table 2.1, is only one of an infinite number of generator damping and variable effective mass pairings. Other control parameter settings have been tested and were found to converge on the appropriate solution. Unfortunately, some settings resulted in an unstable response evaluation and were unable to converge on the appropriate solution.

To demonstrate this instability and discuss the causes of it, two solution evaluation scenarios are given; one remains stable, while the other demonstrates an unstable solution process. The first scenario, is that of the case study considered throughout the thesis and described in Table 2.1. The second, and unstable, scenario uses a similar set of parameters as the stable case study, but with a larger effective mass variation amplitude, ϵ_1 . The complete parameter set for the unstable second scenario is given in Table 5.1.

Although the two scenarios have similar control parameter settings, the response evaluation produces two very different results. The component construction of the reaction mass response has been given for the first eight levels of the solution for both scenarios in Figures 5.2 and 5.3. Also included in these figures are the reaction mass' response amplitude operator (RAO), Equation (3.7), plotted over the compressed representation of each scenario's solution - constructed from the components $\vec{\zeta}(\omega_j)$

Table 5.1: Wave and physical control parameters used to demonstrate an unstable response evaluation case.

Parameter	Name	Units	Value
H_s	Significant Wave Height	[m]	0.4
ω_i	Incident Wave Frequency	$\frac{\text{rad}}{\text{s}}$	1.725
c_g	Generator Damping	$\frac{\text{Ns}}{\text{m}}$	3000
ϵ_0	Effective Mass Bias	[kg]	10000
ϵ_1	Effective Mass Amplitude	[kg]	3000
ϕ_1	Effective Mass Phase	[rad]	0
ω_c	Effective Mass Control Frequency	$\frac{\text{rad}}{\text{s}}$	0.2

As shown in Figure 5.3, the components of the unstable evaluation process continually grow at each successive level. The growth of these components appears to originate at the component with a oscillation frequency of $\omega_j = 1.725 \frac{\text{rad}}{\text{s}}$, which then begins to affect the growth of neighbouring components. In the stable solution, Figures 5.2, this trait is not seen and the solution component magnitudes continually decrease upon each successive level.

The instability of the second case is best explained using the device's response amplitude operator(RAO), first introduced in Section 3.2 in Equation (3.7). It is first noted that the RAO for the unstable scenario is significantly higher than the stable solution's RAO. This is a result of the direct relationship between the RAO and the effective mass variation amplitude, ϵ_1 , Equation (3.7). This effects the peak value of the RAO and also scales the magnitude of the RAO at any frequency. The construction of the solution, as described in Section 2.4.2, is a recursive pattern in which each level's solution amplitude provides a portion of the forcing applied to the two neighbouring components on the succeeding level's equations of motion. The RAO acts as a transfer function between the solution components at each level and, as a result, if the product of two neighbouring component's RAO value is greater than unity, the magnitude of the preceding level's component will grow rather than decay and will result in the solution response becoming unstable.

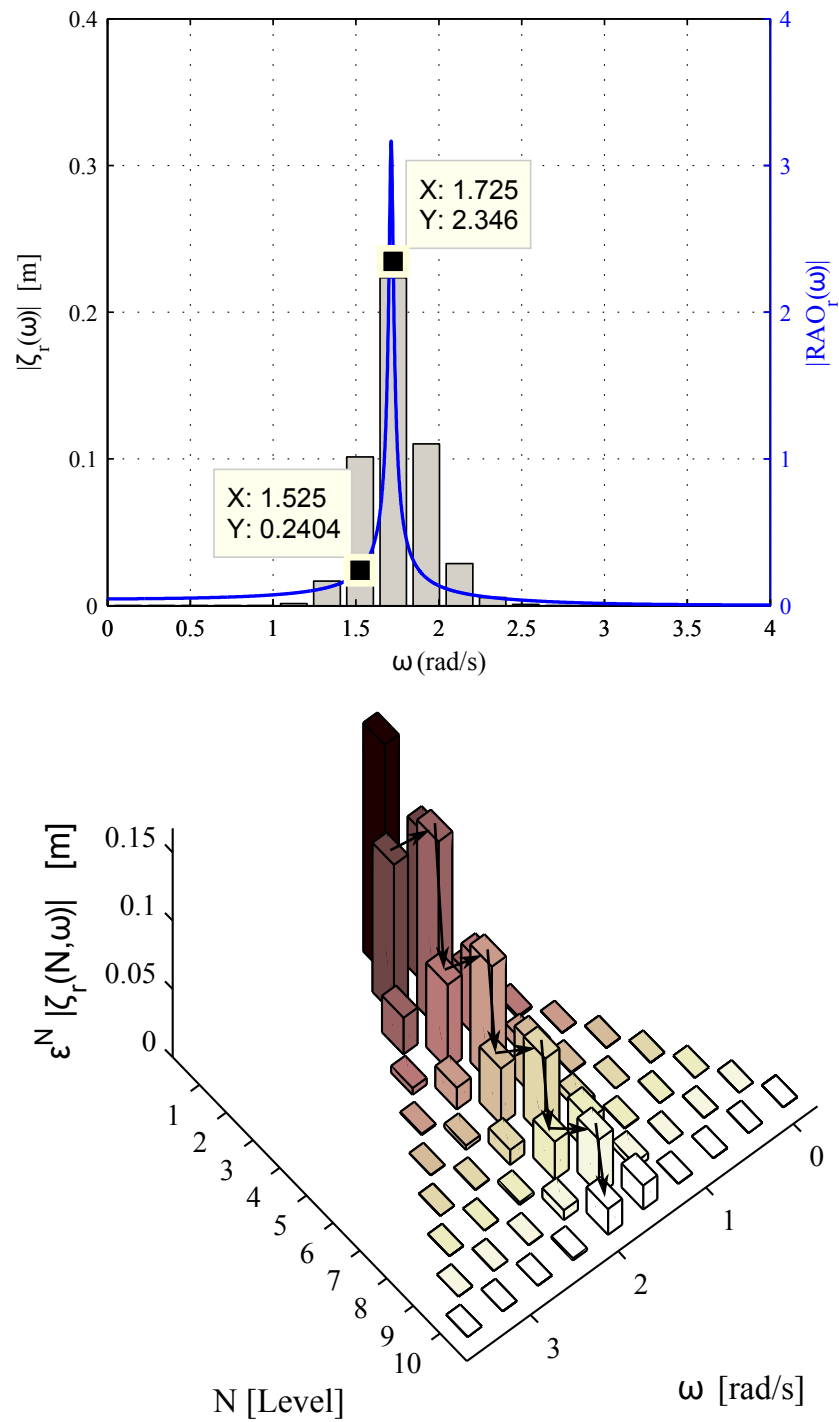


Figure 5.2: A stable perturbation approach solution evaluation. Physical parameters for this simulation are given in Table 2.1

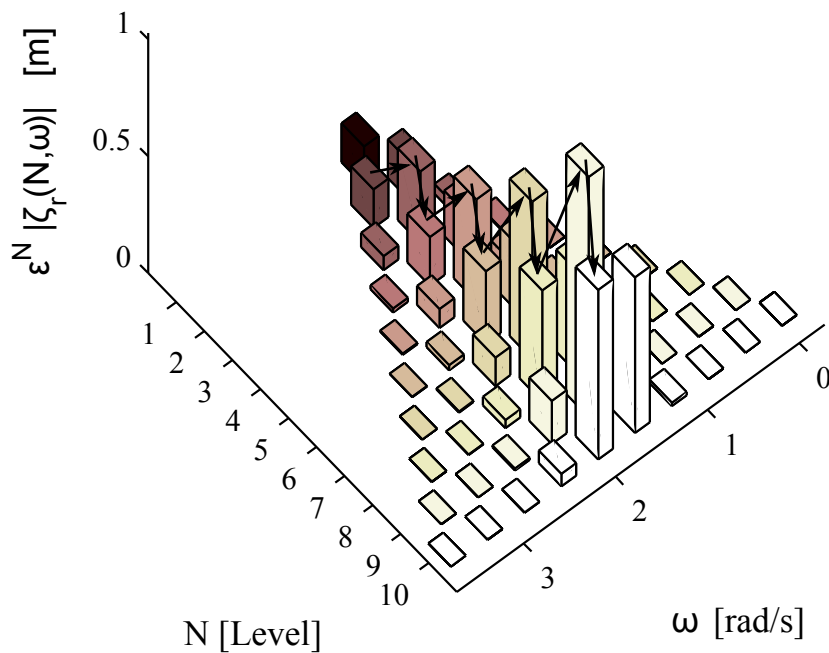
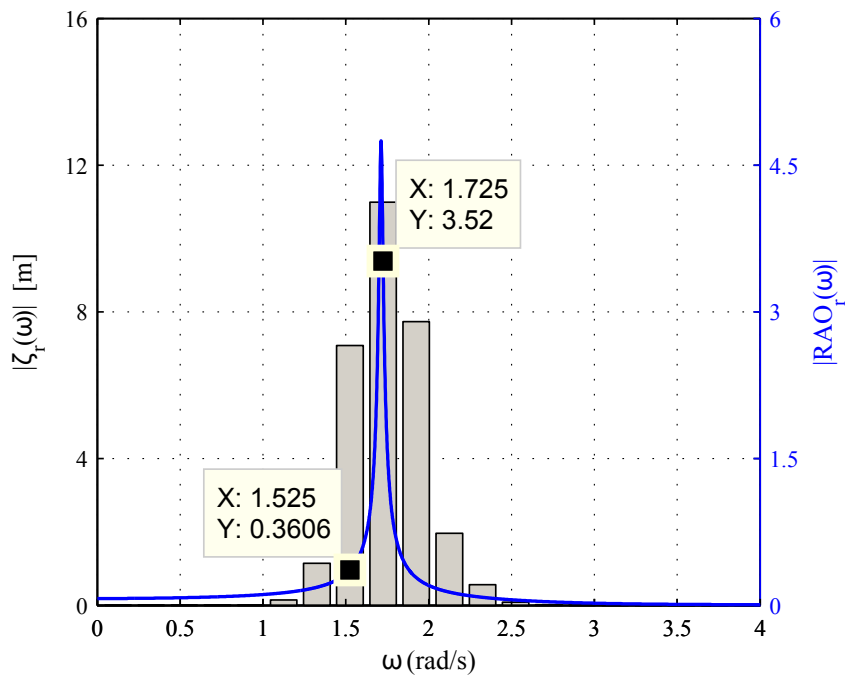


Figure 5.3: An unstable perturbation approach solution evaluation. Physical parameters for this simulation are given in Table 5.1. Note that the vertical axis' scale for both plots is quite different from the corresponding plots in Figure 5.2.

For example, consider the evaluation of component $\omega = 1.725 \frac{rad}{s}$ in the unstable scenario shown in Figure 5.3. For a given input component motion, the output motion grows by a factor of 3.52. This new term will drive the input of a successive level at a frequency of $1.725 \frac{rad}{s} - \omega_c = 1.525 \frac{rad}{s}$. The RAO plot of Figure 5.3 shows that this component will be 36.1% of its input. This output will then provide an input for a component back at $\omega = 1.725 \frac{rad}{s}$ ($\omega = 1.725 \frac{rad}{s} - \omega_c + \omega_c$). At that stage the original component has grown by 352% and then contracted by 63.9% leaving an input that is 127% of the original component. This then repeats across the next levels. In the stable case, the product of neighbouring RAO values, at $\omega = 1.725 \frac{rad}{s}$ and $\omega = 1.525 \frac{rad}{s}$, is less than unity and a stable evaluation process results.

It is important to note that the effective mass variation parameter does not effect the shape of the RAO - it is only responsible for its magnitude. On the other hand, the remaining two control parameters, generator damping c_g and the effective mass bias ϵ_0 , greatly effect the shape of the RAO. Figure 5.4 shows how the selection of generator damping can change not only the peak magnitude of the reaction mass' RAO, but also the shape.

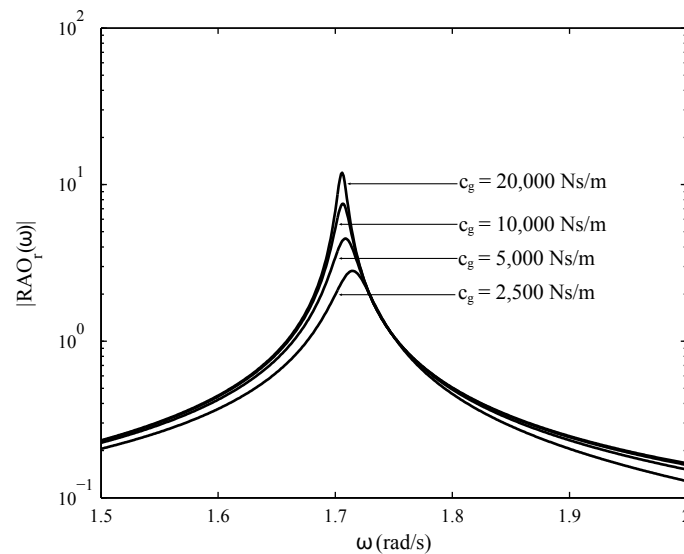


Figure 5.4: RAO shape changes with varied generator damping. Other physical parameters can be found in Table 5.1.

It is believed that these high RAO values are, in part, due to an improper representation of the added mass, the radiation damping, and an unrealistically low value

of damping on the reaction mass. As discussed Section 2.2, a constant coefficient model was adopted. This model does not take into the frequency dependence of the added mass and radiation damping parameters. The frequency dependence of these terms, as well as a higher level of damping on the reaction mass, is expected to result in peak reductions on the RAO and possibly limit the domain of c_g , ϵ_0 , and ϵ_1 combinations that lead to instability. As shown in Figure 5.5, the unreasonably low reaction mass damping coefficient of $10 \frac{Ns}{m}$ is largely responsible for the high RAO values and consequently, the unstable nature of the solution. At this point no industrial design exists for the effective mass system, and the true value of the damping remains speculative.

The travel constraint analysis presented in Section 3.3 is capable of assessing a penalty or disregarding solutions that do go unstable. However, the current dynamics model is believed to be too restrictive and would eliminate, on an artificial concern, a great deal of potential control strategies. Further work is needed to determine the appropriate values of reaction mass damping, as well as the frequency dependent added mass and damping coefficients.

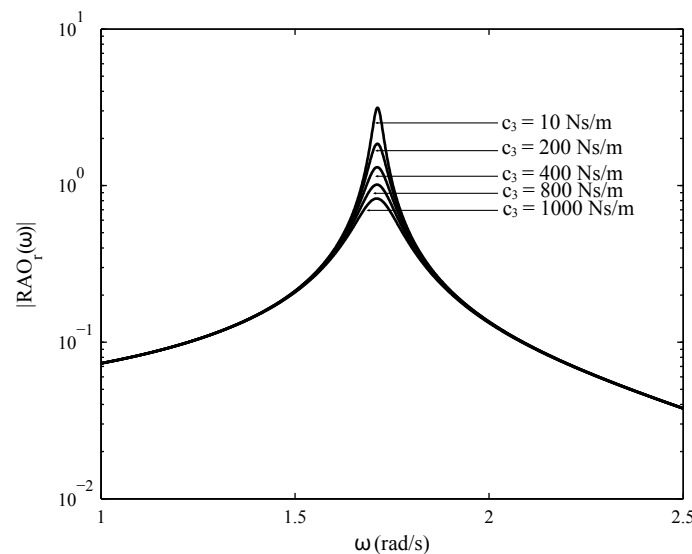


Figure 5.5: RAO shape changes with varied reaction mass damping. Other physical parameters can be found in Table 5.1.

5.2.2 Perturbation Methodology Extension

The effective mass variation described in Section 2.3, used throughout the work presented in this thesis, was limited to a two-term Fourier series. Although, this variation extends upon the time-invariant control parameter studies done on the SyncWave device in [9] and [16], the variation wave form is still quite limited. To converge on the optimal effective mass variation wave form, more Fourier series components describing the wave form must be added, allowing for a wider range of possible wave forms to be generated by the Fourier series included within an optimization routine. In Appendix A, the means to evaluate the response of the device for a three-term Fourier series is given to demonstrate the ability of the perturbation method to be extended. Future work is needed to further extend the perturbation method to a larger Fourier series and to evaluate the extended perturbation method's important device response characteristics; average absorbed power, net absorbed power, and travel constraint violation.

Appendix A

Methodology Extension to a Three Term Control Input

The methodology developed in Chapter 2 allowed for the response of a WEC with a periodically varying physical parameter to be evaluated. To allow for methodology development, the wave-form of the periodically varied parameter was limited to the first two terms of a Fourier series—a single sinusoidal wave with a bias, as described in Section 2.3.

Although the truncated Fourier series allowed for methodology development, the absorbed power benefit resulted from the truncated series is limited. As it stands, it remains unknown as to the type of parameter variation that will allow for maximum energy absorption for the device. As to not limit the possible wave-forms that can be analyzed with the methodology developed, it is desired that variation of the physical parameter be extended to the first three terms of the Fourier series. Although the number of terms in the Fourier series is still relatively small, this process will show that the methodology developed to handle the two-term series is capable of being extended.

$$m_4(t) = \epsilon_0 + \epsilon_1 [e^{i(\omega_c t + \phi_1)} + e^{-i(\omega_c t + \phi_1)}] + \epsilon_2 [e^{i(2\omega_c t + \phi_2)} + e^{-i(2\omega_c t + \phi_2)}] \quad (\text{A.1})$$

In extending the effective mass variation to a three-term Fourier series, only two new control parameters are introduced; an amplitude term of ϵ_2 and a phase off-set of ϕ_2 . By adding this additional term, the matrix form of the mass and damping matrices of Equations (2.11) and (2.12) will need to be adjusted:

$$\begin{aligned} \mathbf{M} &= \mathbf{M}_L + \frac{\epsilon_1}{2} \mathbf{Q} [e^{i(\omega_c t + \phi_1)} + e^{-i(\omega_c t + \phi_1)}] \\ &+ \frac{\epsilon_2}{2} \mathbf{Q} [e^{i(2\omega_c t + \phi_2)} + e^{-i(2\omega_c t + \phi_2)}] \end{aligned} \quad (\text{A.2})$$

$$\begin{aligned} \mathbf{C} &= \mathbf{C}_L + i\omega_c \frac{\epsilon_1}{2} \mathbf{Q} [e^{i(\omega_c t + \phi_1)} - e^{-i(\omega_c t + \phi_1)}] \\ &+ i2\omega_c \frac{\epsilon_2}{2} \mathbf{Q} [e^{i(2\omega_c t + \phi_2)} - e^{-i(2\omega_c t + \phi_2)}] \end{aligned} \quad (\text{A.3})$$

As shown, the linear portion of the mass and damping matrices remains unchanged, but there is an additional non-linear term added. This added non-linear term found in the mass and damping matrices will result in the presence of additional forcing functions and solution components. To properly account for this change, the assumed form of the solution for the perturbation method must be adjusted:

$$\underline{z}(t) = \underline{z}_0(t) + \epsilon_1 \underline{z}_1(t) + \epsilon_2 \underline{z}_2(t) + \epsilon_1^2 \underline{z}_3(t) + \epsilon_1 \epsilon_2 \underline{z}_4(t) + \epsilon_2^2 \underline{z}_5(t) + \dots \quad (\text{A.4})$$

Substituting both the extended mass and damping matrices, Equations (A.2) and (A.3), and the assumed form of the solution back into the device's equation of motion, Equation (2.9), gives:

$$\begin{aligned} \underline{f}_e(t) &= \mathbf{M}_L [\ddot{\underline{z}}_0(t) + \epsilon_1^1 \ddot{\underline{z}}_1(t) + \epsilon_2^1 \ddot{\underline{z}}_2(t) + \dots] + \mathbf{C}_L [\dot{\underline{z}}_0(t) + \epsilon_1^1 \dot{\underline{z}}_1(t) + \epsilon_2^1 \dot{\underline{z}}_2(t) + \dots] + \mathbf{K}_L [\underline{z}_0(t) + \epsilon_1^1 \underline{z}_1(t) + \epsilon_2^1 \underline{z}_2(t) + \dots] \\ &- \frac{\epsilon_1}{2} \mathbf{Q} [e^{i(\omega_c t + \phi_1)} + e^{-i(\omega_c t + \phi_1)}] [\ddot{\underline{z}}_0(t) + \epsilon_1^1 \ddot{\underline{z}}_1(t) + \epsilon_2^1 \ddot{\underline{z}}_2(t) + \dots] \\ &- i\omega_c \frac{\epsilon_1}{2} \mathbf{Q} [e^{i(\omega_c t + \phi_1)} - e^{-i(\omega_c t + \phi_1)}] [\dot{\underline{z}}_0(t) + \epsilon_1^1 \dot{\underline{z}}_1(t) + \epsilon_2^1 \dot{\underline{z}}_2(t) + \dots] \\ &- \frac{\epsilon_2}{2} \mathbf{Q} [e^{i(2\omega_c t + \phi_2)} + e^{-i(2\omega_c t + \phi_2)}] [\ddot{\underline{z}}_0(t) + \epsilon_1^1 \ddot{\underline{z}}_1(t) + \epsilon_2^1 \ddot{\underline{z}}_2(t) + \dots] \\ &- i2\omega_c \frac{\epsilon_2}{2} \mathbf{Q} [e^{i(2\omega_c t + \phi_2)} - e^{-i(2\omega_c t + \phi_2)}] [\dot{\underline{z}}_0(t) + \epsilon_1^1 \dot{\underline{z}}_1(t) + \epsilon_2^1 \dot{\underline{z}}_2(t) + \dots] \end{aligned} \quad (\text{A.5})$$

Expanding the newly defined equation of motion and collecting in terms of common ϵ_i 's, including mixed products, one obtains an infinite series of coupled ordinary differential equations that present as one degree of freedom oscillators:

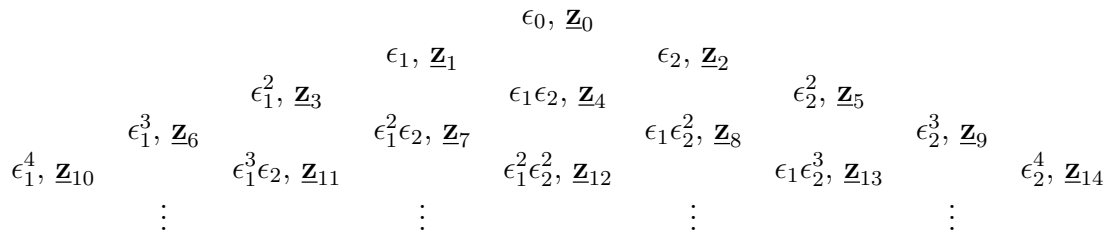


Figure A.1: Pascal’s pyramid for complete polynomials. The solution components have been ordered in such a way that they can be solved sequentially.

parameter is indeed possible with some slight modifications to the evaluation ordering and memory storage. Further added terms to the Fourier series representation will again result in the addition of another dimension to the multinomial expansion (i.e. a three-term Fourier series representation results in the binomial construct of Pascal’s triangle, four-term representation results in a trinomial construct of Pascal’s tetrahedron, etc.). This results in a need for large number of component evaluations and novel approach to memory storage that is beyond the scope of this work.

Bibliography

- [1] J. Cruz. *Ocean Wave Energy*. Number 1865-3529 in Green Energy and Technology(Virtual Series). Springer Berlin Heidelberg, 2008.
- [2] S. J. Beatty, C. Hiles, R. S. Nicoll, J. E. Adamson, and B. J. Buckham. Design synthesis of a wave energy converter. In *Proceedings of the International Conference on Offshore Mechanics and Arctic Engineering - OMAE*, Honolulu, Hawai'i, 2009. OMAE, American Society of Mechanical Engineers.
- [3] G. A. Nolan, J. V. Ringwood, W. E. Leithead, and S. Butler. Optimal damping profiles for a heaving buoy wave energy converter. *15th International Offshore and Polar Engineering Conference, ISOPE-2005, Jun 19-24 2005*, 2005:477–484, 2005.
- [4] C. Hiles, B. Buckham, and P. Wild. Wave energy resources in hesquiaht sound. In *Proceedings of the Canadian Society for Mechanical Engineering Forum*, 2010.
- [5] S. J. Beatty. Analysis and developement of a three body heaving wave energy converter. Master's thesis, The University of Victoria, 2009.
- [6] R. Johansen. Ocean power. Patent No. US 508320, November 1893.
- [7] F. Dempsey. Wave motor. Patent No. US 819006, April 1906.
- [8] U. A. Korde. Control system applications in wave energy conversion. In *OCEANS 2000 MTS/IEEE Conference and Exhibition. Conference Proceedings (Cat. No.00CH37158)*, volume vol.3, pages 1817–24, Piscataway, NJ, USA, 2000. IEEE.
- [9] J. Falnes. Optimum control of oscillation of wave-energy converters, 1993. “Annex Report B1: Device fundamentals/Hydrodynamics”, an annex to the main

report “Wave Energy Converters: Generic Technical Evaluation Study”, the final report for the B-study of the DG XII Joule Wave Energy Initiative.

- [10] A.A.E. Price, C.J. Dent, and A.R. Wallace. Frequency domain techniques for numerical and experimental modelling of wave energy converters. In *Proceedings of the 8th European Wave and Tidal Energy Conference EWTEC*, 2009.
- [11] E. R. Laithwaite and S. H. Salter. Method of, and apparatus for, extracting energy from waves, November 1981.
- [12] J. Falnes. Wave-energy conversion through relative motion between two single-mode oscillating bodies. *Journal of Offshore Mechanics and Arctic Engineering*, 121(1):32–38, 1999.
- [13] S. Beatty. Sensitivity of point absorbing wecs to physical parameters of the reacting body. In *In proceedings of the 9th European Wave and Tidal Conf*, Southampton, UK, September 2011.
- [14] D. Dunnett and James S. Wallace. Electricity generation from wave power in canada. *Renewable Energy (2008)*, 2008. In Press.
- [15] A. P. McCabe and G. A. Aggidis. Optimum mean power output of a point-absorber wave energy converter in irregular waves. *Proceedings of the Institution of Mechanical Engineers, Part A: Journal of Power and Energy*, 223(7):773–781, 2009.
- [16] J.K.H. Shek. Reaction force control of a linear electrical generator for direct drive wave energy conversion, 2007.
- [17] T.K.A. Brekken. On model predictive control for a point absorber wave energy converter. In *PowerTech, 2011 IEEE Trondheim*, pages 1–8, june 2011.
- [18] J. Falnes. *Ocean Waves and Oscillating Systems: Linear Interactions including Wave Energy Extraction*. Cambridge University Press, 2002.
- [19] R.G. Dean and R.A. Dalrymple. *Water wave mechanics for engineers and scientists*, volume 2 of *Advanced series on ocean engineering*. World Scientific, 1991.
- [20] G. B. Airy. Tides and waves. In Et Al, editor, *Encyclopedia metropolitana (1817–1845)*. London, 1841.

- [21] A. Babarit, M. Guglielmi, and A. H. Clement. Declutching control of a wave energy converter. *Ocean Engineering*, 36(12-13):1015 – 1024, 2009.
- [22] W. E. Cummins. The impulse response function and ship motions. *Schiffstechnik*, 9(1661):101–109, 1962.
- [23] M. Greenhow, J. H. Rosen, and M. Reed. Control strategies for the clam wave energy device. *Applied Ocean Research*, 6(4):197 – 206, 1984.
- [24] K. Budal and J. Falnes. A resonant point absorber of ocean-wave power. *Nature*, 256:478 – 479, 1975.
- [25] G.A. Nolan, J.V. Ringwood, W.E. Leithead, and S.H. Salter. Power conversion systems for ducks. In *Proceedings of International Conference on Future Energy Concepts*, number 171, pages 100–108, London, January 1979. Institution of Electrical Engineers.
- [26] G. DeBacker, M. Vantorre, R. Banasiak, and J. Beels, C.and DeRouck. Numerical modelling of wave energy absorption by a floating point absorber system. In *Proceedings of the Sixteenth (2007) International Offshore and Polar Engineering Conference Lisbon, Portugal, July 1–6, 2007*. ISOPE, 2007.
- [27] J. Falnes and K. Budal. Wave-power conversion by point absorbers. *Norwegian Maritime Research*, 6(4):2–11, 1978.
- [28] K.J. Gunn, C.J. Taylor, and C.J. Lingwood. *An Independent Validation of the Optimality of Latching and De-clutching Control by Evolutionary Methods*. 2011.
- [29] S. H. Salter, J. R. M. Taylor, and N. J. Caldwell. Power conversion mechanisms for wave energy. *Proceedings of the Institution of Mechanical Engineers – Part M – Journal of Engineering for the Maritime Environment*, 216(1):1–27, September 2002.
- [30] C. Hiles. On the use of computational models for wave climate assessment in support of the wave energy industry. M.a.sc., University of Victoria, December 2010.
- [31] L.H. Holthuijsen. *Waves in Oceanic and Coastal Waters*. Cambridge University Press, 2007.

- [32] W. Thomson and M. Dahleh. *Theory of Vibration with Applications*. Prentice Hall, 5 edition, August 1997.
- [33] G.W. Stewart and Ji guang Sun. *Matrix perturbation theory*. Computer science and scientific computing. Academic Press, 1990.
- [34] S. Rao. *Mechanical Vibrations*. Prentice Hall, 4 edition, April 2003.